School of Chemistry

Fabrication and evaluation of P-i-N junction Diamond Betavoltaic Diodes

Ben Harding

This thesis is submitted in partial fulfilment of the requirements for the Honours Degree of MSci Chemical Physics with Industrial Experience at the University of Bristol

Supervisor: Professor Neil Fox

Second Assessor: Professor Paul May

Physical and Theoretical Chemistry

Abstract

Diamond is an ultrawide bandgap (UWBG) semiconductor with exceptional physical and electrical properties, such attributes make it an attractive candidate for betavoltaic devices. These nuclear batteries generate electrical current from beta particles emitted by radioactive sources and produce a stable power output over a long working lifetime, making them suitable for inaccessible environments.

This report explores the fabrication of functional p-type / intrinsic / n-type (P-i-N) junction diamond diodes and investigate their application as potential betavoltaic cells. All layers were prepared and grown in the Bristol Diamond Laboratory via Microwave plasma enhanced chemical vapour deposition (MWCVD). The growth of these devices began on a polycrystalline diamond substrate. A boron doped (p-type) layer was first deposited, followed by an intrinsic diamond layer and finally a nitrogen doped (n-type) layer. Ohmic contacts of platinum/palladium were applied to both the exposed p-type and n-type layers, forming a pseudo-vertical P-i-N diode structure.

The fabrication process yielded reproducible P-i-N junction diodes that possessed rectifying properties. The best diode, produced a rectification ratio of 311, observed at 12 V. Upon remeasurement following reapplication of the metal contacts, a maximum forward current of 6×10^{-4} A was recorded at 20 V. The threshold voltage of the device was estimated to be 5.5 V.

An experimental investigation of co-doping with boron and nitrogen clusters to achieve a more efficient n-type diamond layer in the P-i-N structure was also carried out, a critical advancement for the next generation of betavoltaics. However, early results were inconclusive.

Acknowledgements

Firstly, I would like to say a thank you to Professor Neil Fox for his supervision and for making this project possible. Secondly, a thank you to Professor Paul May, my tutor and industrial supervisor, for his guidance and insightful advice throughout the project.

I'd like to acknowledge the BUDGie group for all their support and for making my master's project such an enjoyable and collaborative experience. With a big thank you to Dr. Ramiz Zulkharnay for putting up with me in the lab, providing advice, helping me understand the work, and always taking the time to answer my many questions.

Finally, a special thank you to Axel Persson, James Swarbrigg and Jacob Fox – the Diamond boys. Live Mas!

Table of Contents

1 Introduction *1*

1.1 Betavoltaic Devices 1

1.2 Band Gap Theory and Band Structure 9

1.3 Traditional Diodes 11
1.3.1 Diodes 11
1.3.2 Carrier Transport Theory in Diodes 13

1.4 Diamond and it's Synthesis 18
1.4.1 High Pressure High Temperature synthesis (HPHT) 19
1.4.2 Chemical Vapour Deposition of Diamond synthesis (CVD) 19

1.5 Diamond Doping 22
1.5.1 P-type diamond 23
1.5.2 N-type diamond 23

1.6 Diamond as a Semiconductor and viability for Betavoltaic applications 25
1.6.1 Diamond as a Semiconductor 25
1.6.2 Diamond Betavoltaics 26

1.7 Aside on Radionuclides 29

1.8 Aim of the thesis 30

2 Experimental *31*

2.0 Device summary: 31

2.0.1 Diode Structure I 32

2.0.2 Diode Structure II 33

2.0.3 Process Overview 34

2.1 Substrate and P-layer Growth 35

2.2 Intrinsic-layer Growth 37

2.3 Lasers micromachining apparatus 38

2.3 N-layer Growth 39

2.4 Hydrogen Surface Termination 41

2.5 Preparation for Metallisation 42

2.6 Metallisation and Wiring 43

2.7 Complete Device and Analysis 46

2.8 Other Experimental Sample Preparation 48

3 Characterisation techniques *49*

3.1 Scanning Electron Microscopy (SEM) 49

3.2 Energy-Dispersive X-ray Spectroscopy (EDS) 50

3.3 Laser Raman Spectroscopy 50

3.4 Olympus LEXT Confocal 52

3.5 4-point-probe (4PP) 53

3.6 Hall Voltage Measurement 54

4 Results and Discussion ... *56*

4.1 Raman Spectroscopy ... **56**

4.1.1 N-type Diamond ... 56

4.1.2 P-type Diamond ... 58

4.2 Four Point-Probe ... **59**

4.3 Scanning Electron Microscopy ... **61**

4.4 Current-Voltage (I-V) characteristics ... **65**

4.4.1 Diode 1 ... 65

4.4.2 Diode 2 ... 69

4.4.3 Diode 3 ... 71

4.4.4 Diode 4 ... 74

4.4.5 Diode 5 ... 77

4.4.6 Surface contacts and Silver Contamination ... 78

5 Conclusions and Future Work ... *80*

5.1 Conclusions ... **80**

5.2 Future work ... **81**

6 References ... *84*

List of Tables

Table 1 – Comprehensive summary of fabricated P-i-N diodes ... 31
Table 2 - The conditions used for the p-layer growth in the back reactor. ... 36
Table 3 - The conditions used for the intrinsic layer growth in the front reactor. ... 38
Table 4 - The conditions used for the n-layer growth in the front reactor. ... 39
Table 5 - The conditions used for the n-layer growth in the back reactor. ... 40
Table 6 -The stepwise process for hydrogen termination. ... 41

List of Figures

Figure 1 - Rappaport patent for the first ever betavoltaic device. ... 3
Figure 2 – Cross sections taken of the Betacel.. ... 5
Figure 3 – A Ragone plot for the comparison of batteries. ... 6
Figure 4 - City Labs' NanoTritium™ battery ... 7
Figure 5 - A diagram showing the conduction and valence bands of a metal, a semiconductor and an insulator.. ... 9
Figure 6 - A diagram demonstrating how the band gap of an extrinsic semiconductor varies with doping.. ... 10
Figure 7 – A schematic of a p-type material and an n-type material. ... 12
Figure 8 - Typical I-V curve of a diode ... 16
Figure 9 – A diagram of a basic P-i-N diode structure ... 17
Figure 10 - A schematic for the reaction process of diamond during CVD ... 21
Figure 11 - The current-voltage characteristic of the P-i-M single crystal CVD diamond membrane. ... 28

Figure 12 - [A] Schematic of the pn junction diamond diode. [B] The current-voltage characteristic of the pn junction diode.. 28
Figure 13 – Radionuclide Beta decay schemes 30
Figure 14 – A schematic of Diode Structure I 32
Figure 15 – A schematic of Diode Structure II 33
Figure 16 - A flowchart for the fabrication procedure. 34
Figure 17 - Microwave plasma-enhanced CVD reactor 35
Figure 18 - Molybdenum mask on Diode 4. 37
Figure 19 - Photograph of the exterior of the laser micromachining apparatus. 38
Figure 20 - Photograph of Diode 4 and Diode 5 masked with Kapton tape before metallisation 42
Figure 21 - A photograph of the AGAR High Resolution Sputter Coater.. 43
Figure 22 - Photograph of the copper wires being attached to the Pt/Pd contact of Diode 1. 44
Figure 23 - A series of photographs demonstrating a diodes journey ‘Beyond the reactor’ ... 45
Figure 24 – Bad metallisation examples 46
Figure 25 - A screenshot of Keithley code. 47
Figure 26 - Photograph of a typical I-V measurement setup 47
Figure 27 - Photograph of a repurposed Edwards S150A sputter-coater for oxygen plasma. 48
Figure 28 – A schematic of a scanning electron microscope 50
Figure 29 - Raman Spectrum for a Single Crystal Diamond calibration sample 51
Figure 30 - LEXT map images of Diode 1 and Diode 2 before metallisation.. 52
Figure 31 - BDD sample placed in the 4-point-probe apparatus. 53
Figure 32 - A diagram of the hall effect in a 2D conducting material 55
Figure 33 - Raman spectrum for the n-layer of Diode 1 56
Figure 34 - Raman spectrum for the p-layer of Diode 1 58
Figure 35- I-V Response of BDD under the 4-point-probe apparatus. 60
Figure 36 - SEM images of the surface of the BDD used in Diode 1 and Diode 2 62
Figure 37 - SEM image of the top-view P-i-N junction of Diode 1 63
Figure 38 - SEM image of the top-view P-i-N junction of Diode 2. 63
Figure 39 - Rectification ratio at a given potential difference for Diode 1. 66
Figure 40 - Initial Diode 1 I-V response. 66
Figure 41 - Diode 1 I-V response with reapplied ohmic contacts 68
Figure 42 - Rectification ratio at a given potential difference for Diode 1 after the ohmic contacts were reapplied 68
Figure 43 - Diode 2 I-V response with a linear best-fit line calculated. 69
Figure 44- Diode 3 I-V response with a linear line of best-fit calculated 71
Figure 45 - Raman spectrum for the topside of the Element Six BDD 73
Figure 46 - Raman spectrum for the backside of the Element Six BDD. 73
Figure 47 - Diode 4 I-V response 75
Figure 48 - Rectification ratio at a given potential difference for Diode 4. 75
Figure 49 - I-V comparison of the initial Diode 1 measurements compared to Diode 4 76
Figure 50 - I-V comparison of Diode 1 to Diode 4. 76
Figure 51 - Diode 5 I-V response 78
Figure 52 – An optical microscope image of silver DAG and silver migration 79
Figure 53 - EDS Spectrum from silver contamination investigation. 80

1 Introduction

1.1 Betavoltaic Devices

The concept of the ‘Electron Voltaic Effect’ was first introduced in 1951 by Ehrenberg et al. at Birkbeck College, University of London [1]. Ehrenberg and his team concluded that photovoltaic cells were sensitive to electron bombardment; whilst investigating the effect of current amplification in selenium cells under bombardment by electron beam.
They observed a rapid voltage increase, which appeared to be proportional to the number of ion pairs in selenium.

In 1953, American scientist Paul Rappaport, working at the Radio Corporation of America (RCA), explored the electron-voltaic effect in semiconductor materials. He published an article titled “The Electron-Voltaic Effect in P-N Junctions Induced by Beta Particle Bombardment” [2], where he described using a 50-millicurie Strontium-90/Yttrium-90 radioactive source to bombard silicon and germanium wafers with beta particles. This marked the first documented prototype of a beta-voltaic device.

The total efficiency, η, of a beta voltaic device can be separated into two distinct components;

$$\eta = \eta_{source}\,\eta_{conv} \tag{1.1}$$

Where η_{source} is the efficiency of the beta source and is radionuclide dependent. $\eta_{conv}$is the conversion efficiency of the semiconductor [3]. The cell designed by Rappaport produced 0.8 µW of power with an average efficiency of approximately 0.2%. Given the radioactive source's power output of around 200 mW, this resulted in a conversion efficiency of 0.4% for the device [2,4]. A year later, in 1954, Rappaport and a colleague filed a patent for this technology on behalf of RCA [3], a schematic of the design is shown in Figure 1. The invention was described as a means for converting the energy of radioactive material into useful electrical energy. The design consisted of a radioactive material contained within a semiconducting body, surrounded by a magnet at either end of the device. The semiconducting body contained both a P and N type region. The purpose of the device, as stated, was to create an atomic battery that utilises a semiconducting material and is distinguished by its extended lifespan.

Rappaport et al. concluded that the limiting factors of reducing the conversion efficiency were the recombination, backscattering, junction leakage and energy absorption processes other than charge carrier production. It was also noted that the effects of radiation damage were yet to be explored [2] . Decades later, Olsen et al. calculated that due to radiation damage, the maximum power output of this silicon-strontium-90 system was found to decay to one-tenth of its initial value within one week of device lifetime [7].

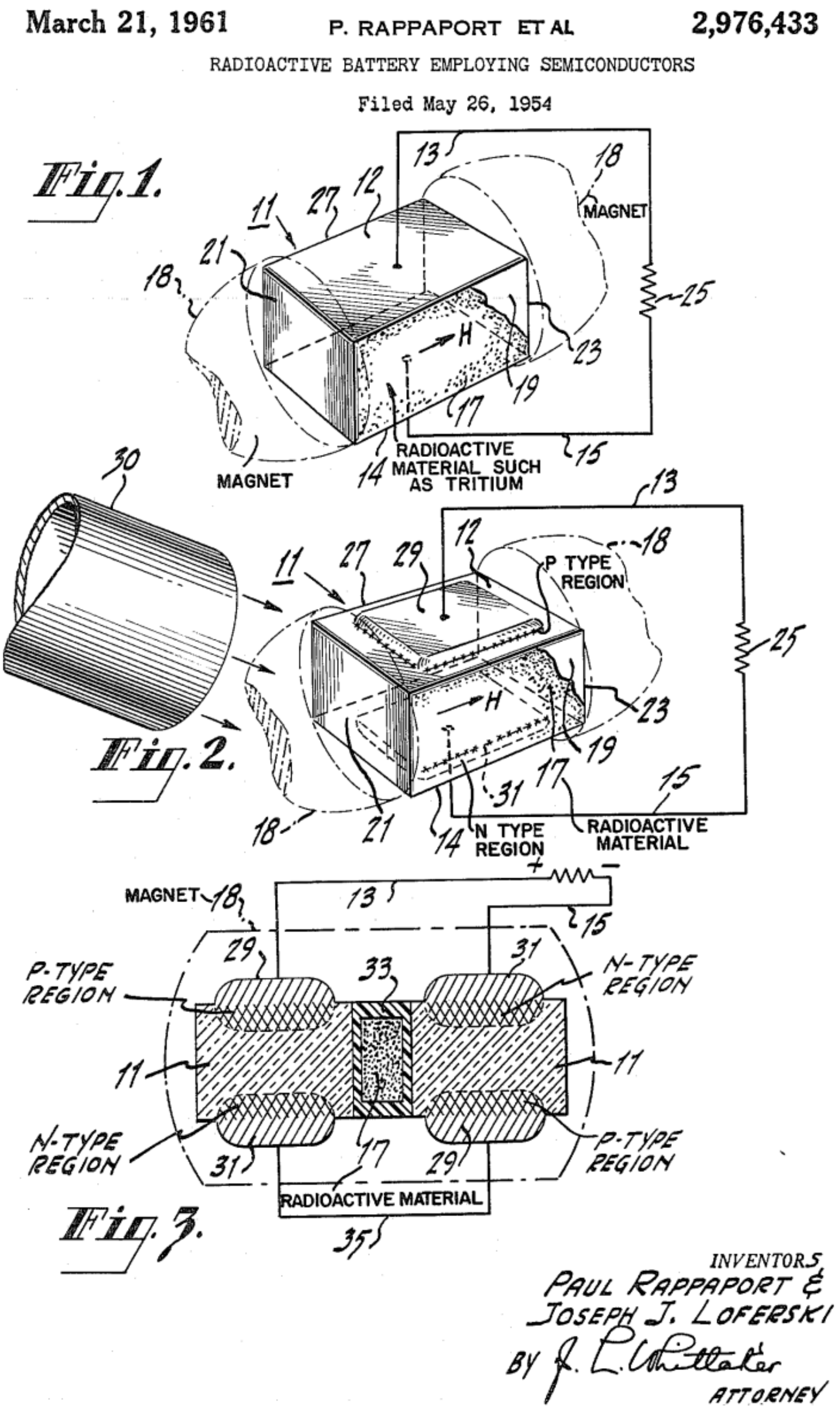

Figure 1 - Rappaport patent for a radioactive battery employing semiconductors, filed on March 21st, 1961 sourced from [5]. The first ever betavoltaic device.

In the 1970s worked continued on betavoltaic devices. Olsen et al. [8] explored the generation of power by coupling a beta source to a semiconductor device junction. This led to the production of the Betacel, the first Betavoltaic power source by a group at Donald W. Douglas Laboratories [9]. Shown in Figure 2, the design comprised of stacked planar layers of silicon as the semiconductor material and ^{147}Pm in the form of Pm_2O_3 as the beta source, it was licenced for use in cardiac pacemakers and implanted into over 100 patients. The Betacel battery achieved an efficiency of 4% based on incident flux and lifetime over 10 years with up to 400 μW of power at the beginning of its 10-year useful life [10,11].

However, Pm_2O_3 contains varying isotopes of promethium. Promethium-147 is a pure beta emitter however, Promethium-146, a contaminant, has gamma emission lines greater than 300 keV at 453keV, 735keV, 747keV [12]. High energy radiation may cause damage to batteries as well as their environment. Silicon, the semiconducting material in the Betacel, has a radiation damage threshold of approximately 200 keV [13]. The radiation damage threshold is the minimum amount of radiation energy per unit volume required to cause permanent structural damage to a material. When a material is exposed to radiation, atoms can be displaced from their lattice sites, creating defects like vacancies, interstitials, or dislocations. If the radiation energy exceeds this threshold, these displacements become irreversible, resulting in permanent damage to the material's structure and therefore decreasing the electrical conductivity of the device.

In an ideal scenario, the radioactive source of the betavoltaic battery should be a pure beta-decay method without γ-rays and X-rays to reduce radiation damage, with beta emission energies of below 300 keV [14]. Moreover, the daughter nuclei formed after the decay of the radioactive source also has no γ-ray or X-ray emission.

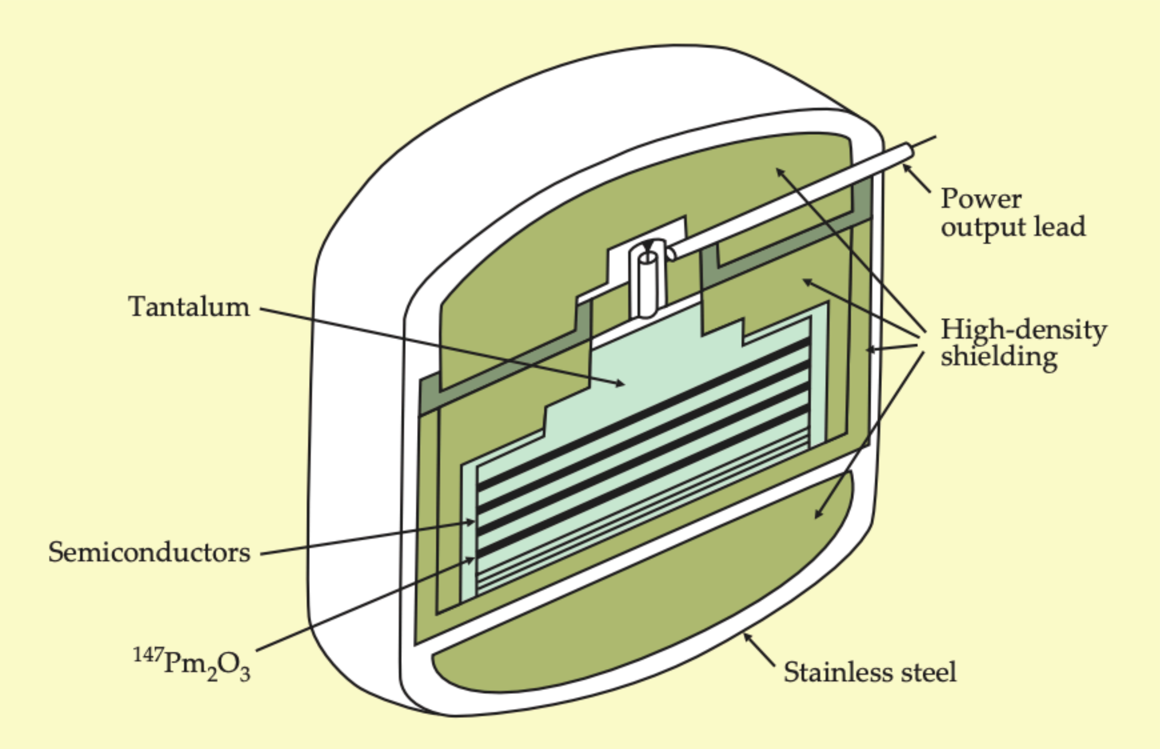

Figure 2 – Cross sections taken of the Betacel. The Betacel 400 was an early betavoltaic battery powered by promethium-147, the device was produced for cardiac pacemakers [*8*]. Although the battery remained small [13], much of its volume of the device was shielding for the gamma radiation emitted by the 146Pm source. Schematic by Larry Olsen [14].

From 1975 to 2006, studies of betavoltaics proceeded sporadically [14]. The pacemaker market was occupied by new lithium battery powered devices which were smaller; cheaper and without the negative stigma surrounding radioactivity such as the environmental concerns and the public uneasiness about nuclear safety attached to it. The nuclear pacemaker market was rendered obsolete [15]. Betavoltaic devices of today represent a category of nuclear battery which generate electrical current from beta particles emitted from a radioactive source, typically Tritium (H-3) or Nickel-63. These are pure beta emitters, meaning the radionuclide only emits beta radiation during the decay process [16]. This process is characterised as a non-thermal conversion method. The devices directly convert the radioactive decay energy of these beta-emitting isotopes into electrical energy employing a semiconductor method of charge collection. When beta particles enter the energy converting structure, many electron-hole pairs are generated. If the electron-hole pairs are generated within the depletion layer, the electrons and holes can be separated by the built-in potential to generate an electrical current. Conversely, if the electron hole pairs are formed outside of this region, they are likely to recombine, dissipating energy as heat [18].

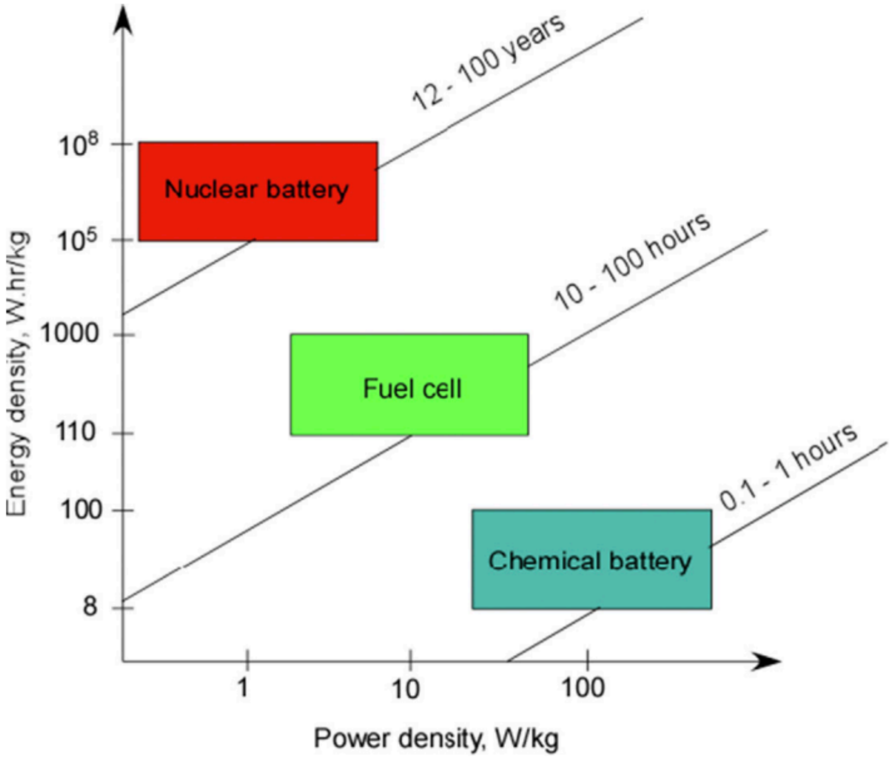

Figure 3 – A Ragone plot for the comparison of nuclear batteries, fuel cells and a chemical batteries sourced from [6].

Betavoltaic devices typically have a low power output due to this being proportional to the radioactive power of the radionuclide and limited by the efficiency of the device [19]. However, the devices produce a stable power output over a long working lifetime and have a high energy density. The betavoltaic battery provides a reliable, long-life power supply in harsh or inaccessible environments. As mentioned earlier, between the mid-1970s and early 2000s, studies and production of betavoltaic devices remained intermittent. Until in 2010, when City Labs' NanoTritium battery was awarded the betavoltaic industry's first general license for 'manufacturing and distribution', meaning it can be purchased by any user [4].

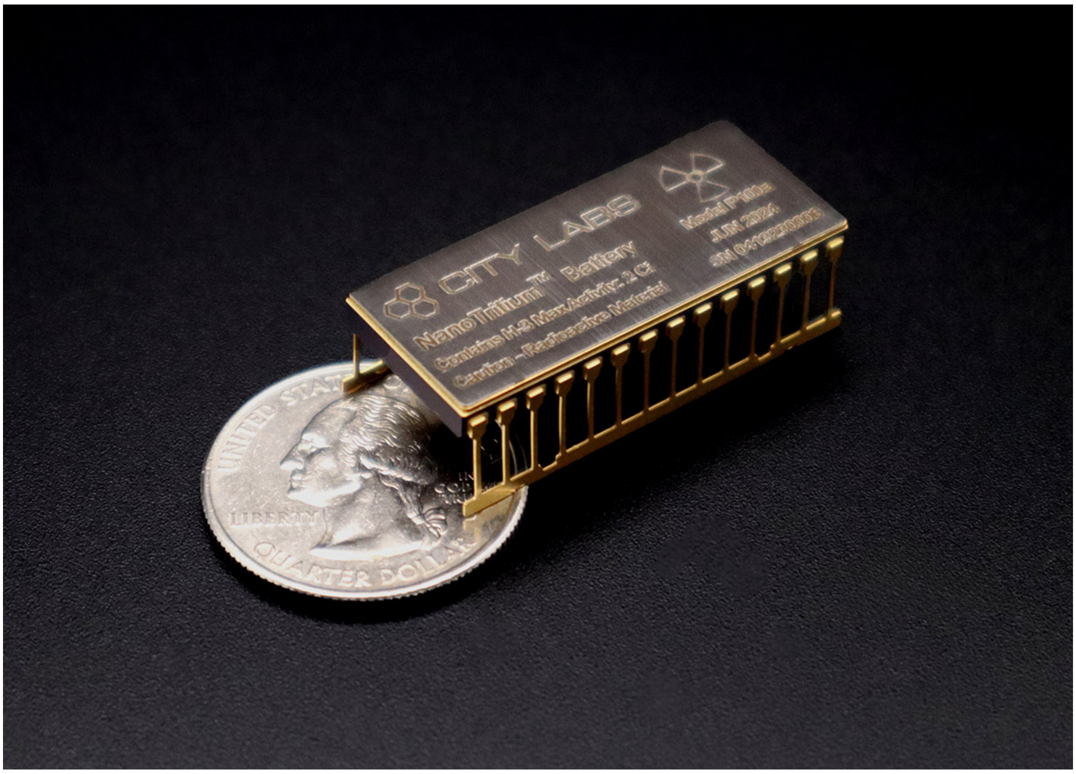

Figure 4 - City Labs' NanoTritium™ battery size comparison with a US quarter; a small-scale nuclear battery able to provide low-energy devices in extreme environments with power for over 20 years [17].

High prices, starting at several thousand dollars per unit, and limited production capacity have kept City Labs' NanoTritium batteries primarily confined to research. These betavoltaic devices are designed for environments where long-term, maintenance-free power is critical, such as space exploration, military applications, and medical implants like the Betacel.

Since the inception of the space program in the 1950s, the National Aeronautics and Space Administration (NASA) has relied on Radioisotope Thermoelectric Generators (RTGs) to power vehicles exploring outer space [20]. These generators, deployed in missions such as Apollo, Viking, and Voyager, have proved their ruggedness, reliability, and long lifetimes, making them crucial for deep-space exploration [21]. Although different to betavoltaics, with RTGs utilising the heat generated from radioactive decay, both methods harness energy from radioactive decay demonstrating their applicability to space exploration.

Beyond medical implants and space exploration, betavoltaic devices have found use in novel applications where conventional batteries would fail. Examples include sensors designed to operate in extreme environments such as high-radiation zones, deep underwater, or areas with extreme temperatures [4]. These environments render standard chemical batteries impractical due to their limited lifespan and sensitivity to environmental conditions. However, the use of betavoltaic devices in consumer products remains virtually non-existent due to the cost and regulatory complexities associated with handling radioactive materials like tritium. Despite their advantages, such as the ability to generate power continuously for decades without recharging, betavoltaics like NanoTritium are far from becoming a mainstream energy solution for the general public.

Today, researchers at Bristol University have successfully fabricated the world's first carbon-14 diamond battery, with the potential to power devices for thousands of years [24]. Carbon-14 can be used in the growth process, removing the need for an external beta source, with the battery providing its own internal power source. This carbon isotope is a beta emitter with half-life 5730 ± 40 years and 156 keV decay energy [22], it is formed naturally in the upper atmosphere by the irradiation of N-14 by cosmic ray neutrons. Carbon-14 can also be obtained from the reprocessing of man-made spent nuclear fuel in the form of $BaCO_3$ powder and radioactive graphite. Repurposing waste carbon would contribute to a decrease in the overall amount of nuclear waste generated [23]. On beta emission the isotope decays into nitrogen, although this degrades the quality of the battery overtime, nitrogen is a clean gas and the most abundant in Earth's atmosphere. The carbon-14 diamond battery represents a novel approach to energy storage, though its development is still at an early stage, with significant research and refinement required to achieve practical applications [24].

1.2 Band Gap Theory and Band Structure

The band gap is the energy between the valence band and the conduction band.
In metals these bands overlap, allowing for the free movement of electrons through the material. Electrons can transition from the valence band to the conduction band when subjected to an external electric field, resulting in the creation of holes, which are defined as the absence of electrons. This process facilitates the generation of electrical conductivity.

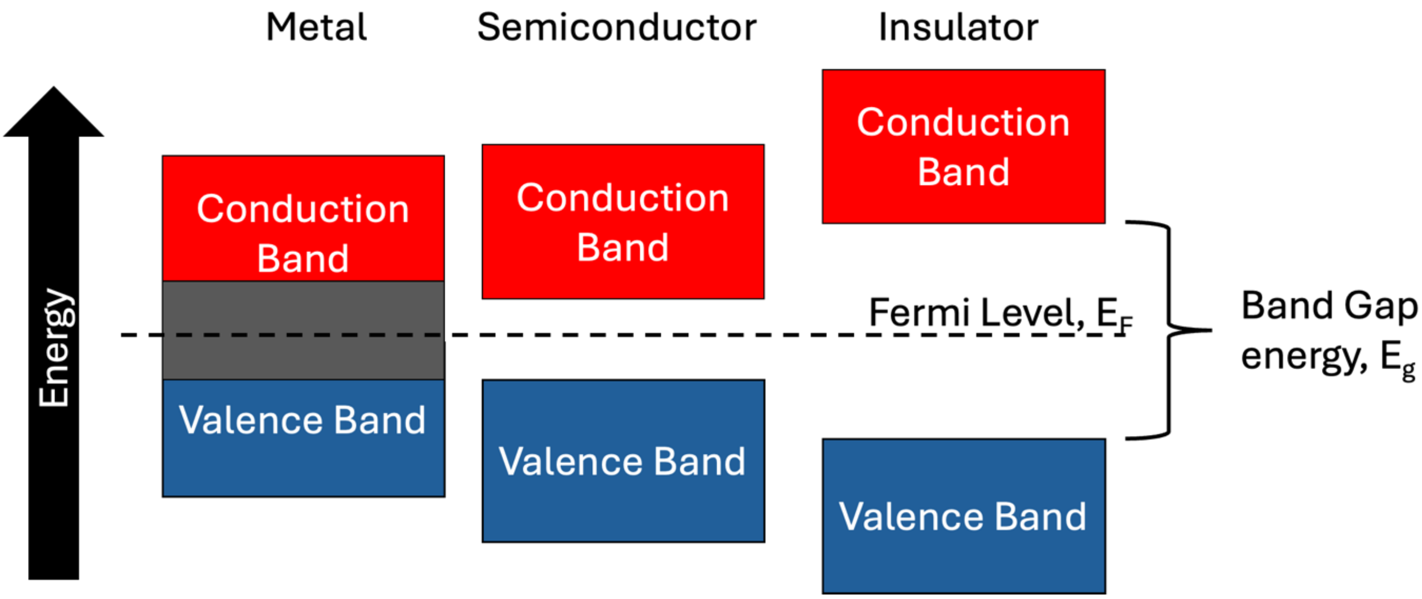

Figure 5 - A diagram showing the conduction and valence bands of a metal, a semiconductor and an insulator. The diagram highlights the size gaps between the bands and the overlap of the bands in a metal.

In insulators the band gap is large, electrons cannot easily move from the valence band to the conduction band. In a conductor there is no band gap, the valence band and conduction band overlap, electrons move freely between the two bands. A semiconductor has an intermediate band gap and can be described as a material that is between an insulator and a conductor, sharing properties with both. This 'intermediate' band gap can be overcome by thermal energy, light or applied voltage allowing semiconductors to exhibit controllable electrical conductivity.

The electrical conductivity of semiconductors can be modified through a process called doping, which involves substituting atoms in the crystal lattice with elements that have either more or fewer valence electrons. These dopant elements introduce free electrons or holes into the material, significantly altering its electrical properties while minimally impacting other bulk properties. Depending on the type of dopant, this process creates n-type (negative) or p-type (positive) semiconductors, facilitating tailored electronic functionality for a range of applications.

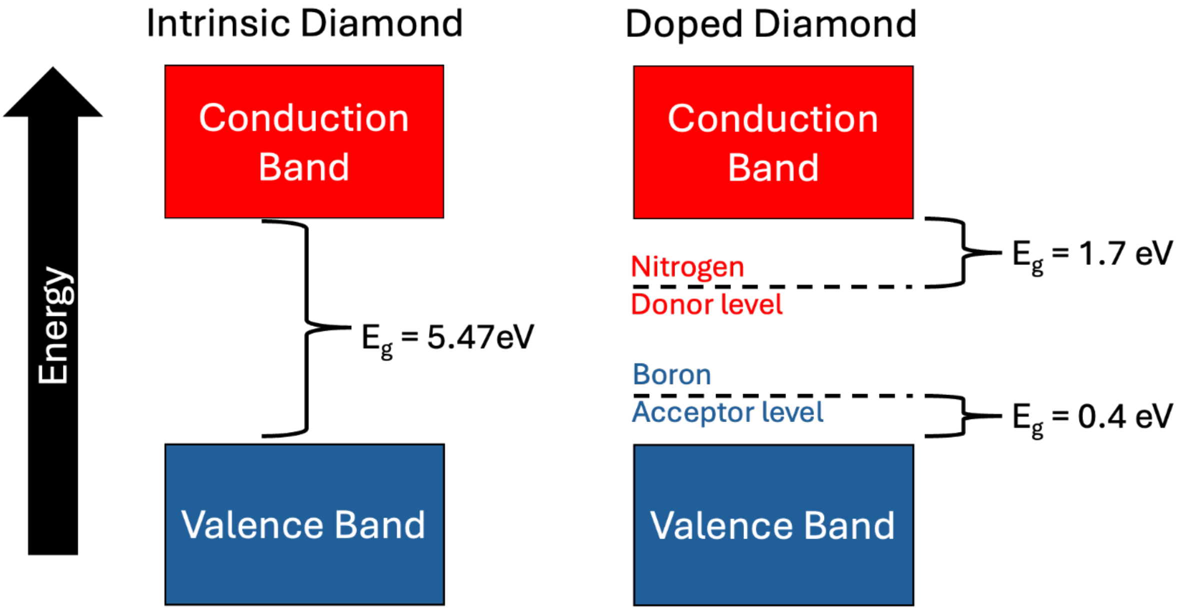

Figure 6 - A diagram demonstrating how the band gap of an extrinsic semiconductor varies with doping. It also highlights where n-type and p-type dopants sits within a semiconductor structure.

Acceptors are impurities which have less valence electrons than the host, they contribute energy levels above the valence band edge. They accept electrons from the valence band, leaving holes in the valence band which can contribute to electrical conduction. Similarly, donor levels are formed by donors with more valence electrons and contribute to energy levels just below the conduction band.

1.3 Traditional Diodes

1.3.1 Diodes

A diode is a two-terminal semiconductor device that only allows current to flow in one direction. The simplest form of a diode is the p-n junction, formed by joining p-type and n-type semiconductor materials. This junction creates an electrical asymmetry; when a forward voltage is applied, the diode conducts electricity. However, when a reverse voltage is applied, the diode blocks most of the current, acting as an electrical check valve. In the forward direction, the device must overcome a built-in potential which is related to the work function of the semiconducting material.

When the junction is formed between the P and N type materials, the Fermi levels (chemical potentials) align on either side of the interface. To account for this band bending occurs due to a charge transfer at the interface until an equilibrium is reached between the chemical potentials. The redistribution of charge creates an internal electric field; electrons diffuse from the n-type region to the p-type region, leaving behind holes and a depletion region is created. Thus, the built-in electric field leads to a built-in potential barrier, V_{bi}, forming across the junction.

$$V_{bi} = \frac{k_B T}{e} \, ln\left(\frac{N_A N_D}{{n_i}^2}\right) \tag{1.2}$$

where N_a is the acceptor atoms concentration in cm^{-3}; N_D is the donor atom concentration in cm^{-3}, and n_i is the concentration of carrier electrons within the intrinsic material in cm^{-3}. e is the elementary charge of an electron. k_BT/e is known as the thermal voltage, V_T and is equivalent to approximately 25 mV at room temperature.

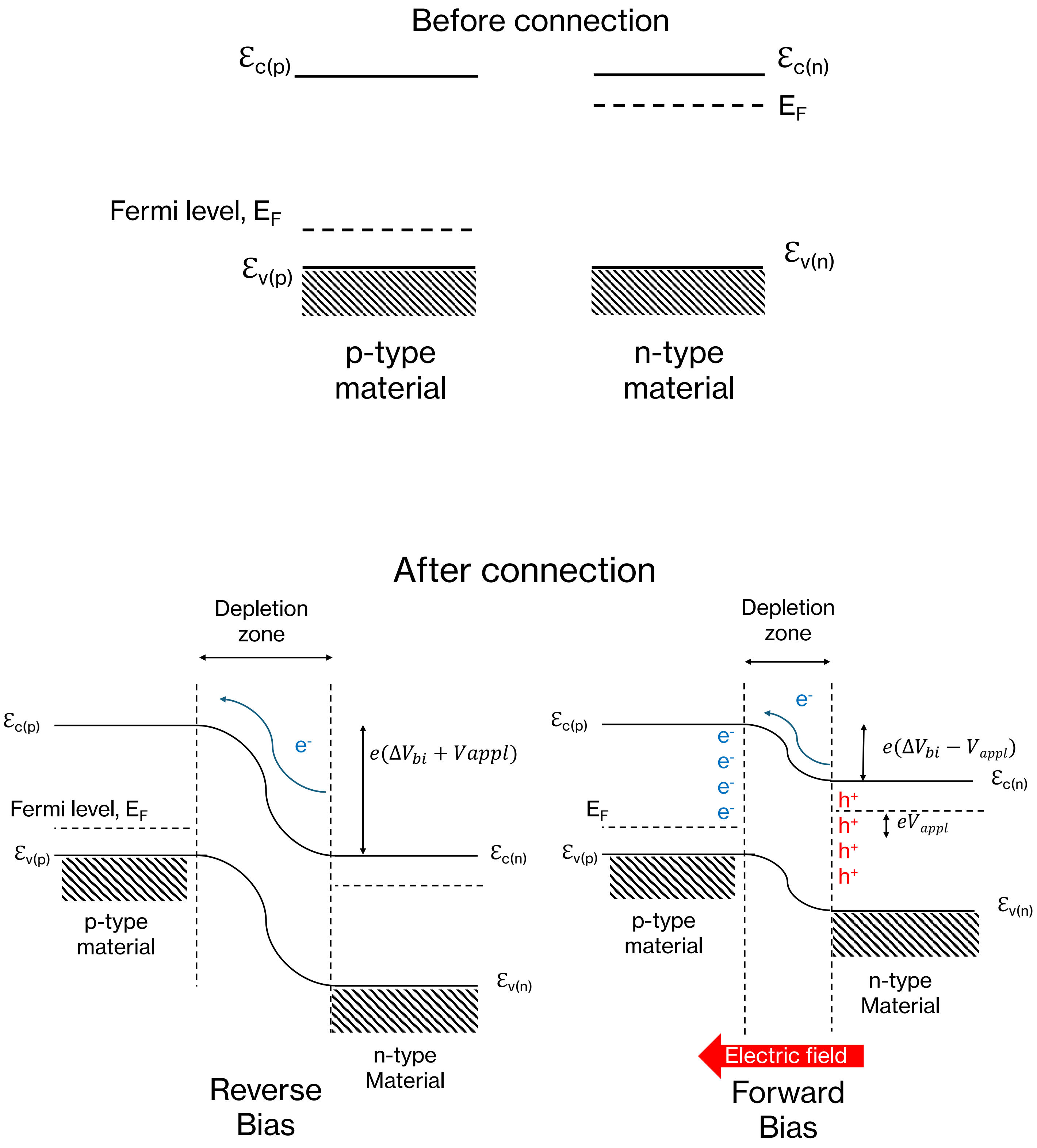

Figure 7 – A schematic of a p-type material and an n-type material. Before connection: The fermi levels are at different energies. After connection: the Fermi levels align and band bending occurs, and a built-in potential is formed. The built-in potential varies with applied voltage across the junction.

1.3.2 Carrier Transport Theory in Diodes

Carrier transport in a pn junction diode is governed by diffusion and drift. These processes arise due to carrier concentration gradients and built-in electric fields, respectively. Electrons diffuse from the n-region to the p-region, J_e^{diff}, whilst drifting from the p-region to the n-region, J_e^{drift}. Hole carrier transport occurs in the opposite direction, J_e^{drift} and J_h^{drift}, respectively. At equilibrium, with no external applied bias, the net current in the semiconductor is zero. The diffusion and drift currents balance each other.

$$J_e^{drift} = -J_e^{diff} \tag{1.3}$$

$$J_h^{drift} = -J_h^{diff} \tag{1.4}$$

When an external voltage V_{appl} is applied, the built-in potential barrier ΔV_{bi} is modified.

$$\Delta V'_{bi} = \Delta V_{bi} - V_{appl} \tag{1.5}$$

where $\Delta V'_{bi}$ represents the change in potential barrier due to the applied voltage, V_{appl}. The generation current density, J_e^{gen}, follows an exponential dependence on the potential barrier.

$$J_e^{gen} = J_0 e^{-\frac{e\Delta V_{bi}}{k_B T}} \tag{1.6}$$

Where J_0 is the saturation current density, k_B is Boltzmann's constant, and T is the absolute temperature in Kelvin. Under an applied voltage, the diffusion current can be written in terms of the modified potential barrier.

$$J_e^{diff} = J_0 e^{-\frac{e\Delta V_{bi}'}{k_B T}} \tag{1.7}$$

Substituting (1.5) into (1.7) gives:

$$J_e^{diff} = J_e^{gen} e^{-\frac{eV_{appl}}{k_B T}} \tag{1.8}$$

The rate of recombination is assumed to be small, and the generation rate of minority carriers does not depend on V_{appl}. Therefore;

$$J_e^{drift} = -J_e^{gen} \tag{1.9}$$

The net current density, combining the forward diffusion current, J_e^{diff}, and the reverse saturation current, J_e^{drift}, follows an exponential dependence on the applied voltage:

$$J_{total} \propto \left[e^{\frac{eV_{appl}}{k_B T}} - 1\right] \tag{1.10}$$

Which can be rewritten in terms of the thermal voltage $V_T = \frac{k_B T}{e}$:

$$J_{total} \propto \left[e^{\frac{V_{appl}}{V_T}} - 1\right] \tag{1.11}$$

This leads to the Shockley diode equation, which describes the total current through a pn junction:

$$I_{total} = I_0 \left[e^{\frac{V_{appl}}{\eta V_T}} - 1 \right] \tag{1.12}$$

Where I_0 is the reverse saturation current, and η is the ideality factor, a measure of how closely a diode follows the diode equation. Equation 1.10 is valid under both the forward and reverse bias regions but does not apply in the breakdown region, the exponential response is shown in Figure 8. Real diodes generally exhibit small deviations from this model [25, 26, 27].

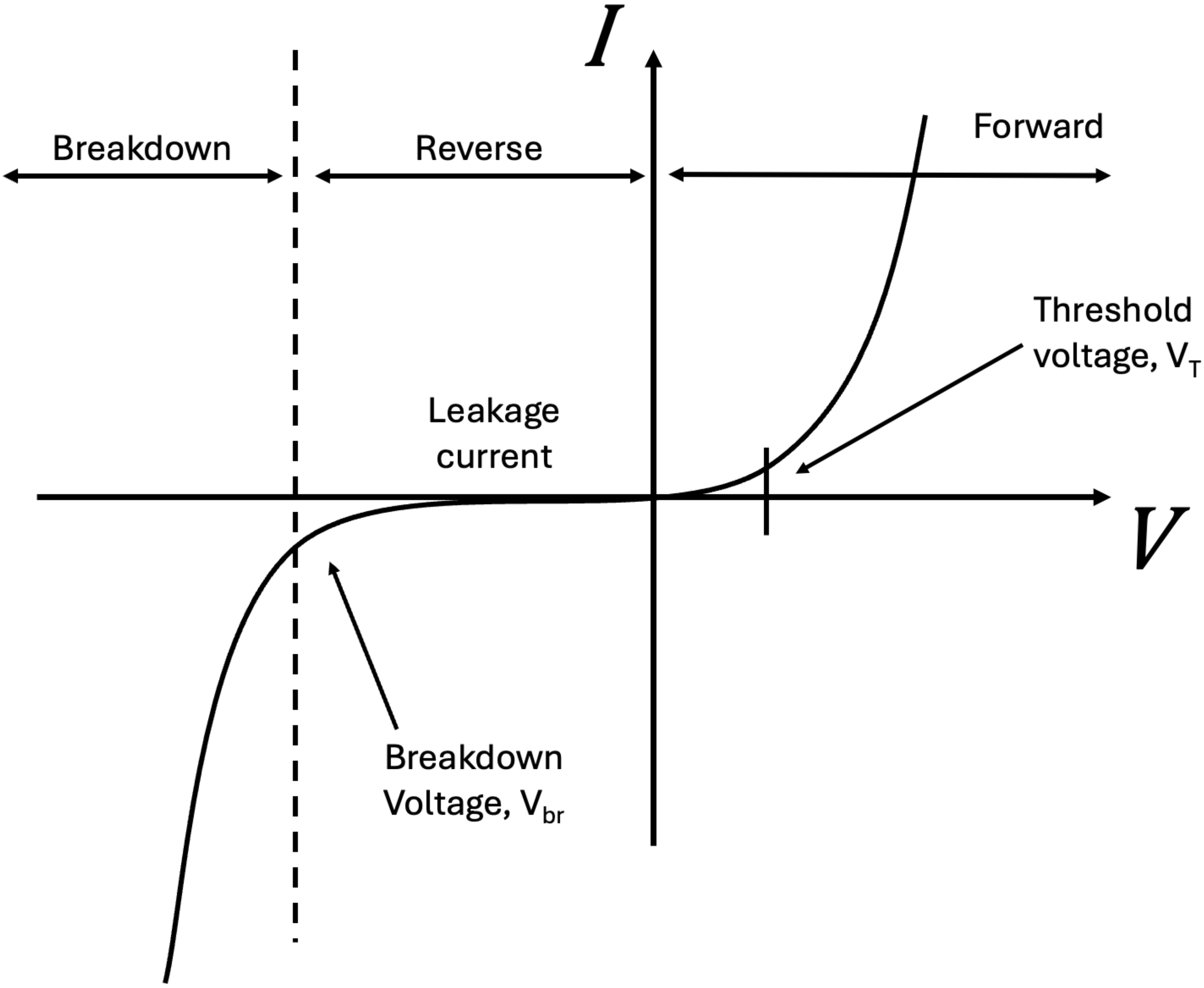

Figure 8 - Typical I-V curve of a diode. The diagram highlights key characteristics such as the threshold voltage, V_T , and the breakdown voltage, V_{br} . The graph shows an exponential increase in the current under forward bias and minimal leakage current under reverse bias, until the breakdown voltage V_{br}.

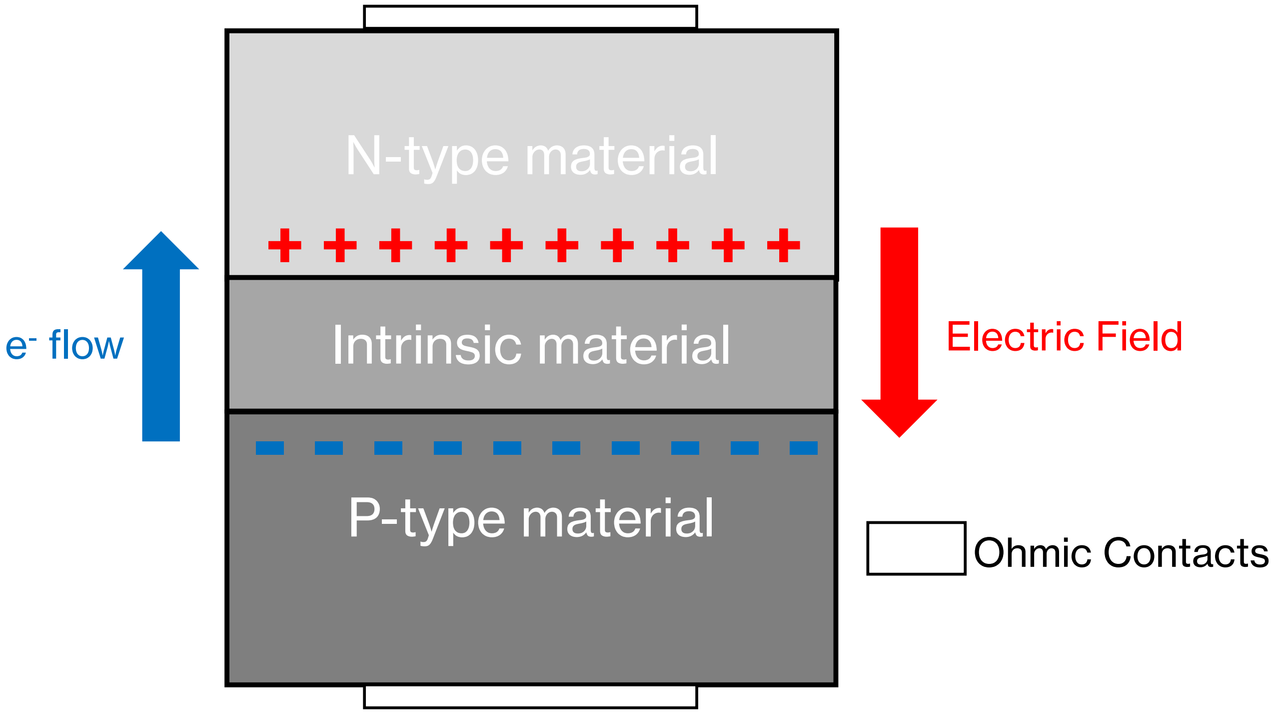

Figure 9 – A diagram of a basic P-i-N diode structure, the negative charges represent electrons, and the positive charges represent holes.

A variation of a standard pn junction diode is the p-i-n junction diode. The i represents an intrinsic semiconductor layer between the p-type and n-type regions as shown in Figure *9*. This intrinsic layer increases the width of the depletion region, improving the diode's ability to handle high voltages and making it particularly useful in applications requiring efficient charge collection, such as radiation detection and energy conversion in betavoltaics. An electric field is formed across the intrinsic material due to the collection of electrons and holes at either side of the junction, yet the intrinsic layer itself has no net charge across it.

In a typical vertical diode structure, current flows vertically through all layers allowing for a compact design. A pseudo vertical structure mimics the vertical current flow adapting to the limitation of the bottom contact being obstructed by the insulating substrate layer. In this report, the devices constructed had a pseudo vertical structure.

Rectification ratio is a measure of good diode behaviour. It is a figure of merit that measures the effectiveness of current rectification. The ratio of current under forward bias to the current under reverse bias and can be used to define the efficiency of a device. Throughout this study, this ratio is explored to characterise fabricated devices. Another key parameter in diode function is the threshold voltage. The threshold voltage which is not to be confused with the built-in voltage, is the voltage at which significant current begins to flow. This is another key characteristic in device performance which is explored in this work.

1.4 Diamond and it’s Synthesis

Diamond, in its simplest form, is an sp^3 hybridised allotrope of carbon. Yet, at its most celebrated, it stands as a gemstone of remarkable brilliance and unparalleled lustre, captivating admiration worldwide [28]. This dual nature of diamond—as both a scientific marvel and a symbol of luxury—has driven the global diamond industry to a valuation of $96.4 billion USD as of 2022 [29].

The De Beers Group, a leader in the diamond industry, has recently experienced a 22% year-on-year drop in rough diamond sales [30]. Economic challenges in major markets like China and the United States have dampened consumer confidence, contributing to a decline in traditional diamond sales. However, these challenges may not fully explain the market contraction. The rise of synthetic diamonds, which are both physically and chemically identical to natural diamond, has disrupted De Beers’ longstanding dominance, reshaping consumer preferences and expectations. In response, De Beers has shifted its strategic focus from the sale of rough diamonds to building a luxury brand image, emphasising the allure and exclusivity of natural diamonds. This pivot reflects the industry's evolving landscape, where innovation in diamond synthesis and shifting consumer attitudes are redefining the value of these precious stones.

There are two primary methods for this synthetic diamond growth, High Pressure High Temperature (HPHT) and Chemical Vapour Deposition (CVD).

1.4.1 High Pressure High Temperature synthesis (HPHT)

HPHT was the first method to effectively synthesise diamond, it attempted to model the conditions of diamonds formation within the Earth's mantle. Over 70 years ago, in 1953, scientists in Sweden synthesised diamond from a mixture of iron carbide (Fe_3C) and graphite using high pressures of 7.5 GPa and high temperatures of 1500°C [31]. Today, the standard conditions for High-Pressure High-Temperature (HPHT) diamond growth are approximately 1300-1600°C and 5-6 GPa [32]. Catalysts are often used to reduce the required temperature, but the growth method remains highly energy-intensive and costly due to the need to maintain such extreme conditions. Additionally, the equipment used is expensive, and the process can produce a range of crystal sizes, including larger crystals up to 8-10mm [23]. With the potential for contamination from atmospheric nitrogen, the control of impurities is critical when optimising the electrical properties of diamond.

Although HPHT is a common technique with applications in both industry and research, it will not be explored any further in this report.

1.4.2 Chemical Vapour Deposition of Diamond synthesis (CVD)

Until the 1980s, High-Pressure High-Temperature (HPHT) was the only method commercially available for diamond growth. However, the development of Chemical Vapor Deposition (CVD) techniques, including Hot Filament CVD and Microwave CVD, introduced new approaches. Hot Filament CVD involves heating a filament, typically tungsten, to temperatures exceeding 2000°C to activate gaseous reactants, creating a chemical reaction that deposits carbon atoms onto a substrate. In contrast, Microwave CVD uses microwave radiation to generate a plasma, which activates the reactants and facilitates diamond growth. Unlike HPHT, which replicates the extreme conditions of diamond formation in nature, CVD grows diamond by depositing carbon atoms one-at-a-time onto a substrate or template, forming a thin solid film [33]. This process occurs at lower temperatures at around 1000°C and pressures, at approximately 100 Torr which is equivalent to 1/7 atmospheric pressure. This offers the advantages of simpler equipment and reduced energy consumption.

During the CVD process, methane and hydrogen are mixed in a chamber and pass through an activation region, forming a plasma of activation products such as free radicals and ions, which then deposit onto the substrate to form diamond. The diamonds are built piece-by-piece at the surface of the substrate [33]. The predominantly hydrogen-based plasma is formed directly above the substrate plane. The atomic hydrogen generated in the plasma is crucial for the growth of diamond, it terminates the growth of the film surface, maintaining the sp ^{3}-bonded structure of carbon in the diamond lattice as shown in Figure 10 [34]. The growth of CVD diamond is metastable [35], the conditions for growth via CVD favour graphite. The excess of hydrogen supresses the deposition of graphite and promotes the growth of diamond. The substrate used for diamond growth varies depending on the specific experiment. For heteroepitaxial growth, substrates such as silicon require the seeding of nanodiamond particles onto their surface to promote diamond formation. In contrast, homoepitaxial growth involves the deposition of diamond directly onto a diamond substrate. Either a single crystalline diamond (SCD) substrate, which is ideal for high performance applications, or polycrystalline diamond (PCD) substrate, which is suitable for a wide range of industrial uses, is used.

In this report, only PCD are used as growth substrates.

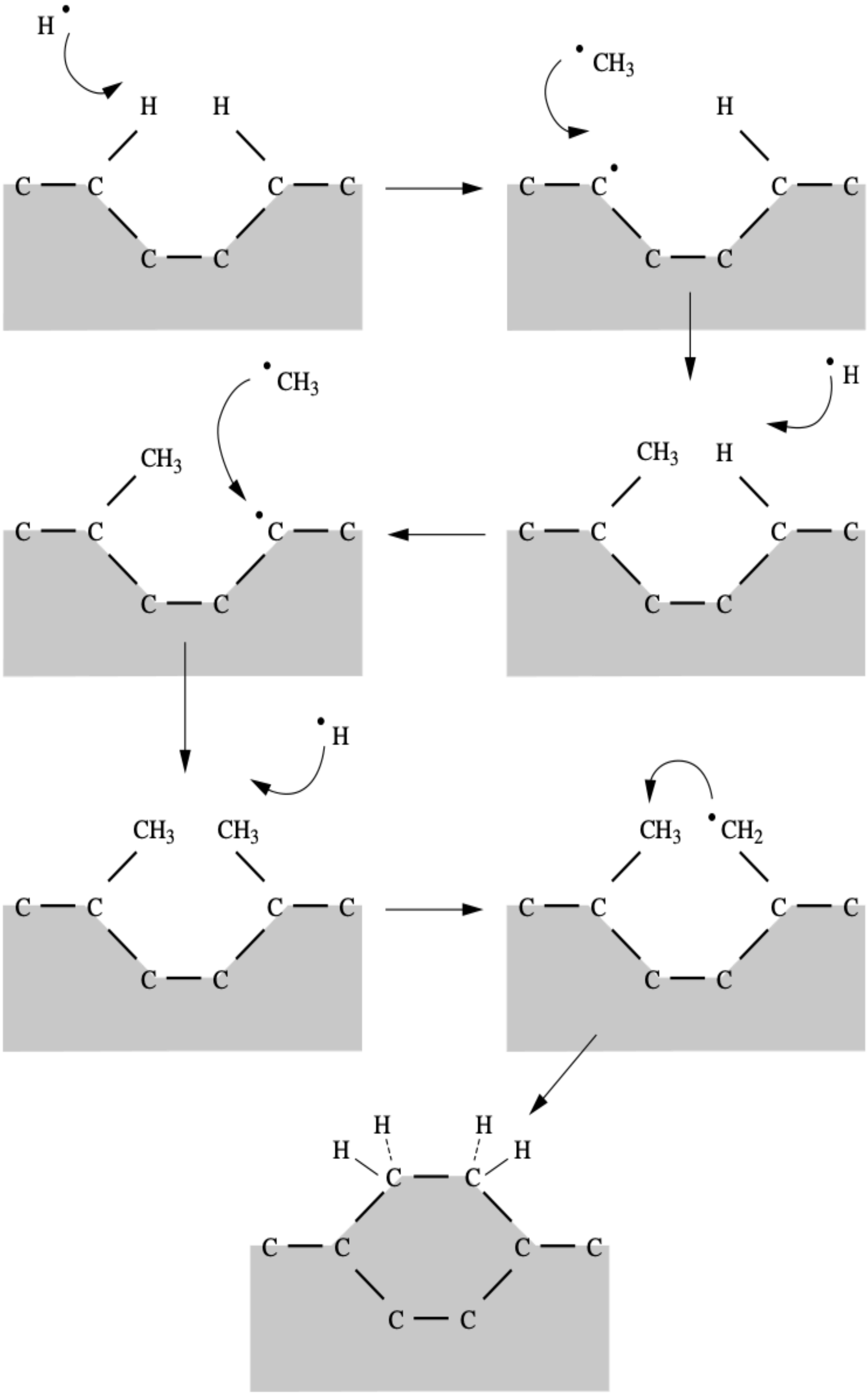

Figure 10 - A schematic for the reaction process occurring at the surface of the diamond. The formation process of diamond during CVD. Schematic by Paul May [33].

1.5 Diamond Doping

Wide band gap materials are highly attractive for power devices due to low conduction and switching loses, high temperature capability and high thermal conductivity [36]. Diamond has an ultra-wide direct band gap of 7.5 eV and an indirect band gap of 5.5 eV [37]. J.Isberg et al., exhibited charge-carrier mobilities exceeding 3000 $cm^2V^{-1}s^{-1}$ in diamond while C.J. Wort, et al., demonstrated thermal conductivities greater than 2000 $Wm^{-1}K^{-1}$ [37,38]. This data indicates that diamond has the potential to serve as an effective semiconducting material in applications necessitating high frequencies, elevated power levels, extreme temperatures, or high voltage conditions. It is an ideal candidate for the development of active components such as high-frequency field-effect transistors (FETs), and high-power switches like diodes [38]. The latter of which is explored in detail within this report.

This wide bandgap at room temperature makes diamond inherently insulating, requiring specific dopants to induce charge carriers and reduce the size of the band gap. For instance, boron atoms, which have one fewer electron than carbon, create acceptor levels within the bandgap, enabling the formation of p-type diamond. Boron doped diamond (BDD), is a basic building block for the fabrication of ohmic contacts in diamond electronic devices [39]. It is also recognised as one of the best materials for the working electrochemical electrodes with high chemical stability, low capacitive current and a large potential window [40].

1.5.1 P-type diamond

Boron doped p-type diamond exists in nature, [41] and the growth method for boron doped diamond is well established. Boron atoms are a similar size to carbon atoms, allowing them to substitute easily into the diamond lattice without deformation of the diamond lattice structure. Boron can easily be incorporated into the diamond lattice during CVD growth, by adding boron-containing gases such as diborane, B_2H_6, into the reactor chamber. The concentration of these dopants can be controlled by varying the boron concentration in the growth environment. Another characteristic for the substitutional incorporation of boron into the diamond lattice is a shallow acceptor state, with an activation energy of 0.37 eV [42]. This means less energy is required to ionise, and the efficient generation of holes can occur at room temperature.

Boron doped diamond (BDD), also exhibits superconductive properties [43]. Zhang et al., explores the electrical transport in nanoscale rings manufactured from heavily boron doped diamond. At high boron concentrations, BDD undergoes a transition from an insulating to a metallic state, leading to superconductivity at low temperatures. This superconductivity arises from the pairing of charge carriers (Cooper pairs) within the diamond's crystal lattice. Through leveraging the magnetoresistive properties of the BDD nanostructures, it may be possible to control superconducting currents more effectively, facilitating the emergence of groundbreaking designs in quantum computing and various other advanced technologies.

1.5.2 N-type diamond

However, n-type doping of diamond has proven to be more challenging [44]. Nitrogen is one of the most common impurities in both natural and synthetic diamonds [45]. It is the n-type equivalent to boron in p-type doping and can be introduced as a donor impurity with nitrogen being adjacent to carbon in the periodic table, having one more valence electron. However, this generates a deep lying donor level at 1.7eV below the diamond conduction band resulting in very low conductivity at 300 K [46].

Although nitrogen incorporation has shown to enhance the growth by factor of 2 [47] with diamond growth rates greater than 100 $\mu m\ h^{-1}$ being reported [48], the C-N bond is about 36%

larger than the C-C bonds along the (111) direction in diamond resulting in a distortion of the diamond lattice for high nitrogen concentrations [49].

While substitutional nitrogen easily enters the diamond lattice which is consistent with its negative formation energy of -3.4 eV. Pinault *et al.*, goes so far as to describes the use of nitrogen in n-type doping of diamond as 'useless' due to its deep lying donor level [46] . Due to the limitations of nitrogen doping, other avenues have been explored for n-type doping such as substitutional phosphorus-doped diamond and deuteration of boron doped diamond [50], in addition to the possibility of co-doping.

Lithium-ion implantation can transform intrinsic diamond into an n-type semiconductor [51], however, the high dose of implanting resulted in a heavily damaged graphitised layer [52]. Phosphorus doping is another impurity that has shown potential in n-type conduction with a donor level of 0.57 eV below the bottom of the conduction band of diamond [52,53]. Although producing a donor level 1.1 eV closer to the conduction band than nitrogen, the larger radius of phosphorus induces a large outwards lattice distortion [54], and the passivation of the donors due to the presence of hydrogen [55]. For heavily doped P-layers, required to decrease electrical resistance, a high efficiency of phosphorus incorporation is required, the current incorporation efficiency is still very low [56].

Co-doping is the combination of multiple defects to promote electron carrier concentration. The combination of two donors (D) and a single acceptor (A) in close proximity such as D—A—D will give rise to a single donor which is shallower than a single donor, D [57]. Previous computational work from the Bristol University Diamond Group explored the applicability of the co-doping of diamond for n-type conductivity combining both Boron and Nitrogen. Alex Croot et al, explored the formation of BN_2 and BN_3 clusters to achieve n-type conductivity [58]. This work followed on from other theoretical work that had previously provided insight into various combinations of elemental clusters that added an extra electron to the diamond lattice such as Katayama-Yoshida , H. et al. which introduced BN_2 clusters that produced a theoretical donor level of 1.17 eV, half an electron volt less than the 1.7 eV donor level of individual nitrogen [59].

However, this work has yet to be realised experimentally, with the formation of BN_2 and BN_3 clusters in diamond remaining a theoretical prediction rather than a practical achievement. Co-doping in this report is explored with the combination of both boron and nitrogen but other methods of co-doping diamond have been explored by researchers, investigating alternative dopant combinations to achieve n-type conductivity. Other examples of co-doping in diamond reported in the literature include Si-N_4, Li-N_x, Se-B, and B-H_x, which are primarily explored through theoretical studies with limited experimental evidence to date [60, 61, 62, 63, 64].

1.6 Diamond as a Semiconductor and viability for Betavoltaic applications

1.6.1 Diamond as a Semiconductor

Today there is an increasing demand for devices working at high power, high frequency and high temperature [65, 66]. Diamond, with its wide band gap of 5.47 eV, enables devices to operate at temperatures exceeding 500 K while maintaining low leakage currents. The high electron (4500 $cm^2/V\cdot s$) and hole mobility ~3800 $cm^2/V\cdot s$), allow for high-speed device operation, while its high breakdown voltage and low dielectric constant further support applications requiring extreme electrical performance [38]. Graebner et al., discusses the thermal conductivity of diamond, with diamond having the highest thermal conductivity of any known material at temperatures above 100 K. The thermal conductivity of diamond being 24–25 W cm^{-1} K^{-1} at 300K, compared to copper and silicon at 4 W cm^{-1} K^{-1} and 1.5 W cm^{-1} K^{-1}, respectively [67]. Moreover, diamond has controllable surface contamination, with some surface contaminants exhibiting a negative electron affinity [68]. Electrons in the conduction band have enough energy to cross the surface and be emitted into vacuum, a useful quality for electron emission applications.

In polycrystalline diamond films, the grain boundaries and numerous defects influence the conduction properties of the films and add an ambiguity to the results [69]. With continued advancements in CVD diamond, higher quality single crystal samples diamond films can be grown more readily. These are ideal for semiconductor applications due to their reduced recombination losses and improved manipulability of properties.

Diamond also has near tissue- equivalence due to its low atomic number ($Z = 6$) and chemical stability due to its strong covalent bonds [71]. It demonstrates exceptional biocompatibility, making it an excellent material for biomedical applications such as the aforementioned pacemakers. L. Tang et al. revealed that CVD diamond is as biocompatible as widely used surgical materials like titanium and 316 stainless steel [73]. However, unlike these metallic biomaterials, which can corrode over time and release metallic ions into host tissues, CVD diamond remains chemically inert, eliminating the risk of ion permeation. Furthermore, CVD diamond adsorbs and denatures significantly smaller amounts of fibrinogen, a key plasma protein involved in blood clotting. This property contributes to reduced cell adhesion and activation on its surface compared to titanium and stainless steel, as shown in both in vitro and in vivo experiments. These attributes, combined with its stability and resistance to degradation, position diamond as a superior choice for long-term biomedical implants.

1.6.2 Diamond Betavoltaics

In terms of betavoltaics, diamond is incredibly radiation hard, and it has been found to remain unaffected after doses of 6.8 MGy of 10 keV photons [70]. As well as being highly radiation tolerant to photons, diamond has higher radiation hardness against protons and neutrons than silicon. The small atomic number ($Z=6$) of carbon is less likely to be damaged by the same photon flux (radiation) compared with other semiconducting materials [71]. Adam et al., even goes on to suggest that high quality CVD Diamond is a nearly ideal material for detecting ionising radiation [72] .

Recent betavoltaic designs utilise Ni-63 or tritium (H-3) as the radioactive source. Bormashov et al., reports a prototype betavoltaic battery consisting of stacked layers of 200 single cells. Schottky barrier diamond diodes stacked in conjunction nickel foils, achieving a total maximum power output of 0.93 μW for a total device volume of 87.5 mm^3, and a device output power density of approximately 10 $\mu W/cm^3$ [3]. Similarly, in 2016, Delfaure and Pomorski et al., successfully fabricated a P-doped/Intrinsic/Metal (P-i-M) diamond device. A large area single crystal diamond membrane was used, reporting one of the highest open-source voltages at 1.85 V and a high total conversion efficiency of 9.4% [74]. The structure was tested under a 20 keV electron-beam irradiation using a scanning electron microscope to simulate the energy of beta particles emitted by Ni-63. The current-voltage (I-V) characteristics are shown in Figure 12.

Most akin to this thesis is the work of Shimaoka et al., which explores the energy efficiency of a diamond pn junction, also characterised under electron-beam irradiation [75]. The study observed an open-circuit voltage of 4.26 V and a semiconductor conversion efficiency of 28%, close to the theoretical Shockley–Queisser efficiency limit for betavoltaic cells [76]. Unlike this project however, the p-type dopant used was phosphorus, the device did not contain an intrinsic layer and was grown on a single crystal diamond substrate. The structure and I-V characteristic of the device are shown in Figure 11. Bormashov's and Delfaure's work on Schottky barrier diodes (SBD) is discussed within Shimaoka et al. It indicates that a limiting factor to the conversion efficiency of these devices is the barrier height being at ~2 V, almost half the built-in potential of a diamond pn junction. This built-in potential is discussed further in section **4.4.1 Diode 1**.

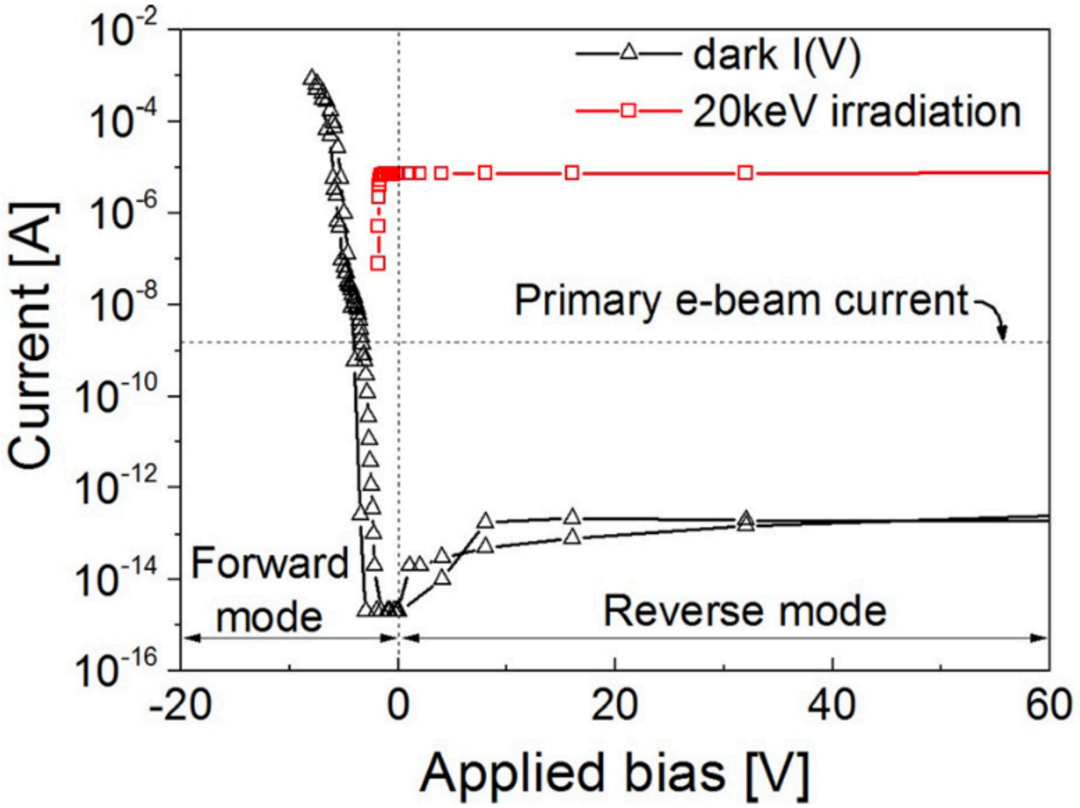

Figure 12 - The current-voltage characteristic of the P-i-M single crystal CVD diamond membrane. The black triangles represent dark characteristics, while red squares correspond to measurements under 20 keV electron beam illumination. The primary SEM beam current measured at 5.19 nA using a Faraday cup, is indicated in the graph by the horizontal black dashed line. The graph is sourced from [89]

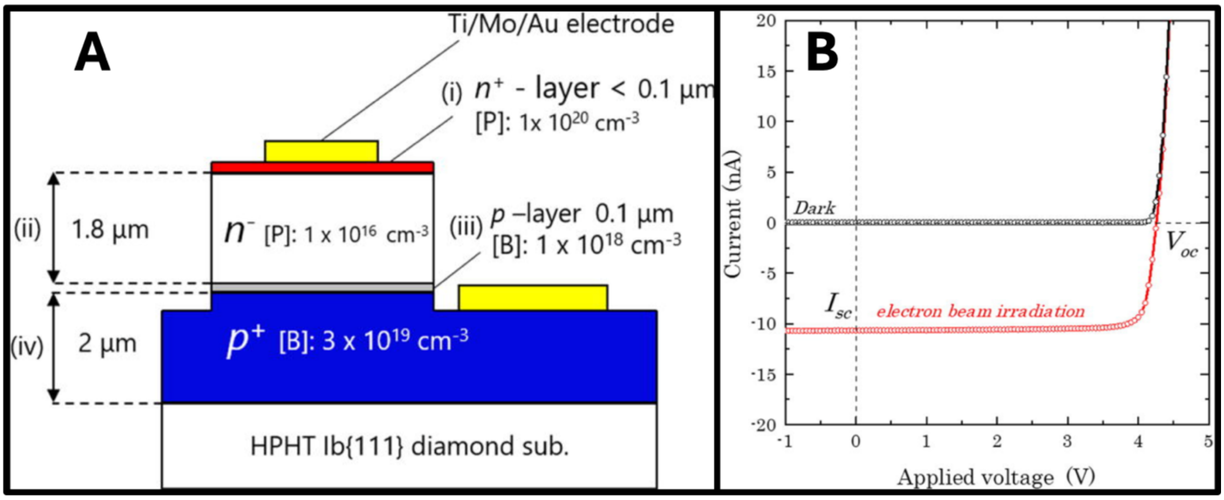

Figure 11 - [A] Schematic of the pn junction diamond diode. [B] The current-voltage characteristic of the pn junction diode at an acceleration voltage of 15 kV. Both diagrams are sourced from [75].

1.7 Aside on Radionuclides

Many radionuclides emit beta particles. However, the energy of the electrons can often be high and cause damage to the semiconductor lattice [13]. Tritium, nickel-63, and promethium-147 and carbon-14 are some of the only beta-emitting isotopes whose maximum beta energy is below 300 keV and whose half-life is sufficiently long enough to facilitate a long-life power source [14, 16].

Tritium, H-3, is a radioactive isotope of hydrogen, consisting of one proton and two neutrons, and a half-life of 12.35 years [77]. Tritium is produced artificially through the irradiation of lithium [78] and is a low abundance byproduct of nuclear facilities, whereby in heavy water reactors, neutron activation of deuterium occurs. Natural tritium is produced through cosmic-ray-induced nuclear reactions in the atmosphere; however, this is a smaller proportion of the environment [79]. Nickel-63 is a radioactive isotope of nickel produced through the neutron activation of stable nickel-62 in a nuclear reactor, nickel is present in Inconel and stainless steel [80]. Carbon-14 is a radioactive isotope of carbon, with a half-life of 5700 years, its production was discussed in 1.1 Betavoltaic Devices. The beta decay energy level schemes and equations are shown in Figure 13 data sourced from the NuDAT database [81].

The beta decay process is governed by the weak nuclear force. The resultant emitted electron will interact with the semiconducting pin junction, generating an electron-hole pair. When the beta particles create the electron-hole pairs, electrons are swept towards the n-side and holes towards the p-side, generating a flow of current.

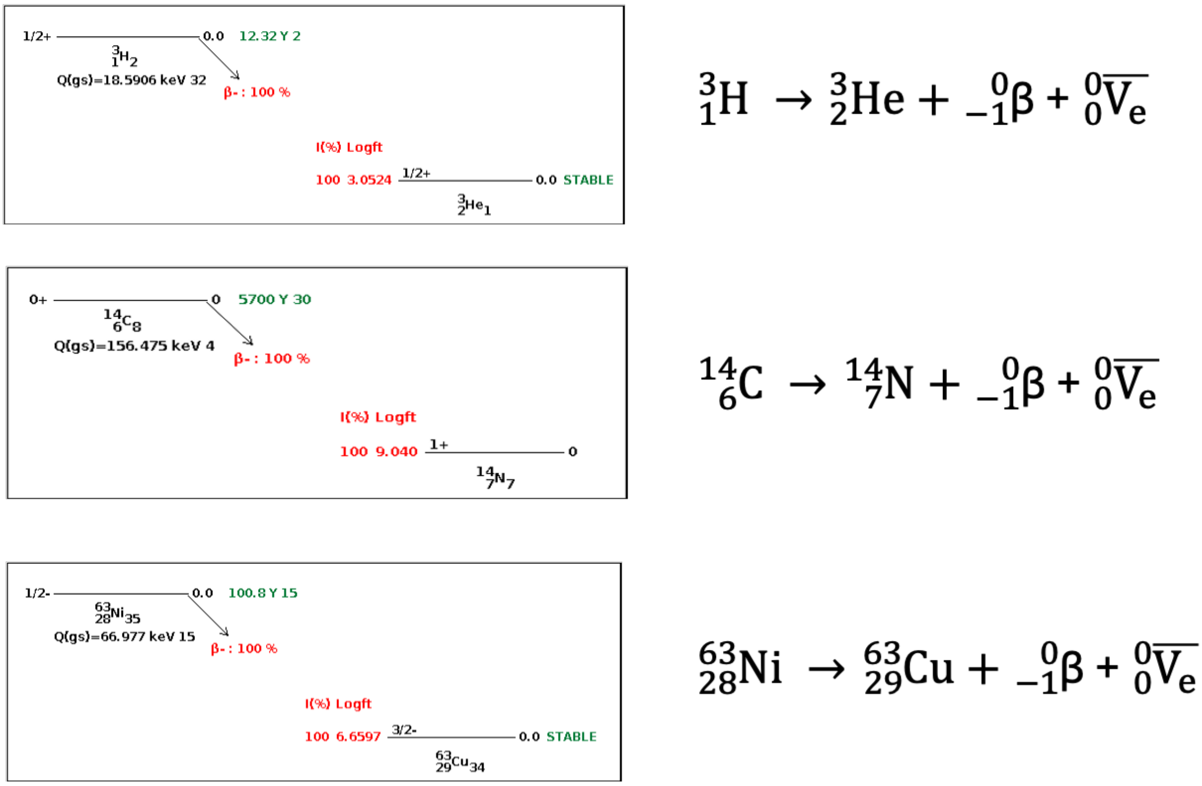

$$^{3}_{1}\mathrm{H} \rightarrow {}^{3}_{2}\mathrm{He} + {}^{0}_{-1}\beta + {}^{0}_{0}\overline{\mathrm{V}_{e}}$$

$$^{14}_{6}\mathrm{C} \rightarrow {}^{14}_{7}\mathrm{N} + {}^{0}_{-1}\beta + {}^{0}_{0}\overline{\mathrm{V}_{e}}$$

$$^{63}_{28}\mathrm{Ni} \rightarrow {}^{63}_{29}\mathrm{Cu} + {}^{0}_{-1}\beta + {}^{0}_{0}\overline{\mathrm{V}_{e}}$$

Figure 13 - Tritium decays into helium-3, a light stable isotope of helium, an electron (beta particle) and an electron antineutrino are also emitted. Carbon-14 decays into nitrogen-14 and nickel-63 into copper-63. Both decays produce stable isotopes, a beta particle and an electron antineutrino.

1.8 Aim of the thesis

The primary objective was to utilise microwave plasma enhanced CVD techniques to grow and fabricate diamond P-i-N junction diodes. Secondly, to characterise and evaluate the current-voltage (I-V) characteristics of the produced diodes and assess their electrical performance. Additionally, the study explored the potential of co-doping with boron and nitrogen to achieve an n-type layer at room temperature, though this aspect remained a secondary focus.

This comprehensive approach aimed to advance understanding and improve the performance of diamond p-i-n junction betavoltaic diodes.

2 Experimental

2.0 Device summary:

Table 1 – Comprehensive summary of fabricated P-i-N diodes. In total 5 devices were fabricated throughout the duration of this project.

Device number	Growth substrate + (Diode Structure, I or II)	p-layer growth time (Boron)	i-layer growth time	n-layer dopant and growth time (mins)	IV Response (summary)
1	Undoped TM180 polycrystalline diamond (I)	5 hours	40 mins, *ex situ*	Nitrogen (15+30)	Diode
2	Undoped TM180 polycrystalline diamond (I)	5 hours	40 mins, *ex situ*	Boron and nitrogen (15) Nitrogen (30)	Ohmic (low resistance)
3	Boron doped Element six polycrystalline diamond (I)	n/a	40 mins, *in situ*	Nitrogen (15+30)	Ohmic (high resistance)
4	Undoped TM180 polycrystalline diamond (II)	5 hours	40 mins, *in situ*	Nitrogen (15+30)	Diode
5	Undoped TM180 polycrystalline diamond (II)	5 hours	80 mins, *in situ*	Nitrogen (15+30)	Ohmic (poor contacts)

2.0.1 Diode Structure I

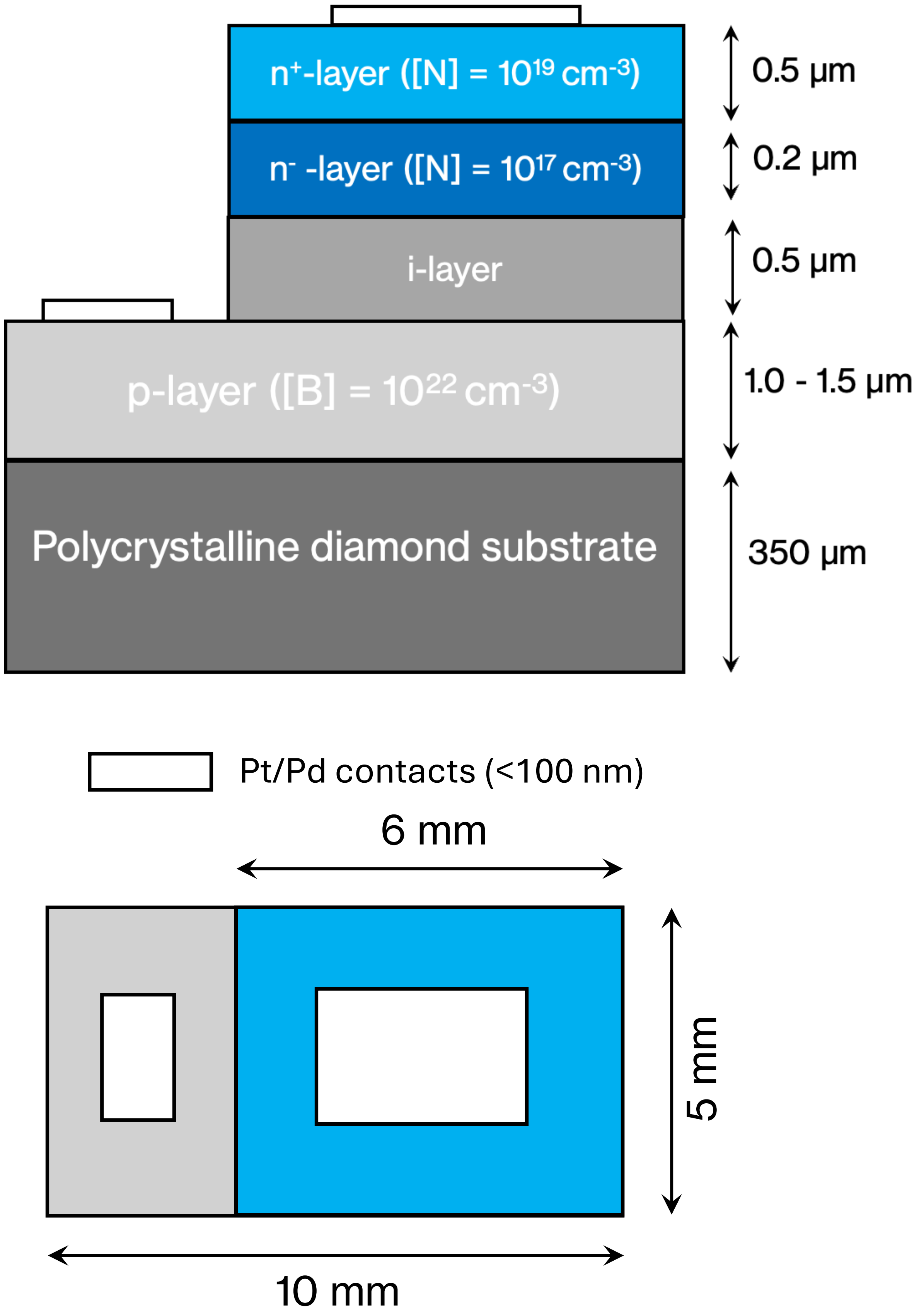

Figure 14 – [Top] A schematic of Diode Structure I; a pseudo-vertical structure grown on a PCD substrate. [Bottom] A top-down view of the constructed device.

2.0.2 Diode Structure II

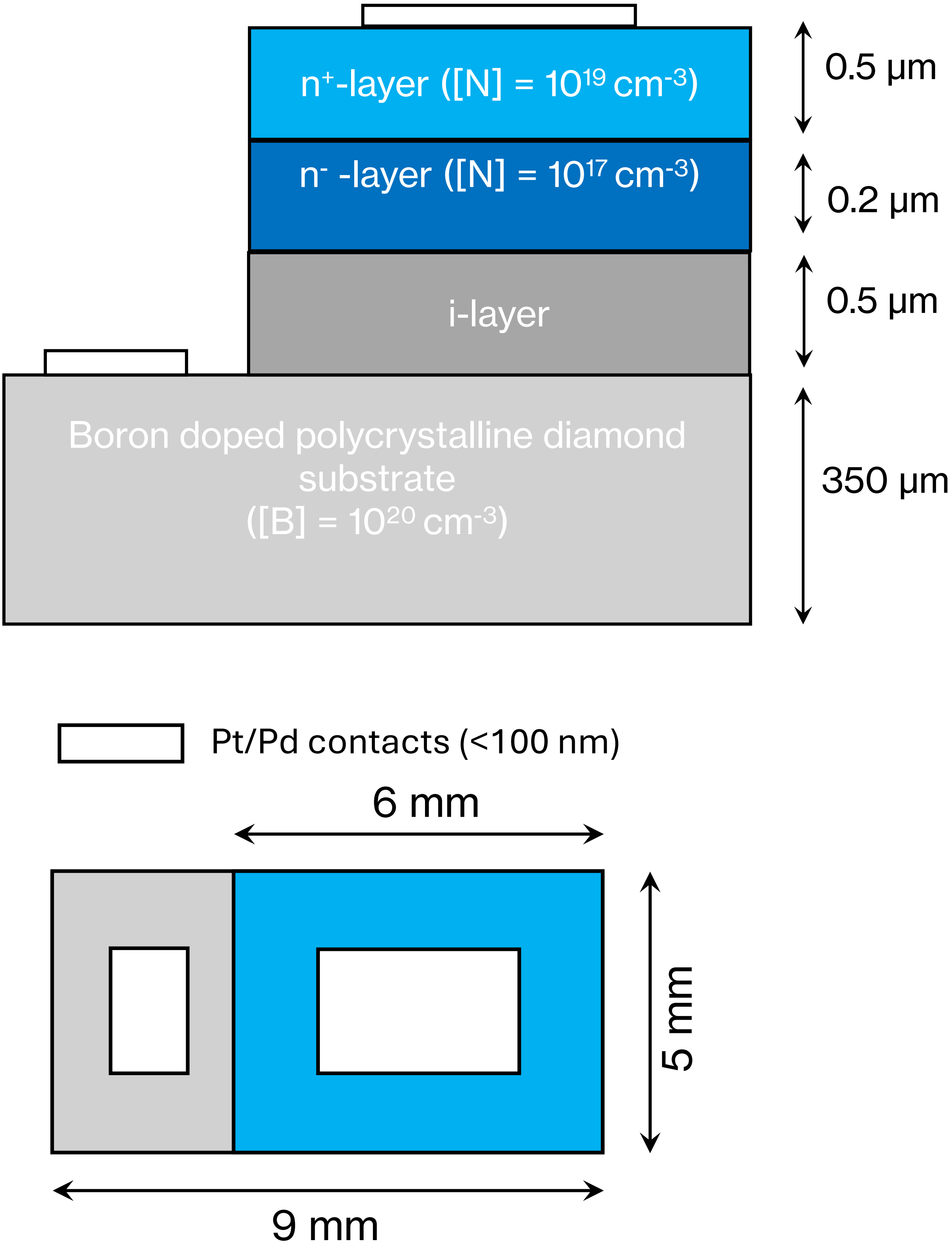

Figure 15 – [Top] A schematic of Diode Structure II; a pseudo-vertical structure grown on a boron doped PCD substrate. [Bottom] A top-down view of the constructed device.

2.0.3 Process Overview

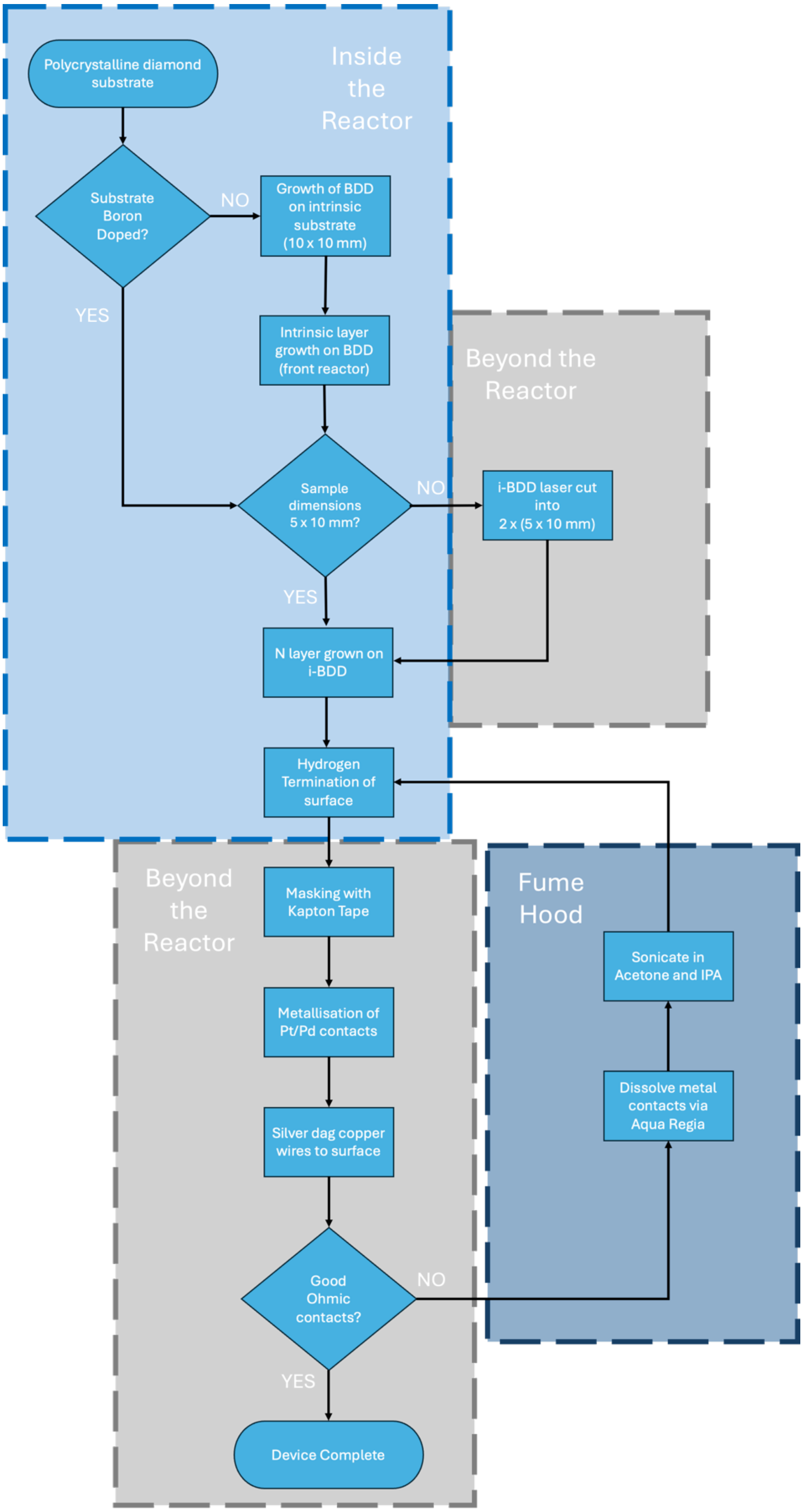

Figure 16 - A flowchart for the fabrication procedure. The process is split into three main categories: ‘Inside the reactor’, ‘Beyond the rector’ and ‘Fume hood’.

Emissivity is a measure of a material's ability to emit thermal radiation, defined as the ratio of energy radiated from the material's surface to that of a perfect black body. It ranges from 0 to 1, where 0 represents a perfect reflector and 1 corresponds to an ideal black body, which absorbs and emits all incident radiation.

For this study, the emissivity of all polycrystalline diamond (PCD) was set to 0.15 and temperatures were measured using a single-colour optical pyrometer ($\lambda = 2.2$ µm).

2.1 Substrate and P-layer Growth

Homoepitaxial growth of boron doped diamond (BDD) were initially conducted to create a p-layer on a TM180 PCD substrate from Element Six. This was conducted using an Applied Science and Technology (ASTeX)-type MWCVD reactor colloquially known as the 'back reactor'. The PCD substrate was centred on a tungsten disk, which was placed on a thin spacer wire of molybdenum (Mo) with a diameter of 8 milli-inches. This spacer wire was positioned above the water-cooled reactor baseplate, minimising the thermal contact between the disk and the baseplate.

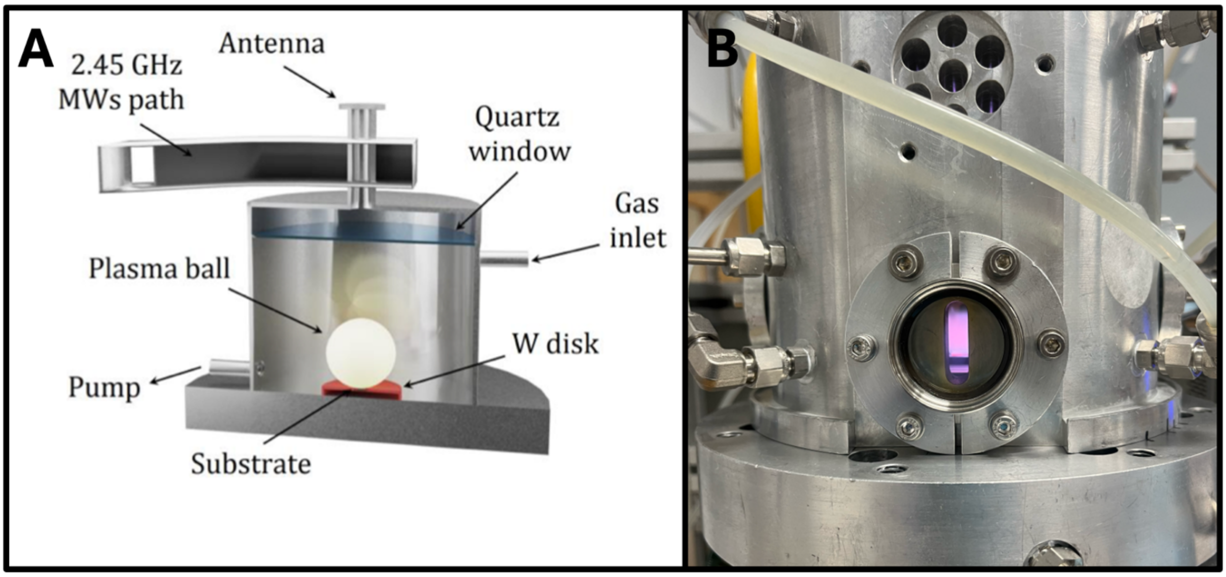

Figure 17 - [A] Vertical cross section of a Microwave plasma-enhanced CVD from Zulkharnay [82] [B] Plasma ball seen through a lateral quartz window during a hydrogen plasma treatment.

The diamond growth began by lowering the reactor chamber pressure to approximately 20 mTorr. Hydrogen gas, H_2, was introduced into the chamber at 300 sccm. The activation of the gaseous species occurs through a plasma ball located directly above the substrate; however, the plasma must be first created before this can occur. The striking conditions for hydrogen plasma were 0.15 Torr and 0.7 kW.

Once a stable plasma had formed, the pressure was gradually increased to 50 Torr. The process was slow to minimise the sample etching from the bombardment of electrons and ions within the plasma. Once stable the other reactants gases, 12.5 sccm of methane (CH_4) and 0.5 sccm of diborane (B_2H_6) were then introduced into chamber. The diborane gas mixture contained 5% diborane in hydrogen. The gas flow rates of the process gases were monitored and regulated by an analogue mass flow control (MFC) panel.

With the plasma stable and the reflected power low (< 0.02 kW), the pressure and power were then both increased stepwise to 100 Torr and 1 kW, respectively. The plasma was continuously monitored throughout the growth process to ensure it remained stable and that the plasma was situated over the substrate, in the centre of the chamber.

Table 2 - The conditions used for the p-layer growth in the back reactor.

H_2 Flow / sccm	CH_4 Flow / sccm	B_2H_6 Flow / sccm	Power / kW	Pressure / Torr	Temperature / °C	Time / Hours
300	12.5	0.5	1.0	100	900 - 1000	5

This was the initial growth procedure for all diodes apart from diode 3, which began with a free-standing boron doped polycrystalline diamond substrate from Element Six.

2.2 Intrinsic-layer Growth

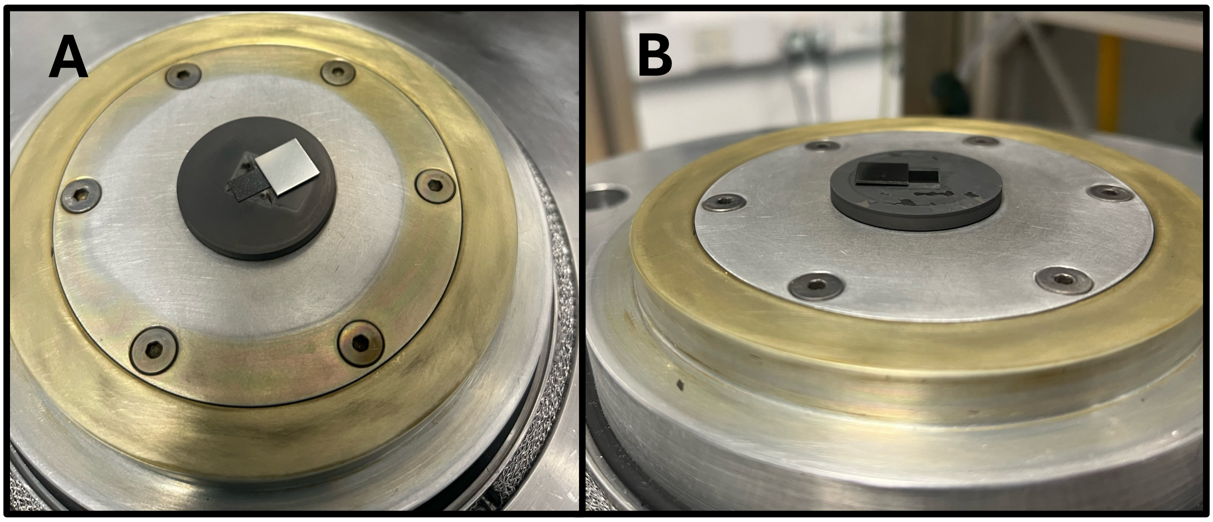

Figure 18 - [A] Top-down view of the molybdenum mask on Diode 4. [B] Side-on view of a molybdenum mask on Diode 3, supported by a piece of silicon.

Boron introduction into the reactor is an irreversible process, contamination of subsequent samples is unavoidable. This is known as the “memory effect” whereby boron oxide is deposited on reactor walls and the quartz window to then be re-introduced gradually to the gas phase [83]. Therefore, subsequent growths were undertaken in a newer ASTeX MWCVD reactor colloquially known as the ‘front reactor’. Consequently, there is a large increase in both reactor pressure and microwave power. (See Table 3)

Prior to the growth of the intrinsic diamond, the p-layer was masked using a clean molybdenum (Mo) sample. Molybdenum is a refractory metal with low emissivity and absorption of radiation [83]. This made it a great material to mask the surface of the diode limiting new diamond growth. This restricted growth, resulted in step formation and established the pseudo vertical structure for all diodes. To achieve this, approximately 3 mm of the substrate surface was covered with the Mo mask, which was supported by scrap silicon as shown in Figure 18.

The method for the intrinsic diamond growth followed a similar approach to 2.1, with slight alterations to the reactor conditions. Firstly, a change in the gaseous species with no diborane used in intrinsic diamond growth. Secondly, there was an increase in both chamber pressure and microwave power from 100 Torr and 1 kW, 140 Torr and 1.4 kW, respectively. Finally, in the front reactor, the MFC panel was digital rather than analogue, used to precisely monitor and regulate gas flow rates.

Table 3 - The conditions used for the intrinsic layer growth in the front reactor.

H_2 Flow / sccm	CH_4Flow / sccm	Power / kW	Pressure / Torr	Temperature / °C	Time / mins
300	12.5	1.4	130	~ 900	40

2.3 Lasers micromachining apparatus

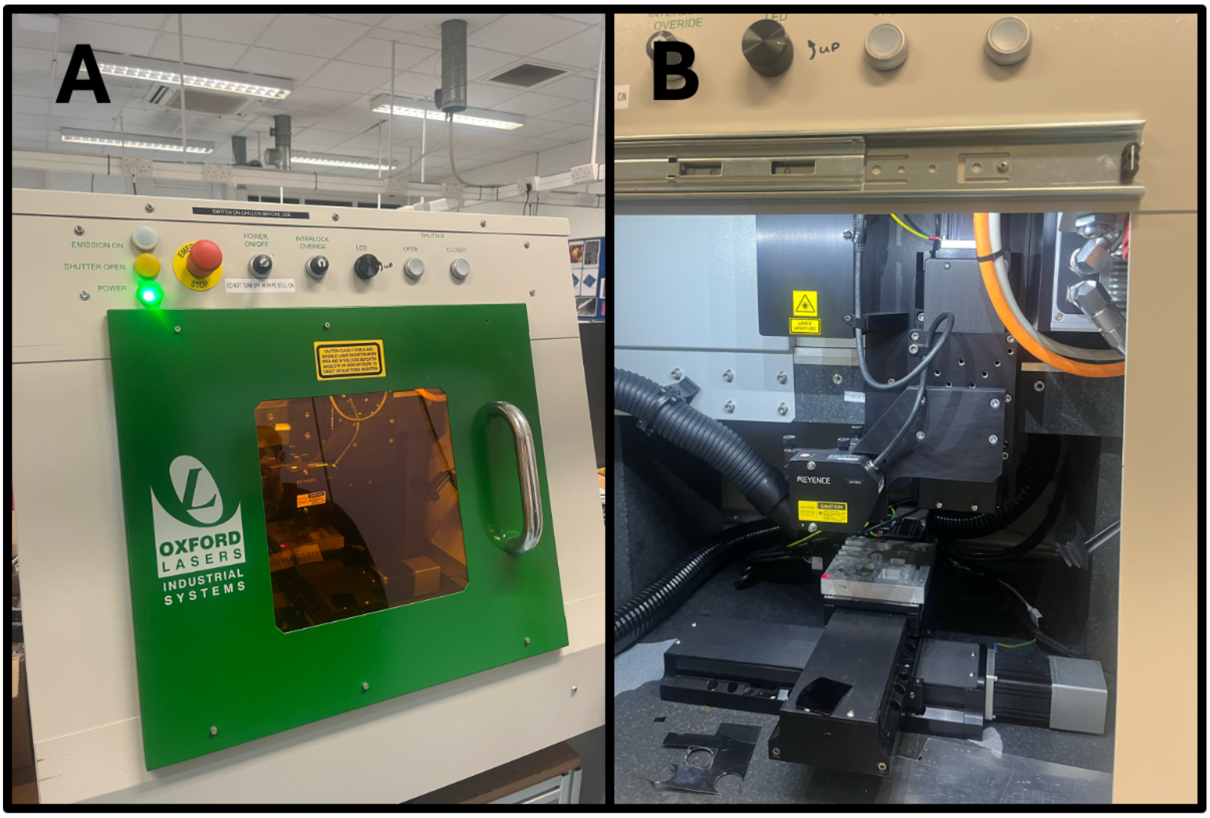

Figure 19 - [A] Photograph of the exterior of the laser micromachining apparatus. [B] Photograph of the interior of the laser micromachining apparatus and adjustable stage

The Oxford Lasers industrial systems micromachining apparatus (Alpha 532, Oxford Lasers Ltd.) was used to cut existing 10 × 10 mm substrates into smaller 5 × 10 mm substrates. The adoption of a smaller substrate size not only improves growth uniformity but also leads to a more economical process, with a greater number of diodes being produced with less substrate material.

The micromachining tool employs a diode-pumped nanosecond laser (Nd:YAG) with a wavelength of 542 nm as the base laser source. The sample is positioned on an adjustable stage equipped with embedded servomotors, allowing precise movement along the x, y, and z directions. The system is controlled using Cimita software, which operates through G-code to regulate both servomotor motion and laser parameters. A programmed etching process is executed to continuously ablate a vertical line through the centre of the substrate, progressively splitting it into two 5 × 10 mm samples. The laser operates at a pulse frequency of 20 kHz, using 90% of its maximum power, an etch speed of 2 mm s^{-1} and a minimum achievable cut width.

It is important to note that for Diode 4 and Diode 5, the laser cut occurred before the intrinsic diamond growth and that the growth of both the intrinsic layer and the n-layer were completed in situ.

2.3 N-layer Growth

The growth of the n-type layer was carried out in the front reactor, with similar reactor conditions to the intrinsic diamond growth in the previous section. Similarly, a molybdenum sample was used to maintain the step of the pseudo vertical structure, ensuring it remained a pristine p-type region.

Table 4 - The conditions used for the n-layer growth in the front reactor.

Layer	N_2 Flow / sccm	H_2 Flow / sccm	CH_4Flow / sccm	Power / kW	Pressure / Torr	Temperature / °C	Time / mins
n-	0.3	300	12.5	1.4	130	~ 900	15
n+	4	300	12.5	1.4	130	~ 900	30

The growth of the n-layer was divided into two distinct layers; an n- (minus) layer and an n+ (plus) layer. The n- being of smaller growth thickness and having a lower nitrogen concentration. Initially the nitrogen (N_2) flow rate was set to 0.3 sccm, and after 15 minutes, was then increased to 4 sccm. With a slight increase in gas volume, minor temperature fluctuations were observed, however the overall reactor temperature remained stable. All other growth parameters remained constant throughout the CVD process. The deposition continued for a total duration of 30 minutes. As described in Section 2.1, the plasma was continuously monitored, and gas flow rates were regulated using a digital MFC.

These growth conditions remained constant for all diodes except Diode 2, which underwent a modified process incorporating a co-doped n-layer consisting of both boron and nitrogen. Due to the inclusion of boron, this growth was conducted in the back reactor.

Table 5 - The conditions used for the n-layer growth in the back reactor (Co-doping of boron and nitrogen). Higher Hydrogen and Methane flow rates to dilute the diborane concentration in the chamber.

Layer	B_2H_6 Flow / sccm	N_2 Flow / sccm	H_2 Flow / sccm	CH_4 Flow / sccm	Power / kW	Pressure / Torr	Temperature / °C	Time / mins
n-	0.4	0.3	500	25	1.0	100	~ 1000	15
n+	0.0	1.1	500	25	1.0	100	~ 1000	30

To account for the introduction of nitrogen into the back reactor growth environment, the overall flow rates of hydrogen and methane were increased to 500 sccm and 25 sccm, respectively. As with previous growths, the n-layer growth was divided into two distinct layers. After 15 minutes the gas flow rates were adjusted; the diborane. (B_2H_6) flow rate was reduced to 0.0 sccm and the nitrogen flow rate was increased from 0.3 sccm to 1.1 sccm. Despite stopping the flow of diborane, background contamination from the reactor's memory effect contributed to residual boron incorporation into the n+ layer. These conditions were selected based on the results of B. Nutbrown's 2024 thesis [84].

2.4 Hydrogen Surface Termination

Before the metallisation of the device, the diamond surface must be hydrogen terminated to ensure proper adhesion and a homogenous contact to the diamond surface. Hydrogen termination of the diamond surface of all devices was carried out in the front reactor, using a pure hydrogen plasma in a multistep process.

The sample was exposed to a pure hydrogen plasma environment with a constant flow rate of 300 ± 10 sccm. The process began at a pressure of 140 Torr with a microwave power of 1.4 kW, during which the samples were heated to temperatures of approximately 900°C for 2 minutes. This high temperature treatment (>700 °C) was sufficient to desorb any surface hydrocarbons, oxygen and even hydrogen itself [85]. Lowering the microwave power to 1 kW and reducing the chamber pressure to 100 Torr for another 2 minutes allowed for the hydrogenation of the diamond surface at a temperature range of 500 – 600°C. With hydrogen readily chemisorbing to the surface on diamond at temperatures above 400°C [86], hydrogenation of diamond can be achieved simply by subjecting diamond to this high-temperature hydrogen gas. Hydrogen atoms incident on the diamond surface can refill vacant sites, etch surface graphite and the adsorbed hydrogen stabilises the diamond surface structure [87].

In the final step, the pressure was further reduced to 30 Torr and the microwave turned off, allowing the sample to cool for 2 minutes in a hydrogen environment. The adsorption of hydrogen continues during this cool down period [89]; the hydrogen atmosphere prevents the adsorption of oxygen and other contaminants to the surface.

Table 6 -The stepwise process for hydrogen termination, step 2 at approximately 600 °C is the key step for hydrogenation.

Hydrogen Flow / sccm	Time / mins	Pressure / Torr	Power / kW	Temperature / °C
300	2	140	1.4	~900
300	2	90	1	~600
300	2	30	0	~40

2.5 Preparation for Metallisation

Kapton tape is a polyimide film commonly used in the electronics industry.
Used in flexible printed circuits, protecting sensitive electronic components during the manufacturing processes. The devices were masked using Kapton tape cut to fit each device by hand, creating two smaller rectangles on the surface of the sample, as shown in Figure 20. This process must be completed with a careful haste to avoid surface contamination but also reduce the surface exposure to the atmosphere. Otherwise, the surface must be cleaned and hydrogen termination repeated.

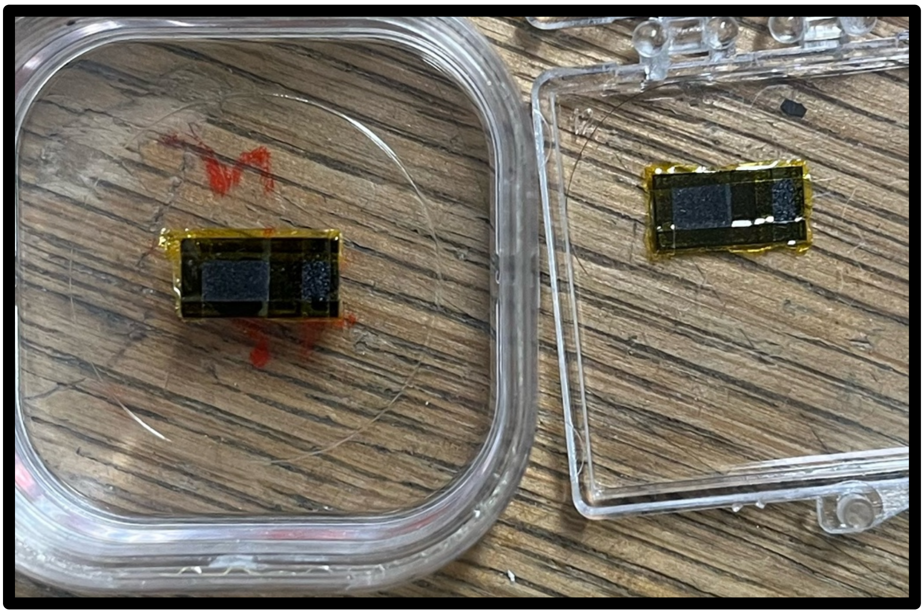

Figure 20 - A photograph of Diode 4 and Diode 5 masked with Kapton tape before metallisation

2.6 Metallisation and Wiring

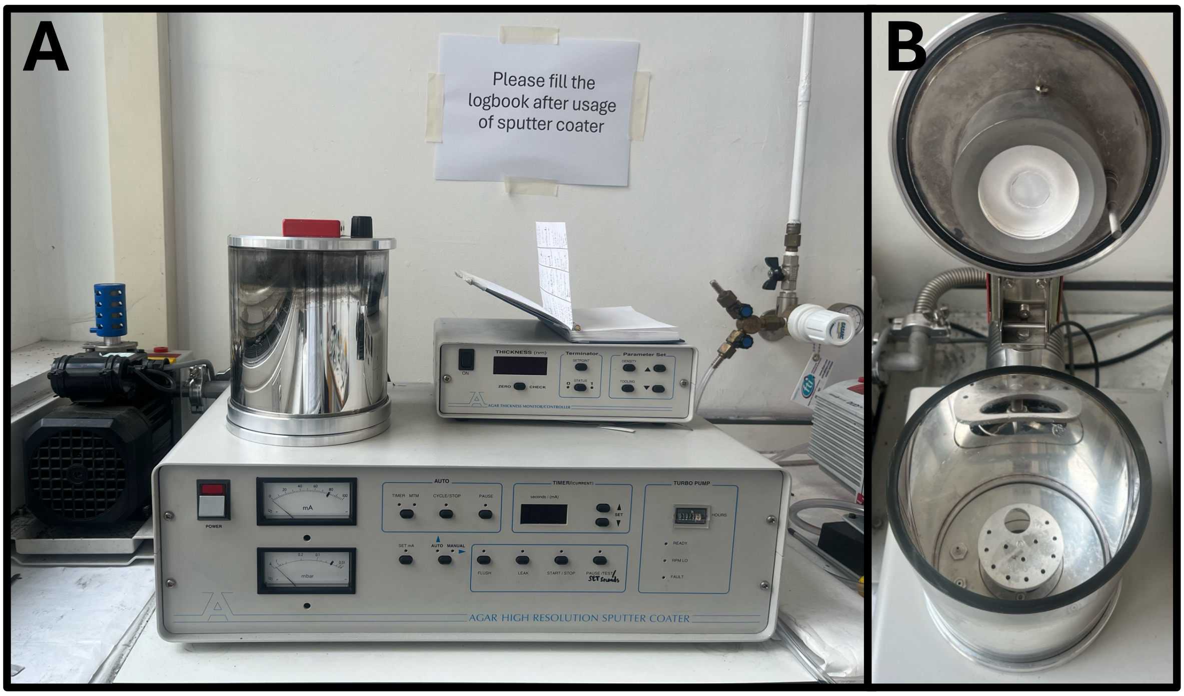

Figure 21 - [A] A photograph of the AGAR High Resolution Sputter Coater. [B] A photograph of the inside of the chamber of the sputter coater and the metal target disk.

The Platinum-Palladium (Pt/Pd) ohmic contacts were sputtered onto the diamond sample surface using an AGAR High Resolution Sputter Coater. The sample was placed on the base of the chamber; Pt/Pd target was used for deposition, screwed into the top of the coater as shown in Figure 21B. The chamber was first evacuated to a base pressure of 5×10^{-2} mbar before introducing argon gas at a controlled flow rate. A high voltage is applied to ionise the gas, creating plasma composed of positively charged argon ions and free electrons. These ions are accelerated toward the negatively charged target, causing Pt/Pd atoms to be ejected via sputtering. The ejected atoms are deposited onto the diamond sample surface, forming a uniform metallic coating. Sputtering was performed using a planar magnetron source, with plasma ignition at 80 mA in a high-vacuum environment. The deposition was carried out for a total sputter time of 300 seconds to ensure uniform metallisation, at a sputter rate of approximately 20 nm min^{-1}.

While a Pt/Pd target was used in this process, the sputter coater is typically equipped with a silver target for SEM applications, particularly for non-conductive species.

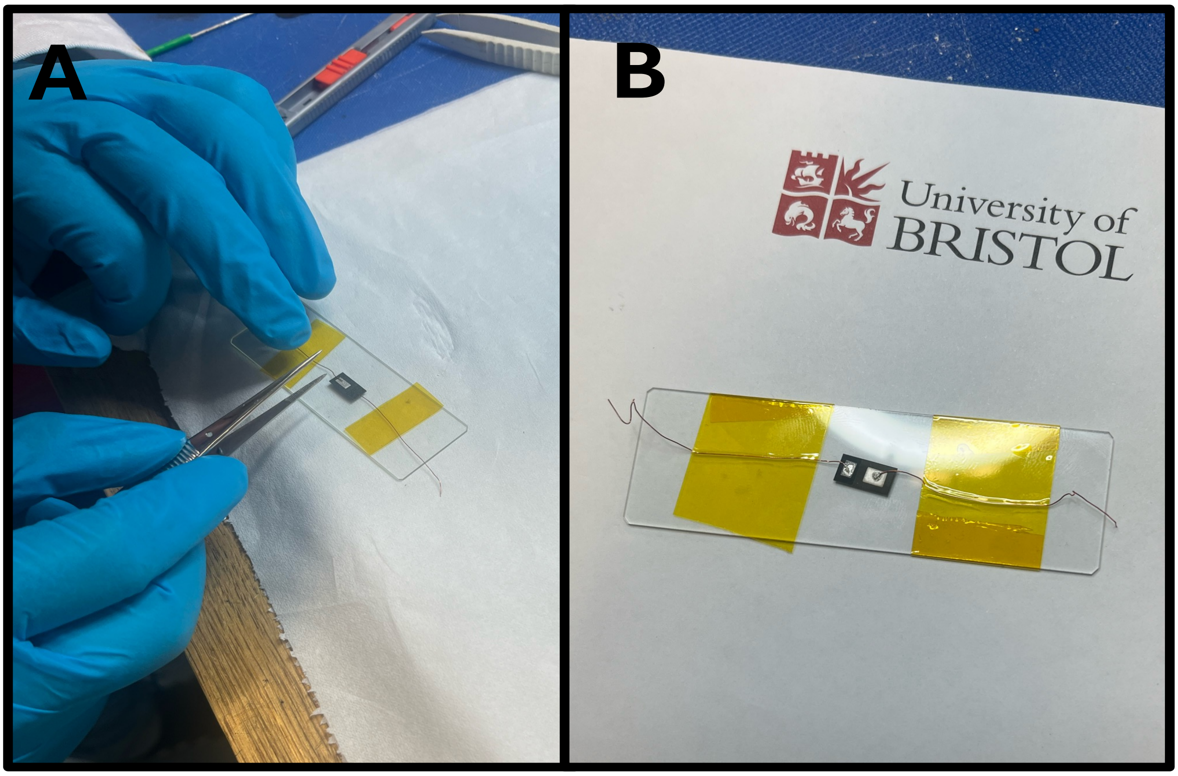

Figure 22 - [A] A photograph of the copper wires being attached to the Pt/Pd contact of Diode 1. [B] A photograph of Diode 3 being left to dry for 24 hours after the silver DAG had been successfully applied.

After sputtering was completed, the sample was transported back to the diamond laboratory workbench where copper wires were attached, to facilitate electrical contacts for measurement. Copper wires were first cleaned using acetone and isopropanol (IPA) to remove any surface contaminants. The cleaned wires were then secured to a glass slide with Kapton tape for ease of handling. The wires were attached to the Pt/Pd metal contacts using Silver-doped adhesive grease (silver DAG), a conductive paint composed of silver particles and an organic binder. To achieve optimal adhesion, the contact surface was kept clean, and the wire was carefully positioned to make direct contact with the Pt/Pd layer only. The device was then left undisturbed for 24 hours to allow the silver DAG to dry and harden, enhancing the durability and stability of the electrical contacts.

If the metal contacts are bad as shown in Figure 24, The device surfaces were cleaned and the metal contacts dissolved via aqua regia [$HCl + HNO_3(3 + 1)$]. This is a highly corrosive solution that effectively dissolved the silver DAG and Pt/Pd contacts without etching or damaging the diamond surface. Due to the hazardous nature of strong acids, this process was conducted inside a fume hood. The sample was then sonicated in acetone, removing any organic solvents, followed by IPA to remove any remaining contaminants. The surface then underwent hydrogen termination as shown in '2.0 Process Overview' and the metal contacts were refabricated.

The structure for the final devices followed either structure I or II (Diode 3) as shown in 2.0.1 Diode Structure I and 2.0.2 Diode Structure II.

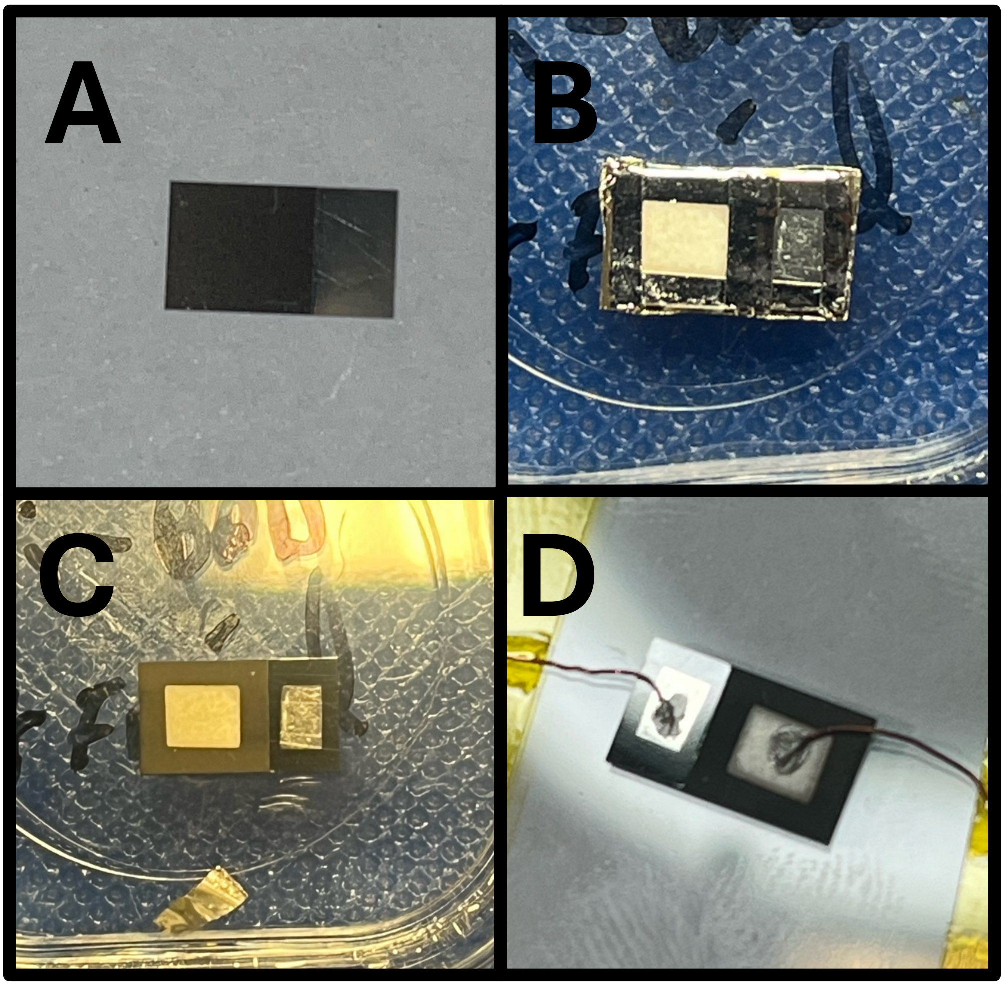

Figure 23 - A series of photographs demonstrating a diodes journey 'Beyond the reactor' [A] Diode 3 after the growth process, before metallisation. [B] Diode 3 immediately after metallisation, before Kapton tape was removed. [C] Kapton tape now removed, leaving behind rectangular Pt/Pd contacts. [D] Copper wires now attached using silver DAG. Device complete!

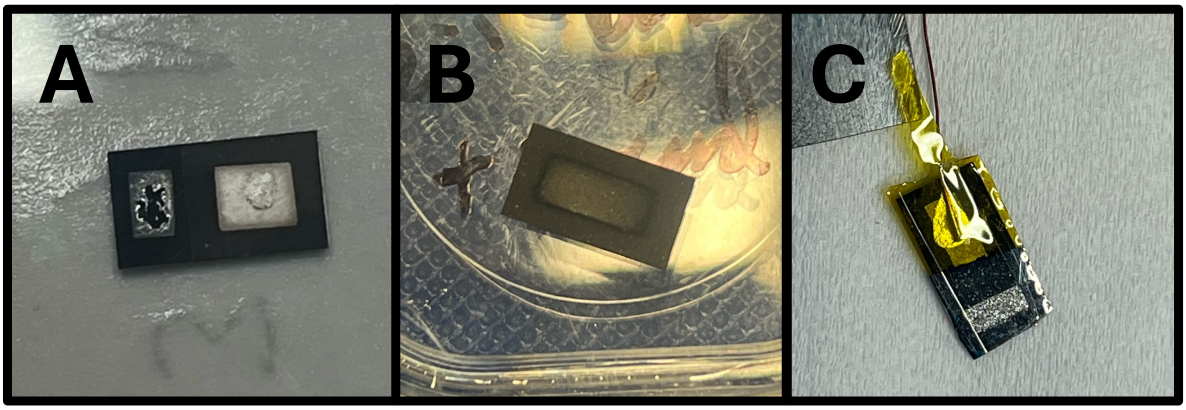

Figure 24 - [A] A photograph of the topside of Diode 3 after the application of silver DAG had partially removed the Pt/Pd contact. [B] A photograph of a poor stutter onto the backside of Diode 3. [C] A photograph of a poor application of silver DAG, spreading over the metal contact and onto the diamond surface.

2.7 Complete Device and Analysis

Once the diode was fabrication and wires attached, readings could successfully be undertaken. The device was connected to the Keithley 2401 via crocodile clips. The Keithley 2401 is a 20V, 1A, 20W Source Measurement Unit (SMU) designed for precise voltage and current sourcing, as well as high-accuracy measurements. With a resolution ranging from 10 pA at 1 µA to 10 mA at 1 A [90] , it serves as a compact, single-channel DC parametric tester ideal for device characterisation. By applying short voltage pulses, the instrument enables the measurement of resistance and capacitance in the fabricated diode devices of this project.

The data was recorded using a Python script written by Dr Robbie Mackenzie, saved in CSV format and later processed in a separate script written by myself. The CSV file was converted into a DataFrame where it could be more easily manipulated. I-V characterisation and current density plots generated, where the properties such as threshold voltage and rectification ratio of the diodes could be analysed.

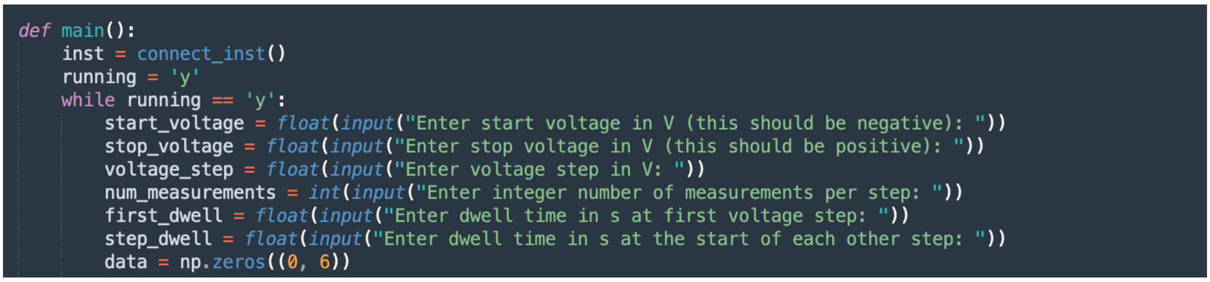

```
def main():
    inst = connect_inst()
    running = 'y'
    while running == 'y':
        start_voltage = float(input("Enter start voltage in V (this should be negative): "))
        stop_voltage = float(input("Enter stop voltage in V (this should be positive): "))
        voltage_step = float(input("Enter voltage step in V: "))
        num_measurements = int(input("Enter integer number of measurements per step: "))
        first_dwell = float(input("Enter dwell time in s at first voltage step: "))
        step_dwell = float(input("Enter dwell time in s at the start of each other step: "))
        data = np.zeros((0, 6))
```

Figure 25 - A screenshot of the input statements of the code used to record data on the Keithley 2401.

For most diodes, the potential difference was swept from -20 to 20 V in voltage steps ranging from 0.1 V to 0.5 V. A compliance limit of 1.05 mA was set to prevent damage by limiting the total power dissipation. Measurements began after an initial dwell time of 5 seconds, with a dwell time of 2 seconds set between voltage steps. At each step, 3-5 measurements were recorded, resulting in a total of 240 to 1,000 data points across the full voltage range.

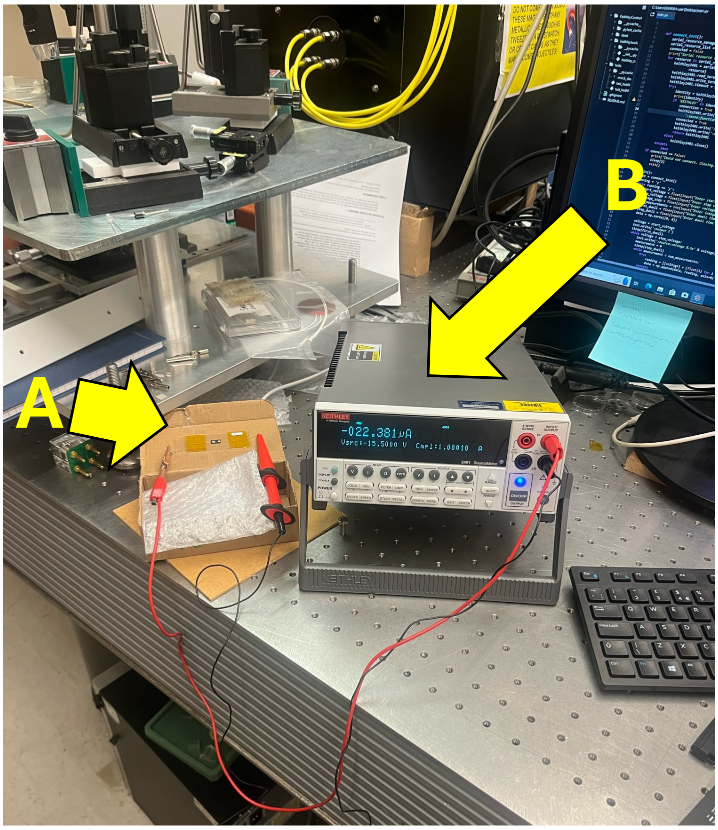

Figure 26 - A photograph of a typical I-V measurement setup. [A] Diode connected via crocodile clips. [B] The Keithley 2401 SMU taking measurements

2.8 Other Experimental Sample Preparation

Figure 27 - [A] Photograph of a repurposed Edwards S150A sputter-coater. [B,C] Close-up photographs of the equipment running and the purple oxygen plasma.

Before the intrinsic diamond and n-layer growth of diode 5 was conducted, the BDD layer was oxygen terminated. The sample was exposed to a an O_2 plasma, using a repurposed sputter coater (Edwards S150A). The plasma chamber consists of two parallel stainless-steel plates separated by 1 cm, serving as the powered (upper) electrode and the grounded (lower) electrode in a DC configuration. To initiate the process, the chamber was evacuated to 20 mTorr before introducing O_2 at a flow rate of 10 sccm. The pressure was then manually adjusted to 1 Torr, as monitored by a Baratron capacitance manometer, as shown in Figure 27B. Plasma was ignited at 65 W and maintained for 5 minutes.

The BDD surface was oxygen terminated to fill vacancies, reduce surface graphitisation and produce a more homogenous surface structure before growth was continued.

3 Characterisation techniques

3.1 Scanning Electron Microscopy (SEM)

Scanning Electron Microscopy (SEM) is a useful technique used for imaging the surface morphology of materials with high resolution. The process begins with an electron gun, which generates a beam of electrons by heating a filament under high vacuum. These electrons are then accelerated through a positively charged anode, resulting in a high-energy electron beam. Magnetic and objective lenses are employed to focus and control the direction of the beam as it scans across the sample surface. When the electron beam interacts with the material, the electrons interact and scatter. This results in the generation of backscattered electrons, secondary electrons, and characteristic X-rays, each providing valuable information about the sample's composition and surface. Backscattered electrons are reflected backward after undergoing elastic interactions with atoms in the sample. The number of backscattered electrons detected is proportional to the atomic number (Z) of the elements present, making this signal useful for compositional contrast imaging. In contrast, secondary electrons result from inelastic interactions, where incident electrons transfer energy to atoms in the sample, causing the emission of lower-energy electrons. These secondary electrons are particularly useful for high-resolution imaging of surface features. In this project, the samples are predominantly carbon (diamond), therefore secondary electrons are more important for characterisation as the composition varies minimally.

Additionally, an X-ray detector captures characteristic X-rays emitted by elements within the sample, enabling elemental analysis through energy-dispersive X-ray spectroscopy (EDS). The final SEM image is rendered in greyscale, where brighter regions indicate areas with higher electron emission, while darker regions correspond to areas with lower electron emission.

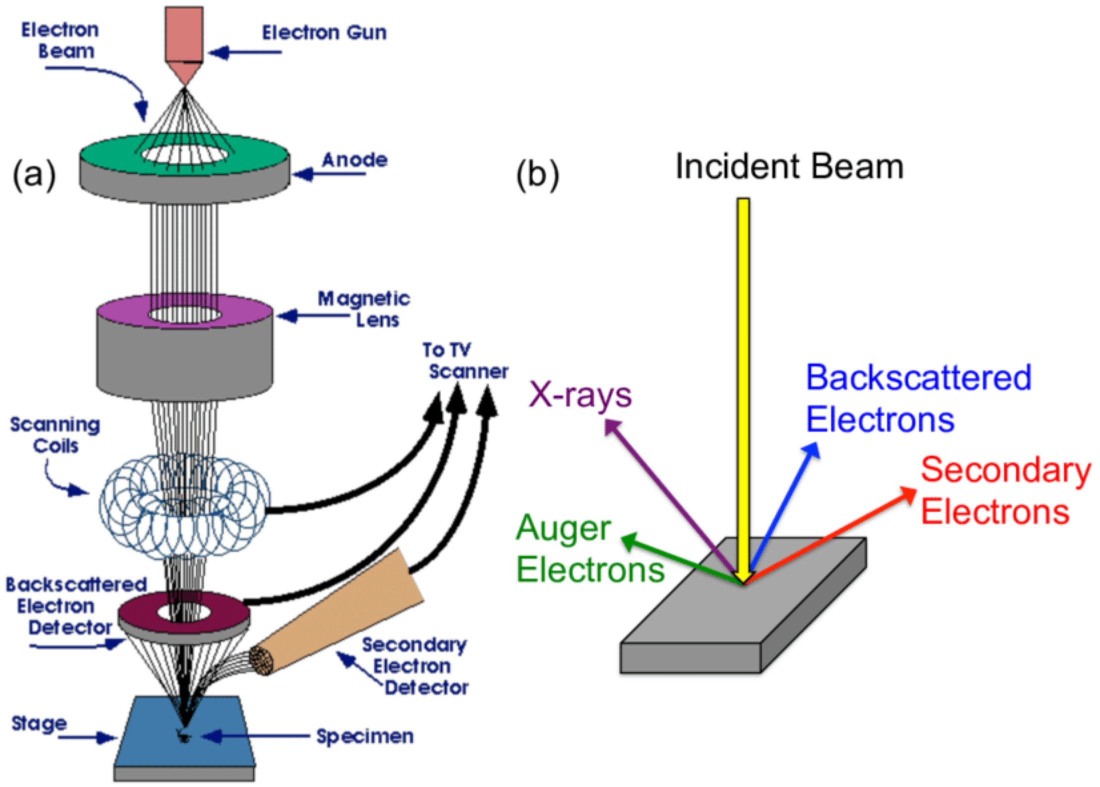

Figure 28 – [A] A schematic of a scanning electron microscope (SEM) and [B] the electron interactions of an incident beam, sourced from [91]

3.2 Energy-Dispersive X-ray Spectroscopy (EDS)

Energy dispersive X-ray spectroscopy is an analytical technique that used analysis of material. It can determine the elemental composition of a sample by the analysis of characteristic elemental X-rays. EDS measurements are completed in tandem with SEM. An EDS detector collects these X-rays, measures their energy, and produces a spectrum that corresponds to the elements present in the sample.

3.3 Laser Raman Spectroscopy

Laser Raman Spectroscopy is a technique used to analyse the vibrational modes of a molecule by studying how light interacts with a sample. It is a non-destructive method for the quantitative analysis of materials. When a monochromatic laser interacts with a sample, it can be reflected, absorbed, or scattered. Most of the scattered light undergoes Rayleigh scattering, where the scattered photons have the same wavelength as the incident light. However, a small fraction of the scattered light undergoes Raman scattering, where the photons exchange energy with the molecular vibrations, leading to a shift in wavelength.

In this project, the laser Raman spectrometer employs an Ar+ (Argon) laser with a wavelength of 514 nm (visible green light) as an excitation source, also using a confocal micro-Raman system (Renishaw RM 2000). The resulting Raman shift is measured in wavenumbers (cm^{-1}), which represents the spatial frequency of the vibrational modes. Raman shift is used to study molecular bonds and crystal structures. In diamond, which consists of sp^3 hybridised carbon bonds, Raman scattering produces a characteristic peak at 1332 cm^{-1}, corresponding to the vibrational mode of the crystal lattice as shown in Figure 29.

For the measurements of the samples a low laser power was used, to reduce the risk of sample damage.

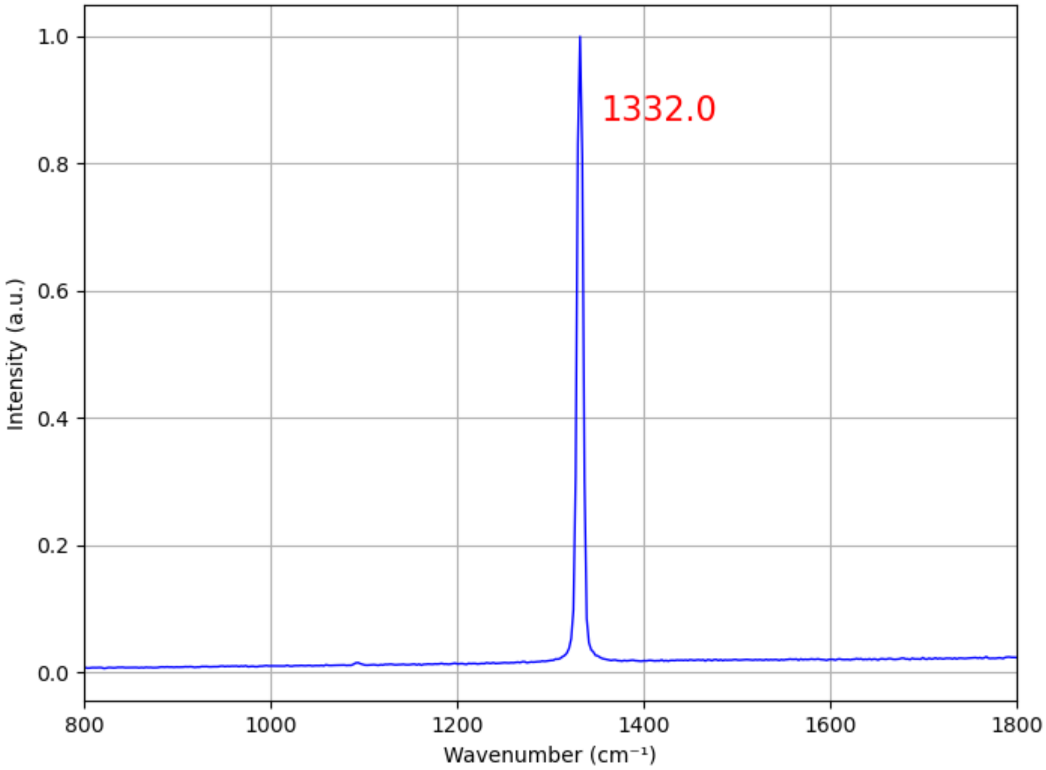

Figure 29 - Raman Spectrum (excitation wavelength 514 nm) for a Single Crystal Diamond calibration sample, the key characteristic peak of sp^3 hybridised carbon is labelled.

3.4 Olympus LEXT Confocal

The Olympus LEXT OLS5100 is a high-precision 405 nm laser scanning confocal optical microscope designed for advanced materials analysis. It enables surface imaging with up to 100× magnification, offering detailed 3D depth profiling and surface profile characterisation with sub-micron accuracy. In the context of this study, this system provides non-destructive imaging with no sample preparation required, making it ideal for rapid and precise analysis of new diamond growth.

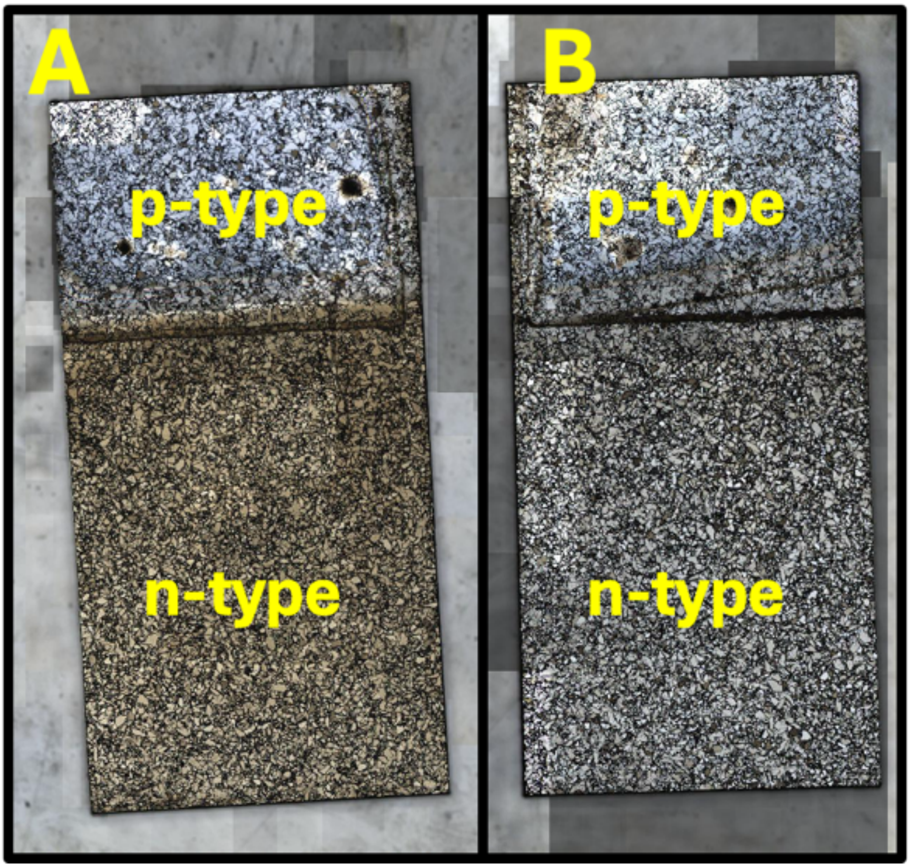

Figure 30 - LEXT map images of [A] Diode 1 and [B] Diode 2 before metallisation. The yellow-brownish colour of the n-type layer in [A] due to the high nitrogen concentration within the diamond bulk. There is also a blueish hue of the p-type layer due to high boron dopant concentration.

3.5 4-point-probe (4PP)

Electrical resistance is the opposition to the flow of current in a material and is experimentally determined by measuring a drop in voltage between two electrodes. A four-point probe is employed to measure resistivity, mitigating the impact of contact resistance by using separate pairs of electrodes for current sourcing and voltage measurement. The outer probes apply a known current, while the inner probes measure the resulting voltage drop. This eliminates internal resistance of a traditional two-point probe and ensures accurate resistivity measurements.

$$\rho = \frac{\pi t}{ln(2)} \frac{V}{I} f_1 f_2 \tag{3.1}$$

Where ρ is the resistivity expressed in Ω m, t is sample thickness (m), V is the potential difference (V) and I is the current through the sample (A). f_1 and f_2 are the geometrical factors that account for the finite dimensions of the sample. Geometrical factors f_1 and f_2 account for the finite dimensions of the sample, where $f_1 = 1$ when the separation between contacts is much greater than the thickness of the sample and $f_2 = 1$ when the sample length and width are significantly larger than the spacing between contacts. Otherwise, correction factors must be applied. The measurements were performed using a Keithley 2400 SMU, which had a precision of 0.012% basic accuracy and a 5 ½ digit resolution. The data was collected using an I-V characterisation program on LabView.

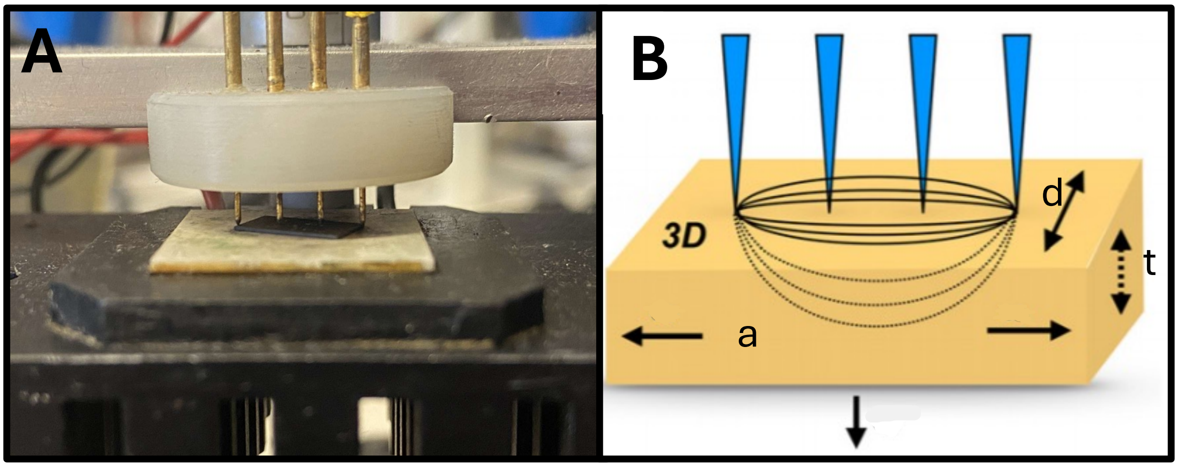

Figure 31 - [A] A photograph of a BDD sample placed in the 4-point-probe apparatus. [B] A schematic of the current flow in a semi-infinite 3D material [*92*].

3.6 Hall Voltage Measurement

The resistivity calculated using a 4-point-probe is a combination of the mobility and the carrier concentration. Hall measurements allow you to calculate each parameter directly. Hall measurements rely on the hall effect; underlying this is the Lorentz force.

When an electric current (I) flows through a semiconducting material in the presence of a magnetic field (B), the charge carriers experience a force which acts normal to both directions:

$$F = q(E + v \times B) \tag{3.2}$$

Where q is the charge of a carrier (typically the elementary charge, 1.602×10^{-19} C), E is the electric field and v is the drift velocity of the charge carriers. This force causes charges to accumulate at one side of the material, which gives rise to an electric field known as the Hall field (E_H). This results in a measurable Hall voltage (V_H). For a p-type material, $V_H$is positive and for an n-type material, $V_H$is negative.

$$V_H = \frac{IB}{qnd} \tag{3.3}$$

Where d is the sample thickness, and n is the charge carrier concentration. If n is known, the carrier mobility (μ) can be determined using the resistivity (ρ):

$$\mu = \frac{\sigma}{qn} = \frac{1}{qn\rho} \tag{3.4}$$

where $\sigma$is the electrical conductivity [93].

Hall measurements were attempted employing the Van der Pauw technique [94], applying the contacts to the vertices of the sample to measure hall voltage and resistivity. However, these measurements were unsuccessful, due to the poor adhesion of the indium contacts onto the diamond surface. The lack of stable electrical contacts prevented reliable data collection and thus results from these attempts are not included in this report.

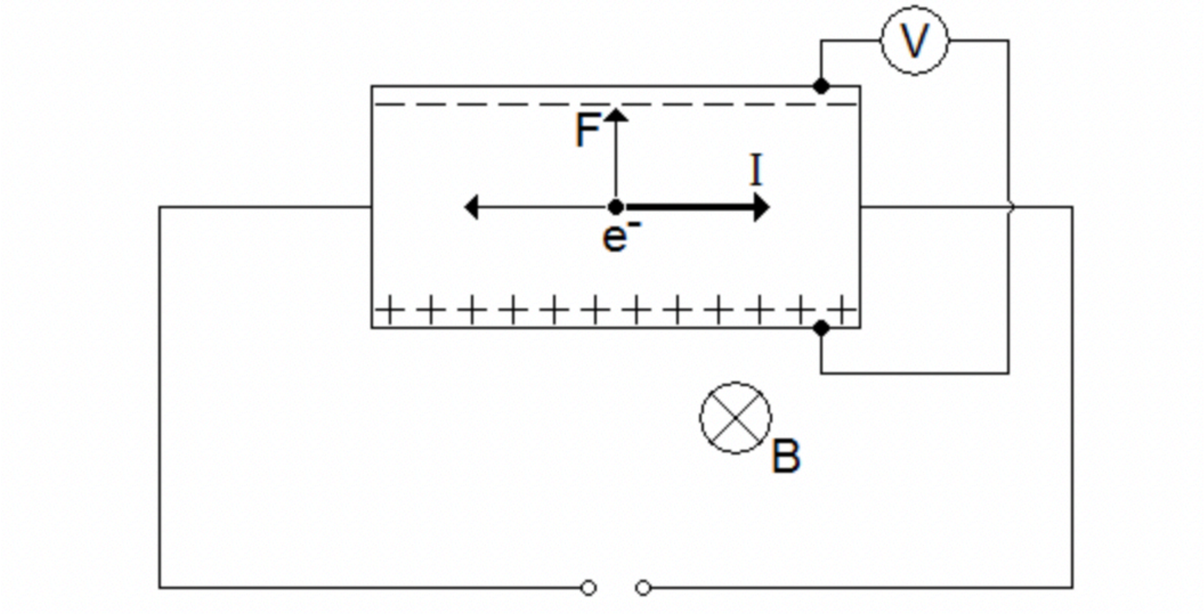

Figure 32 - A diagram of the hall effect in a 2D conducting material sourced from [94]

4 Results and Discussion

4.1 Raman Spectroscopy

Raman spectroscopy was conducted after the initial growth of the diode, before metallisation. The primary purpose was to highlight the differentiation in doping across layers. Unfortunately, due to external complications (a broken Raman laser), a spectrum for the intrinsic diamond nor the co-doped layer was not recorded.

4.1.1 N-type Diamond

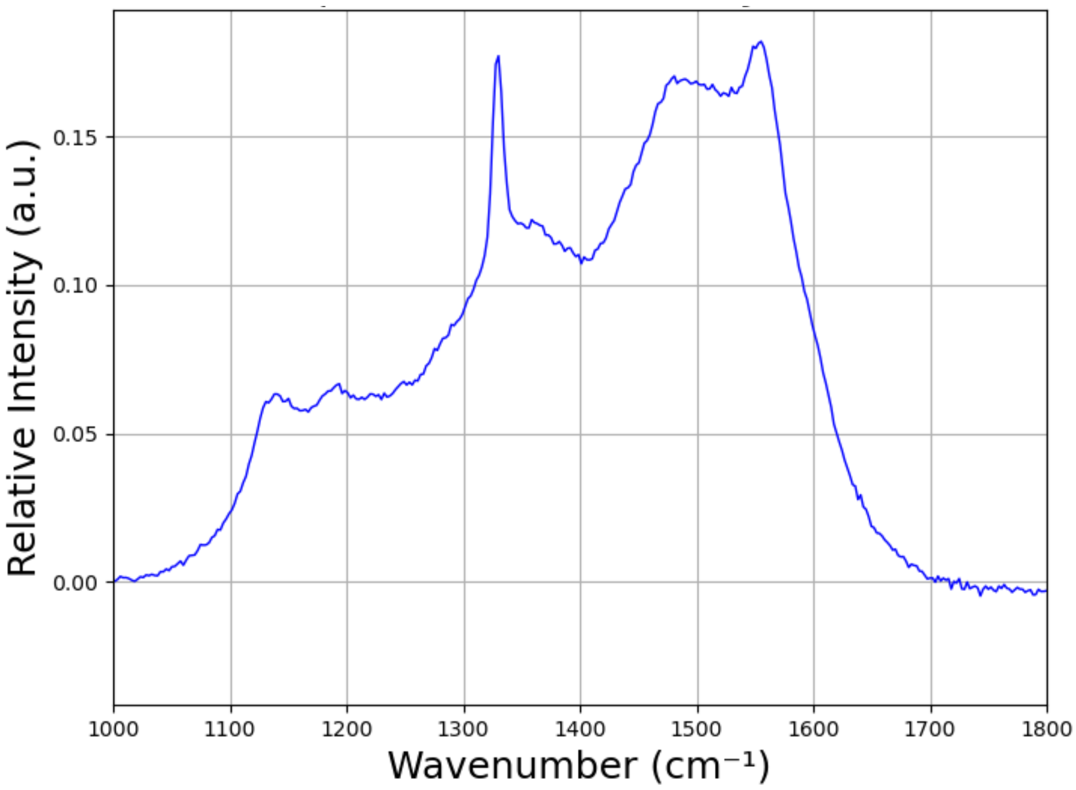

Figure 33 - Raman spectrum (excitation wavelength 514 nm) for the n-layer of Diode 1

The Raman spectrum shown in Figure 33, highlights the characteristic features typically associated with nitrogen doped diamond (NDD). The measurements identified five distinct peaks located at 1150 cm^{-1}, 1190 cm^{-}1, 1332 cm^{-1}, 1480 cm^{-1} and 1550 cm^{-1}. The prominent band at 1332 cm^{-1} is indicative of sp^{3} hybridised carbon and thus diamond. This was previously shown as a single phonon peak in Figure 29 for a single crystal diamond sample. The band which ranges from 1540-1560 cm^{-1} can be assigned to the sp^2 carbon phase, indicative of amorphous carbon content in the sample (G-band) [95]. The incorporation of nitrogen into the diamond lattice results in an increase in the sp^2 hybridised species of carbon. These defects as well as the abundance of large grain boundaries of the PCD have increased the graphitic nature of the NDD [82].

Kuntumalla et al., states that the Raman peak observed at approximately 1190 cm^{-1} in the nitrogen n-type layer, is assigned to the C=N-H bond structure within the diamond lattice [96]. Moreover, the presence of trans-polyacetylene carbon formed at grain boundaries is indicated by the additional characteristic features detected in the spectrum at 1150 cm^{-1} and 1480 cm^{-1} [97]. However, despite convincing arguments form Ferrari & Robertson supporting the theory of trans-polyacetylene carbon [98]. Prawer & Nemanich et al., discusses how this theory remains controversial, as the broad nature of the 1480 cm^{-1} is uncharacteristic of a well-defined molecular species [99]. This broadening may, however, be influenced by the superposition of graphitic species, which are accounted for in the 1540-1560 cm^{-1} G-band.

4.1.2 P-type Diamond

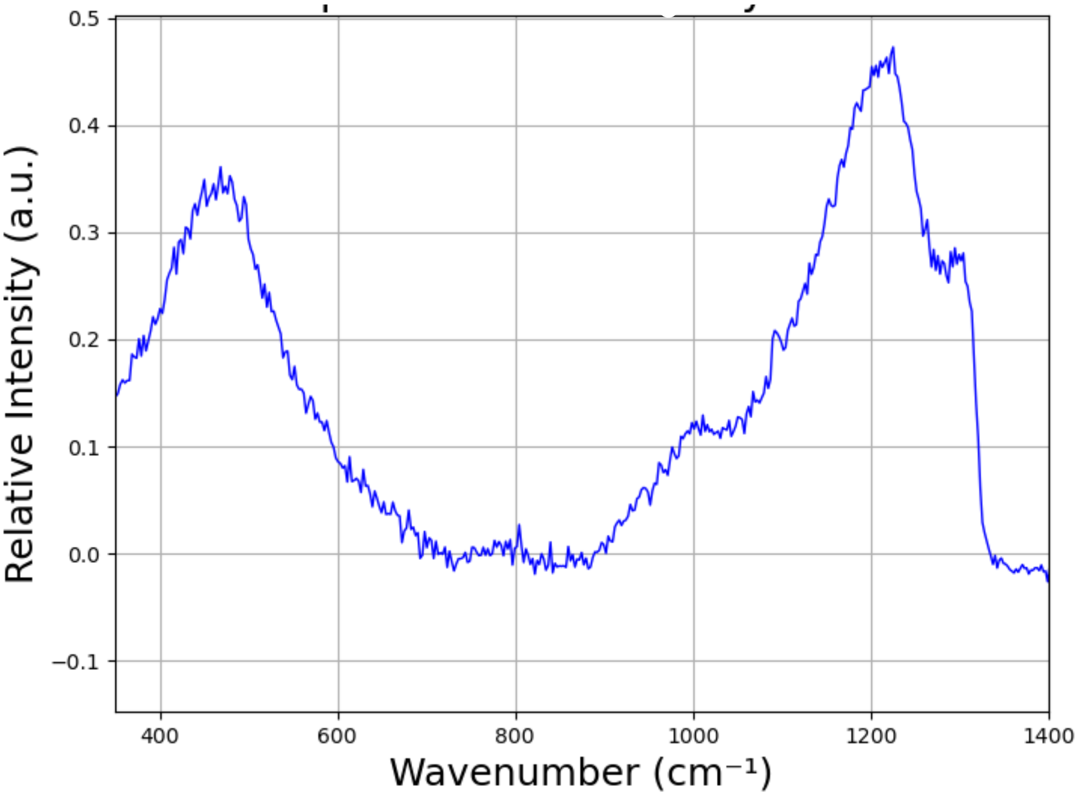

Figure 34 - Raman spectrum (excitation wavelength 514 nm) for the p-layer of Diode 1

The result of the Raman spectrum, shown in Figure 34, is somewhat reminiscent of a 'U-shaped valley', with its point of inflection centralised at 800 cm^{-1}. The measurements identified three distinct features: two broad bands around 500 cm^{-1} and 1200 cm^{-1}, as well as a narrower peak at 1300 cm^{-1}. In BDD, with increasing hole concentration, there is an increasing asymmetry of the zero-phonon line observed, attributed to Fano-type interference [99]. The Fano effect describes the asymmetric broadening and shifting of spectral peaks due to the interaction between discrete vibrational modes and a continuum of electronic states. Due to the high boron concentration in the p-layer of diode 1, the 1332 cm^{-1} characteristic diamond single phonon peak of the sp^3 hybridised carbon has been red-shifted and the wavenumber decreased to approximately 1300 cm^{-1}.

The broad bands at 500 cm^{-1} and 1200 cm^{-1}, can also be attributed to the Fano effect as their positions approximately align with two maxima in the phonon density of states (PDOS) [100]. However, May et al., continues to suggest that the origin of these peaks remains uncertain [99, 100]. There is also evidence to suggest that the peaks can be assigned to the vibrational modes of boron pairs [101, 102]. The probability of these pairs increasing with increasing boron concentration. More recently, Mortet et al., writes that these wide bands are the result of the convolution of the “dirty-metal” electronic states and Fano-shaped functions [103].

In 2004 Bernard et al., showed that the 500 cm^{-1} band could be fitted with a combination of Gaussian and Lorentzian line shapes and used to approximate boron concentration [104]. The peak of the 500 cm^{-1} band in Figure 34 is 470 cm^{-1}. It was observed that the wavenumber, ν, of the Lorentzian component of the peak obeyed the following relationship:

$$[B](\text{in } cm^{-3}) = 8.44\ \ 10^{30} e^{-0.048\nu} \tag{4.1}$$

where ν is in cm^{-1} over a range of doping from 2×10^{20} to 1×10^{22} [B] cm^{-3} [99], thus providing a non-destructive method for calculating doping levels in heavily doped BDD.
Substituting 470 cm^{-1} into Equation 4.1, gives a boron concentration of 1.34×10^{21} cm^{-3} for the p-layer in Diode 1. This value is in agreement with calibrated values carried out in the Diamond Laboratory.

4.2 Four Point-Probe

Four point-probe measurements were undertaken for the BDD, after the growth from 2.1 was completed. They were conducted in the Charl Faul laboratory in the Bristol chemistry building. The 4-point-probe was connected to a Keithley 2400 and readings recorded using LabView software. The current was increased stepwise and the voltage measured and recorded at multiple steps, an average was taken.

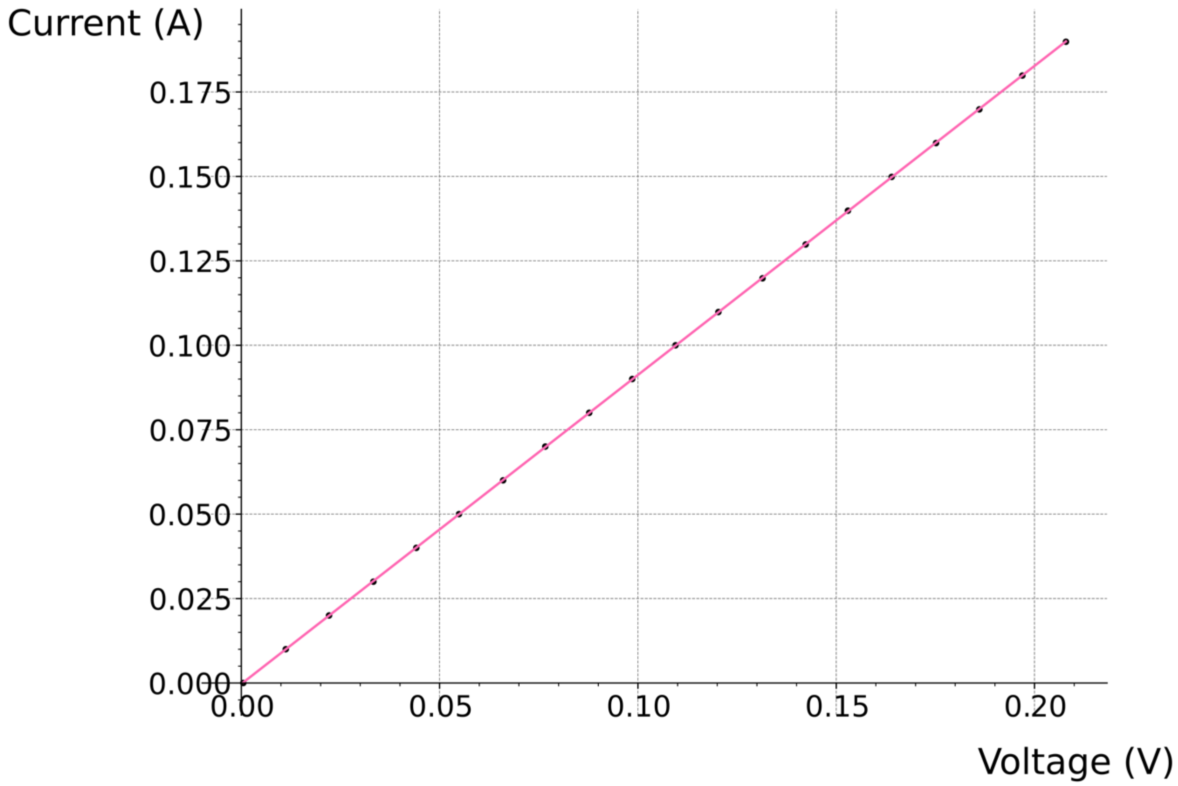

Figure 35- I-V Response of BDD under the 4-point-probe apparatus. Due to the high boron dopant concentration, the response is ohmic and demonstrates the metallic-like conductivity of the thin films.

The resistance, R, is equal to the reciprocal of the gradient of Figure 35, and has a value of 1.09 Ohms.

$$\mathrm{R} = \frac{V}{I} = \frac{1}{gradient} \tag{4.2}$$

In this project, there was large probe separation compared to the finite length and width of sample. Therefore, the assumption of the sample as an infinite plane is no longer valid. Using both Equation 3.1 and 4.2, applying a correction factor of 1.7196 [105] for the finite width correction, f_2, gave a resistivity of 2.97×10^{-3} Ohm m for the BDD sample. This value for the resistivity is in agreement with the values listed on Element Six for a boron concentration in the range of $2 - 6 \times 10^{20}$ cm^{-3} [107] and within to a similar order of magnitude of the value calculated in the previous section.

4.3 Scanning Electron Microscopy

In this project, a JSM-IT300 SEM kit from JEOL was employed for top-view imaging, to probe the surface characteristics of the PCD film. The working distance was varied from 10.3 to 10.7 mm, a high probe current that ranged from 10.6 to 30 A and the electron acceleration voltage kept constant at 15 kV for all SEM images.

Figure 36 highlights the polycrystalline nature of the surface of the diamond, with large grain boundaries and variations in the surface morphology. In PCD, these grain boundaries, point defects and dislocations acts as scattering centres that increase resistivity influencing the calculated value in the previous section. The grain boundaries increase the content of sp^2 hybridised carbon, the presence of graphitic species at these boundaries can introduce localised conductivity regions, altering resistivity. Though, Figure 36 shows that there are no large pinholes or defects on the surface of the BDD, suggesting uniform and homogenous film growth. However, small boron-rich clusters are visible across the surface, appearing as particulate ‘dust’. These clusters may again locally alter the surface conductivity, introducing further inhomogeneity in electron transport.

Additionally, the observed surface roughness, evident from the topographical variations, could impact the accuracy of the four-point probe measurements by affecting the sample-probe contact and introducing non-uniform current distribution. Although these variations are small relative to the size of the probe.

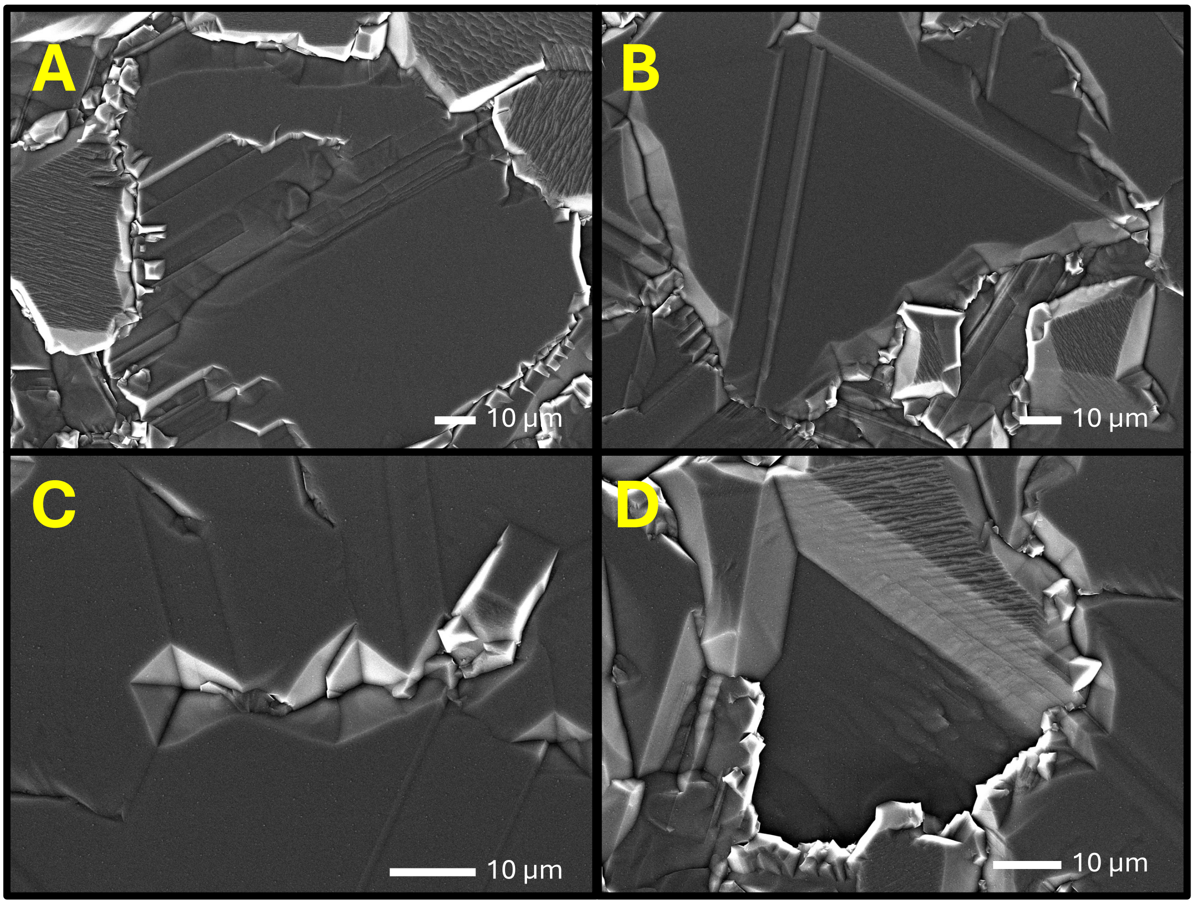

Figure 36 - Collection of SEM images of the surface of the BDD used in Diode 1 and Diode 2

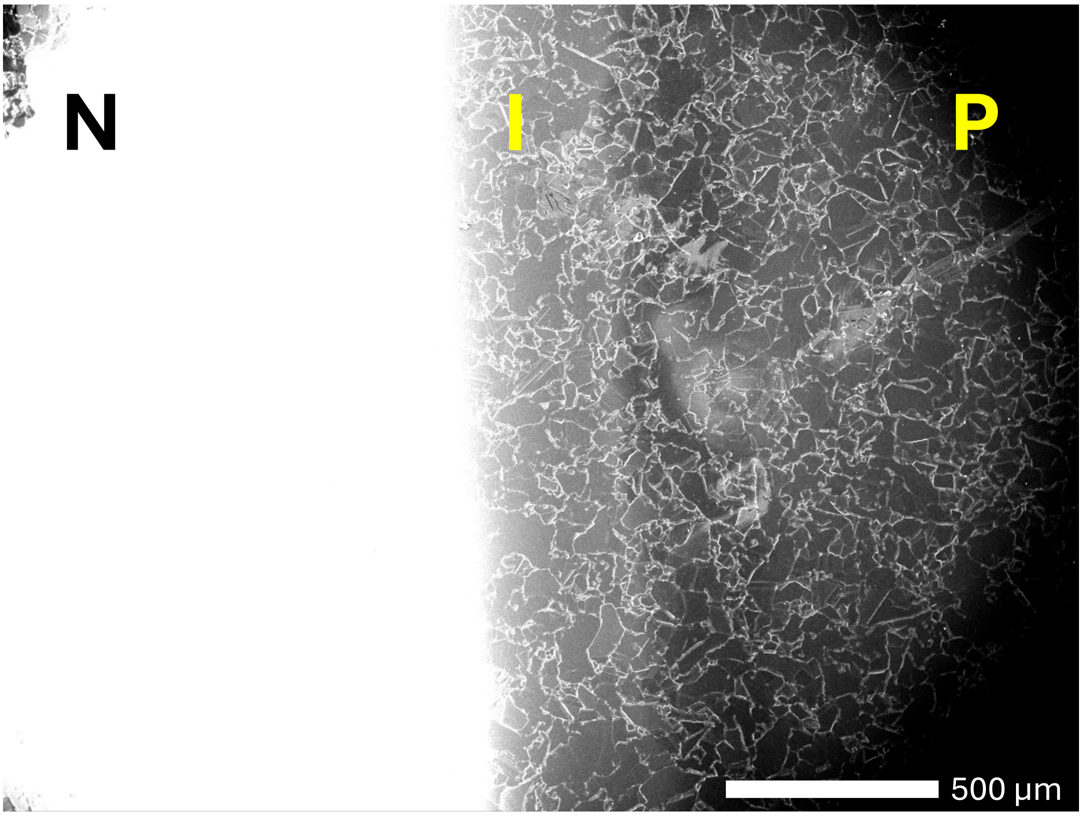

Figure 37 - An SEM image of the top-view P-i-N junction of Diode 1. Greyscale step is clearly shown.

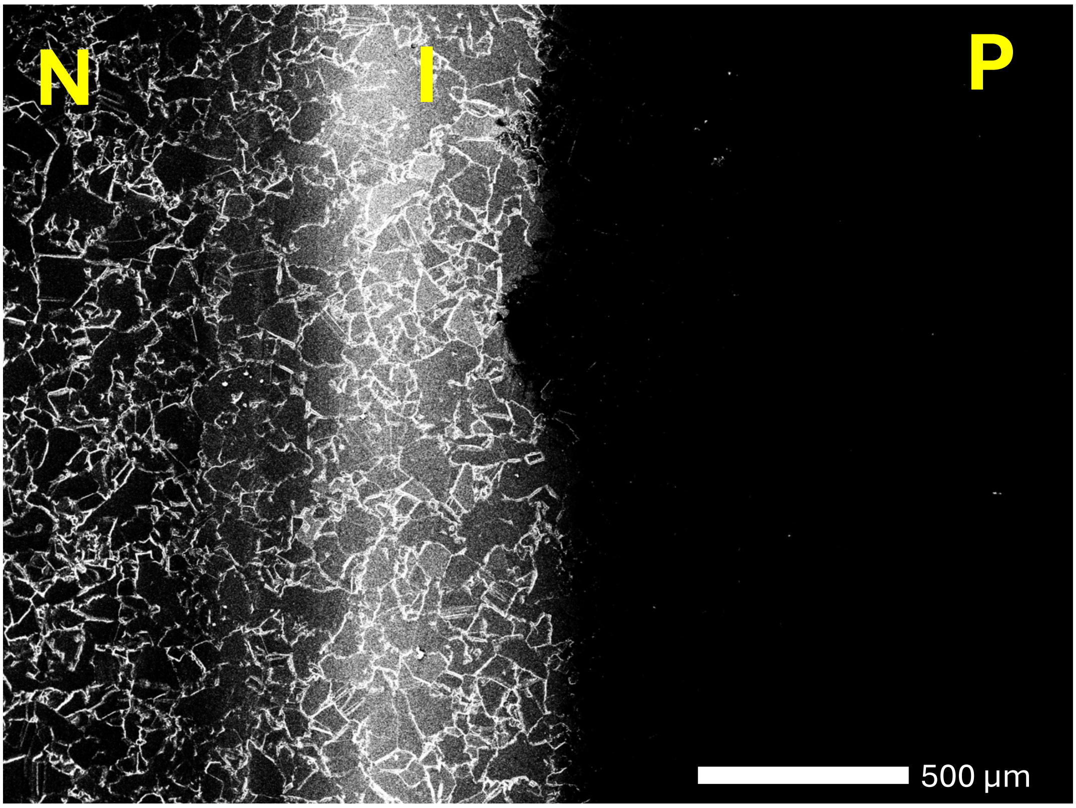

Figure 38 - An SEM image of the top-view P-i-N junction of Diode 2. The pseudo ‘N’ type region is much darker than expected.

Figure 37 is an SEM image of the P-i-N interface of Diode 1. The contrast arises from the change in emission of secondary electron (SE) yield across the surface and hence the dopant within the diamond lattice. Highly doped regions exhibit more contrast.

The work function is the defined as the difference in energy between the Fermi level, E_F, and the vacuum level, E_{vac}, and can be defined by the equation:

$$\phi = E_{vac} - E_F \tag{4.2}$$

Previously, in Figure 6, the acceptor and donor levels are presented. The fermi level, E_F, lies between these levels and the valence and conduction band, respectively. Therefore, in BDD, a p-type material, the fermi level is much further from the conduction band. The difference between E_{vac} and $E_F$is greater, leading to a larger work function. Consequently, the BDD step of the device has a lower SE yield, E_F is closer to the valence band, reducing the availability of free electrons for SE emission. Hence is darker in shade. The intrinsic layer E_F lies between directly the conduction band and valence band and is grey in colour. An intermediate between the p-type and n-type layers.

N-type materials typically have a higher SE yield because electrons are more easily excited and emitted due to the higher Fermi level being closer to the conduction band. In n-type materials there are also more free electrons near E_F which contribute to SE emission, increasing the yield. Figure 37, demonstrates the formation of a P-i-N junction through surface imaging and SE yield.

Figure 38 is an SEM image across the surface of the P-i-N of Diode 2. The gradient for the change in greyscale is similar to before. The p-type layer is very dark due to the lower SE yield detected, with a lighter intrinsic layer represented by ‘I’. The primary difference lies with the n-type layer. As previously discussed, the n-type layer of Diode 2 was co-doped with both boron and nitrogen. However, the ‘n-type’ layer appears very dark, much like the p-layer. With less contrast in image saturation suggesting a smaller band gap difference, compared with Figure 37. Indicating that this pseudo ‘n-layer’ in Diode 2 has a large boron concentration with respect to its nitrogen concentration. Instead, a less concentrated boron p- (minus) layer was formed, supporting the absence of the formation of a D-A-D complex and failure of experimental co-doping. If the D-A-D complex was successfully fabricated, then one would expect the n-type layer in Figure 38 to appear almost white in colour, with the SE yield similar or greater to that of the n-type layer in Diode 1.

The i-layer could not be seen on any other diodes fabricated as their i-layer and n-layer growth was completed in situ and was completely masked by the subsequent n-layer growth. Looking forward, it would be valuable to investigate the contrast in greyscale under an applied bias, where the built-in potential is varied and observe the manner in which the SE yield changes.

4.4 Current-Voltage (I-V) characteristics

4.4.1 Diode 1

In total, five devices were fabricated during this project, with Diode 1 demonstrating the most promising performance. It functioned as a working P-i-N junction diode, exhibiting the most ideal diode behaviour of all the devices fabricated. As demonstrated by Figure 40 , under reverse bias Diode 1 displayed virtually no leakage current, an early indication to excellent rectification characteristics. Under forward bias, the I-V response showed a sharp increase in current following a threshold voltage of approximately 5.5 V. While not perfectly exponential, this sharp rise reflects efficient junction activity and minimal internal resistance. The device achieved a maximum current of 1.80 × 10^{-5} A at 12 V.

Using Equation 1.2, and the estimated concentrations of the n- and p layers as shown in 2.0.1 Diode Structure I: an acceptor concentration, N_a, of 1 × 10^{22} cm^{-3}, a donor atom concentration, N_D, of 1 × 10^{17} cm^{-3} and an intrinsic carrier concentration, n_i , of 1 × 10^{27} cm^{-3} across the depletion zone [106]. This calculation returns a built-in voltage of 5.41 V. The observed threshold voltage of 5.5 V is close to the theoretical built-in potential. This suggests that the metal contacts were of good quality, with minimal voltage drop outside the depletion region. The result is a diode with efficient charge transport and a sharp turn-on characteristic, behaviour consistent with an ideal diode. Such performance suggests that Diode 1 could be highly effective in betavoltaic applications, where efficient charge collection is critical. Moreover, the high threshold voltage offers potential advantages in high-power, high-temperature and high frequency device applications, such as high-electron-mobility transistors (HEMTs) and metal-oxide-semiconductor-field-effect transistors (MOSFETs) [108, 109].

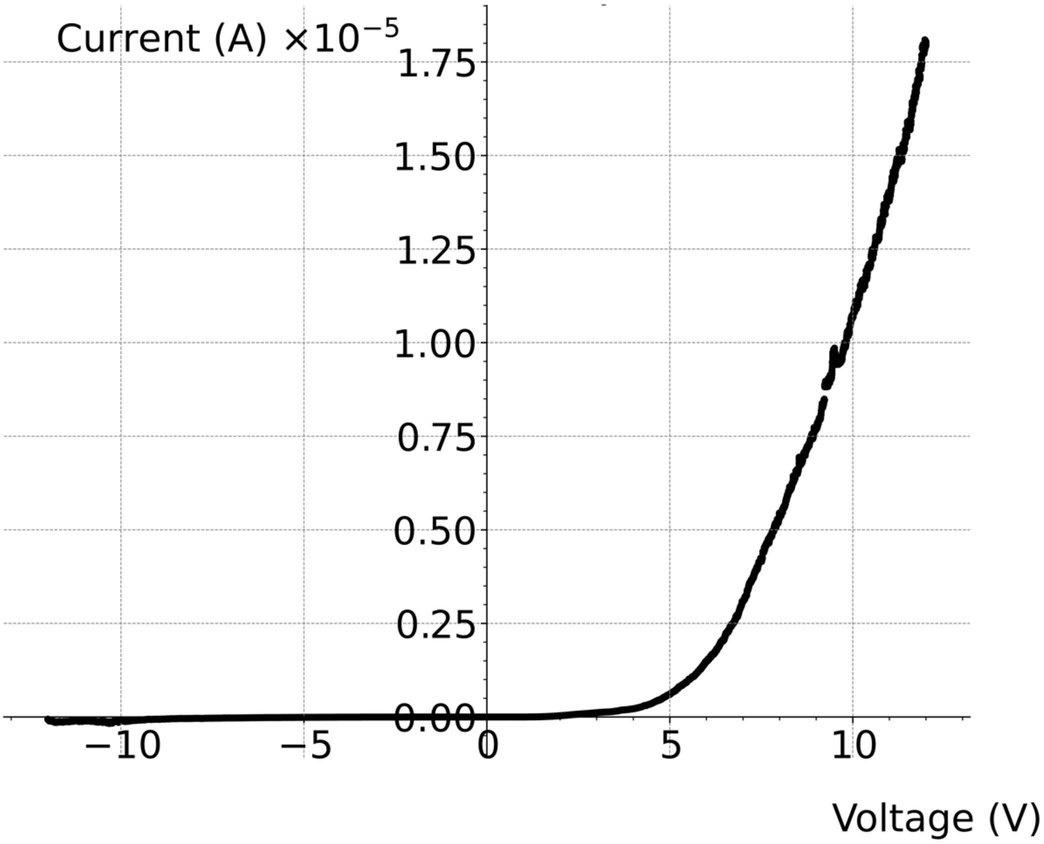

Figure 40 - Initial Diode 1 I-V response, the potential difference ranging from -12 to 12 V

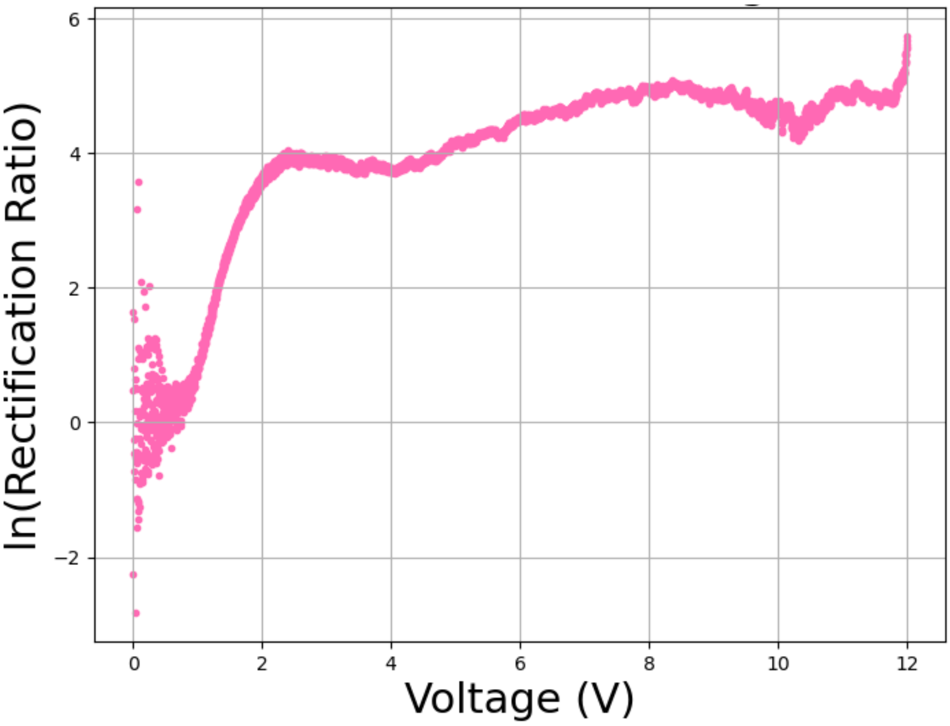

Figure 39 - The natural logarithm of the rectification ratio at a given potential difference for Diode 1.

Figure 39 shows the natural logarithm of the rectification ratio. At a bias of 12 V this value reaches 5.74, corresponding to the current density being approximately 311 times greater in the forward direction compared to the reverse. However, given that the potential difference was flat in the reverse direction, if the increase in current in the forward direction was exponential, taking the natural logarithm as in Figure 39 would produce a linear fit of $y = x$. Therefore, although having decent rectifying properties, the fabricated diode does not fit the Shockley diode equation.

Following the initial characterisation, the metal contacts were damaged and had to be reapplied. The I-V characteristic was then measured again as shown by Figure 41. There are three distinct changes. Firstly, the voltage range was extended from -20 to 20 V. Second, the peak current through the system increased by an order of magnitude, reaching 6.00×10^{-4} A at 20 V, which may reflect improved contact quality. Third, under reverse bias, a leakage current began to appear.

Hu notes that there is nothing inherently destructive about this junction breakdown [26].

In heavily doped samples, Zener breakdown occurs due to large magnitude of electric field over a physically thin depletion region. Under reverse bias, the strong electric field applies a force onto electrons, causing the electrons to tunnel from the valence band to the conduction band. In contrast, Avalanche breakdown occurs in lightly doped junctions, where the depletion region is wider [27]. A phenomenon known as impact ionisation occurs; electrons transversing through the depletion zone gain enough kinetic energy due to the applied internal electric field, moving from the valence band to the conduction band. Another electron-hole pair is created. Thus, further increasing the electric field and creating a snowball effect, hence avalanche [25, 27]. In Diode 1, although the device is heavily doped, the depletion zone is thick at 0.5 μm (the width of the intrinsic layer) which would suggest that both Avalanche and Zener contribute to the breakdown voltage and therefore an increase in current in the reverse direction. If the potential difference were to be applied beyond 20 V under reverse bias, one would expect a sharp negative gradient. With a magnitude comparable to the expected gradient under forward bias. However, this breakdown voltage is not necessarily a negative of the device. If controlled there are many applications in which this is useful.

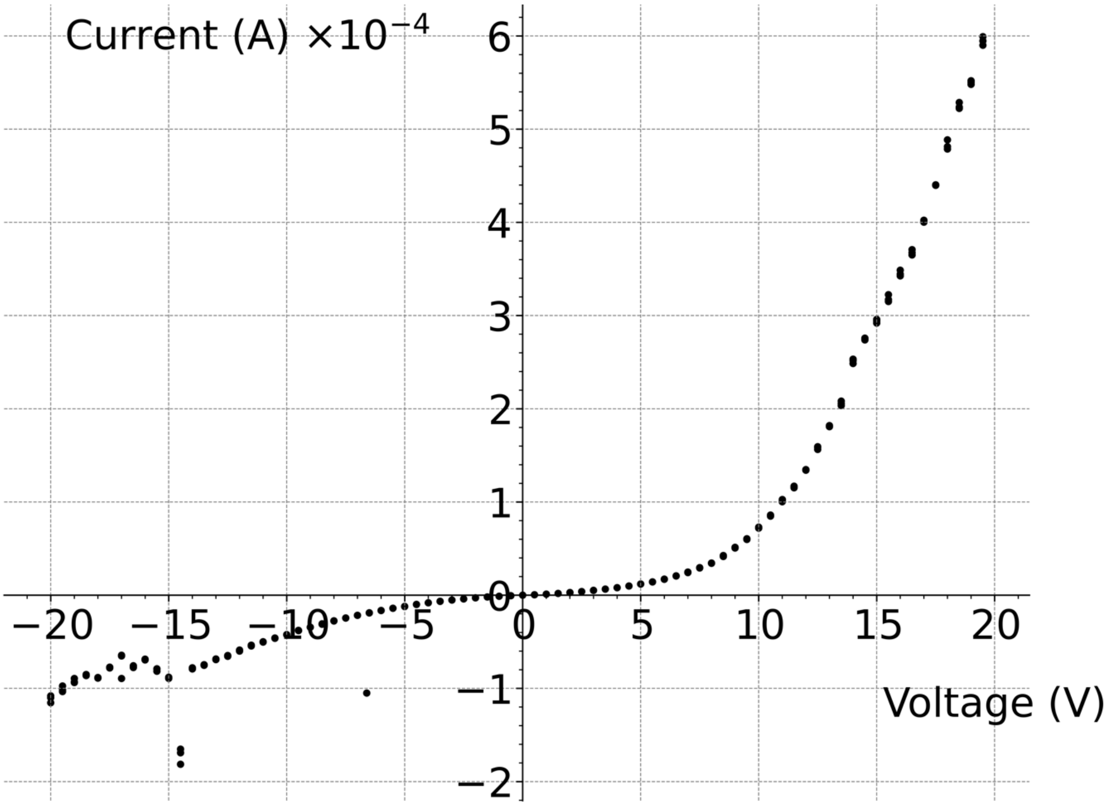

Figure 41 - Diode 1 I-V response with reapplied ohmic contacts, measured from -20 V to 20 V.

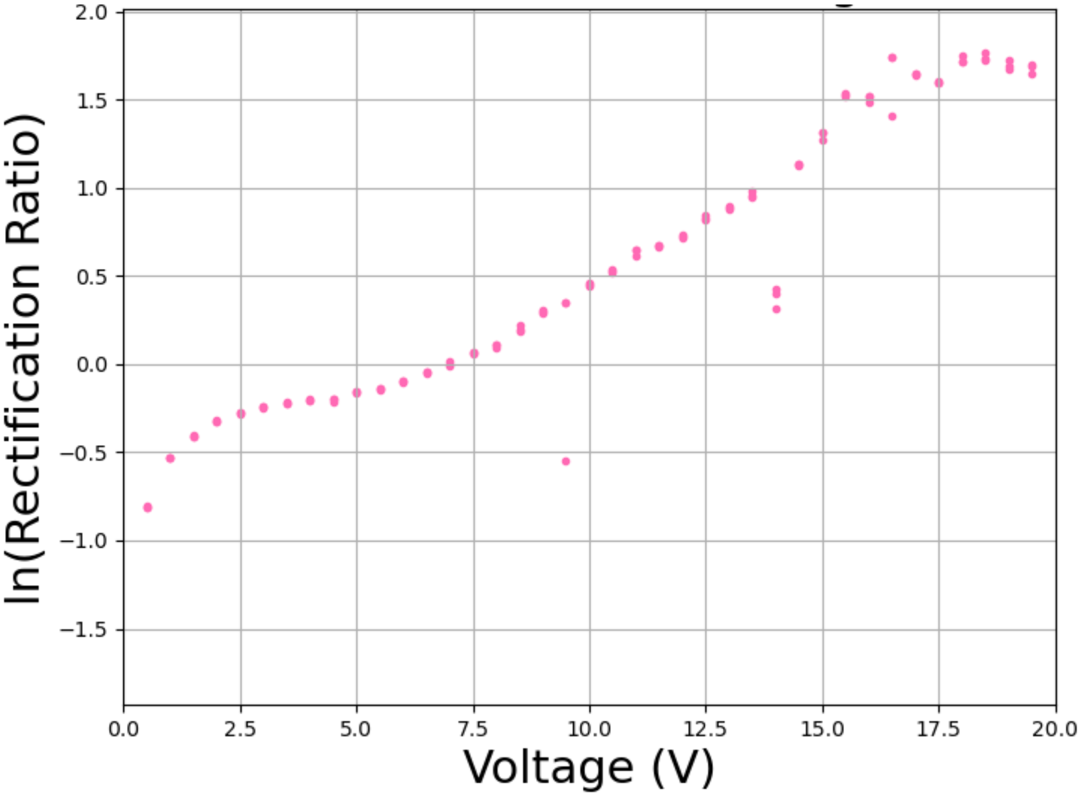

Figure 42 - The natural logarithm of the rectification ratio at a given potential difference for Diode 1 after the ohmic contacts were reapplied

4.4.2 Diode 2

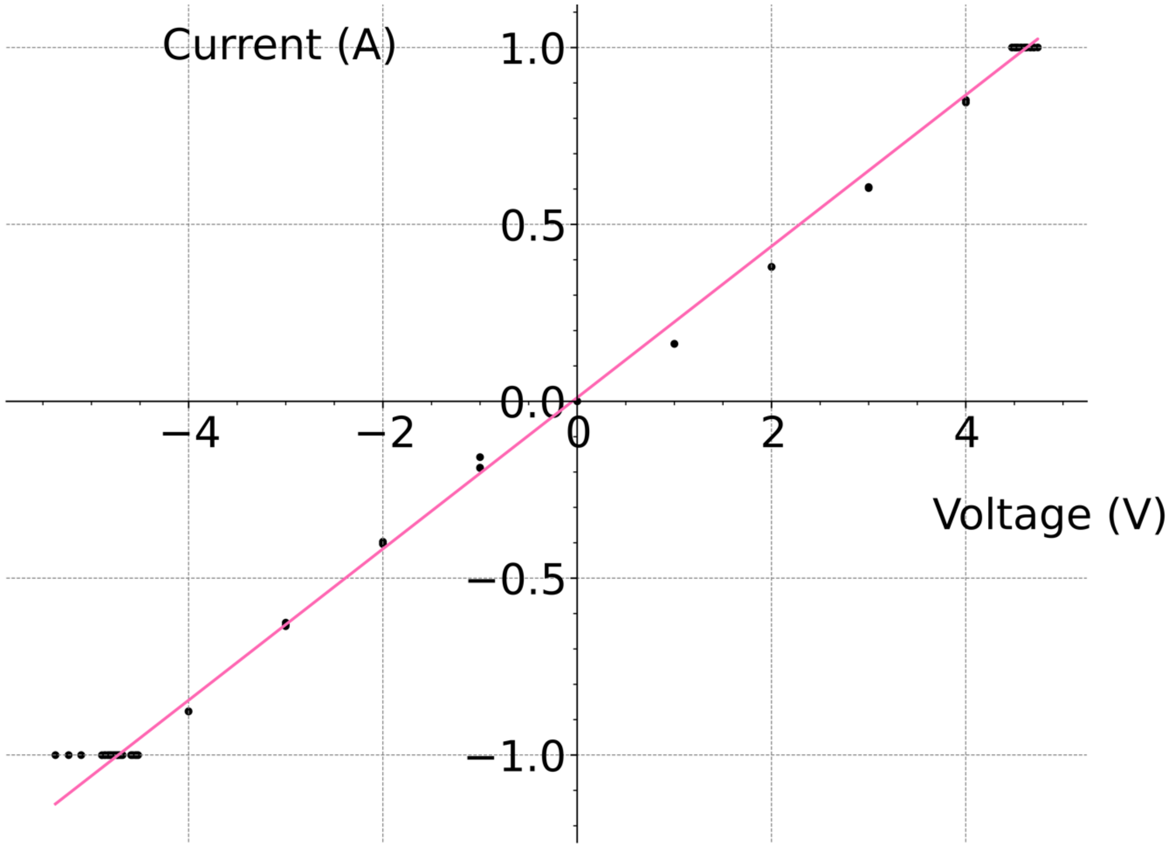

Figure 43 - Diode 2 I-V response with a linear best-fit line calculated.

Figure 43 shows the ohmic response of Diode 2, the flatlining at the extremities highlights where the device reached a compliance of 1.05 A for the Keithley 2401 at a -4 V and -4 V. Using Equation 4.2, the gradient of the linear best-fit gave a calculated resistance of 4 Ohms. The device showed no rectifying properties.

Diode 2 explored the theory of co-doping, a secondary aim of this project. The reactor conditions followed on from previous work in the Diamond Laboratory by B. Nutbrown [84]. However, the metallic response of Diode 2 as shown by Figure 43, suggests that the formation of an n-type co-doped layer was unsuccessful. This theory is emphasised by the SEM data in the previous section. Instead, a P+iP- structure was fabricated, with a high varied boron concentration throughout the device and a low concentration of nitrogen in the n-type layer. Upon reflection the nitrogen flow rate of 1.1 sccm was insufficient. A higher flow rate would have been necessary to increase the overall nitrogen concentration and therefore donor incorporation within the layer.

Furthermore, the contamination within the CVD reactor should have been further investigated before any growth conducted. Understanding the amount of boron within the reactor and therefore the ratio of boron-to-nitrogen is critical for the formation of D-A-D complexes.

In the future, the implementation of plasma diagnostics will be important for the success of experimental co-doping. Techniques such as optical emission spectroscopy can be used to measure the gas phase concentrations of activated species within the plasma and near the substrate surface [110]. Additionally, spatially resolved in situ spectroscopic measurements can be utilised to show the distributions of activated species and accurately measure substrate temperatures [111]. Further increasing the understanding of the growth conditions and environment.

Experimental co-doping was not further explored, partially due to being a secondary aim and due to the decommissioning of the back reactor, which limited experiments that required boron doping.

4.4.3 Diode 3

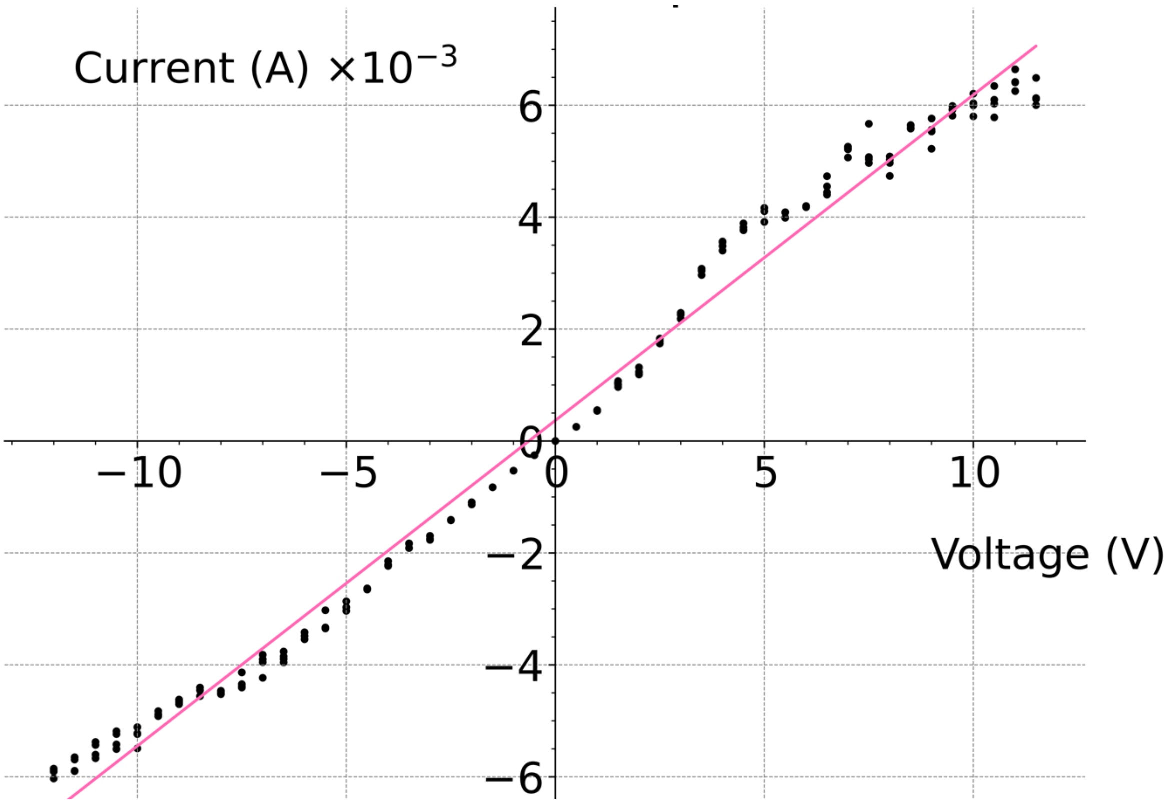

Figure 44- Diode 3 I-V response with a linear line of best-fit calculated

The resultant I-V response for Diode 3 was similar to Diode 2 with a metallic response, but with a higher resistance of 1.72 × 10^3 Ohms. Diode 3 was grown on free-standing Element Six boron doped PCD and was the only diode that did not have a laboratory grown BDD p-type layer. Initially the exceedingly high resistance and ohmic nature of Figure 44 was believed to be due to poor contact adhesion of the silver DAG onto the diamond surface. However, after further investigation, the Raman measurements of the industrially grown BDD revealed a lower concentration of boron than expected in the topside as shown by Figure 45. It also revealed that the backside of the substrate showed little to no evidence of doping as shown by Figure 46. This suggests that the bulk (substrate) of the device, rather than the p-i-n junction, dominated the flow of current which led to an observed ohmic response with high resistance.

Raman spectra of the boron doped PCD substrate of Diode 3 indicated the presence of intrinsic diamond at the backside and less heavily doped, more graphitic carbon on the surface. As previously discussed, the 1550 cm^{-1} band is evidence of amorphous, sp^2 hybridised carbon (the G-band) [95]. The characteristic 1332 cm^{-1} band of diamond is prominent within Figure 45, and not obscured nor red shifted by the broad 1200 cm^{-1} band formed in heavily boron doped samples. Moreover, the broad band at 500 cm^{-1} has a low relative intensity, and there is no 'U-shaped Valley' shape as shown previously in Figure 34. This supports the conclusion that the boron concentration is below 1×10^{20} cm^{-3} [99], implying non-metallic characteristics of the p-type layer. Furthermore, in Figure 46 only the characteristic 1332 cm^{-1} single phonon peak of sp^3 hybridised carbon in diamond is present, suggesting the base of the substrate is intrinsic diamond.

Taken together, these observations provide justifications for a higher resistivity of the BDD substrate, leading to a higher resistance response which dominated the p-i-n junction and hindered its function. Ultimately limiting the performance of the device. Confirmation of this resistivity prediction could be achieved through the application of four-point probe and Hall measurements of the substrate material.

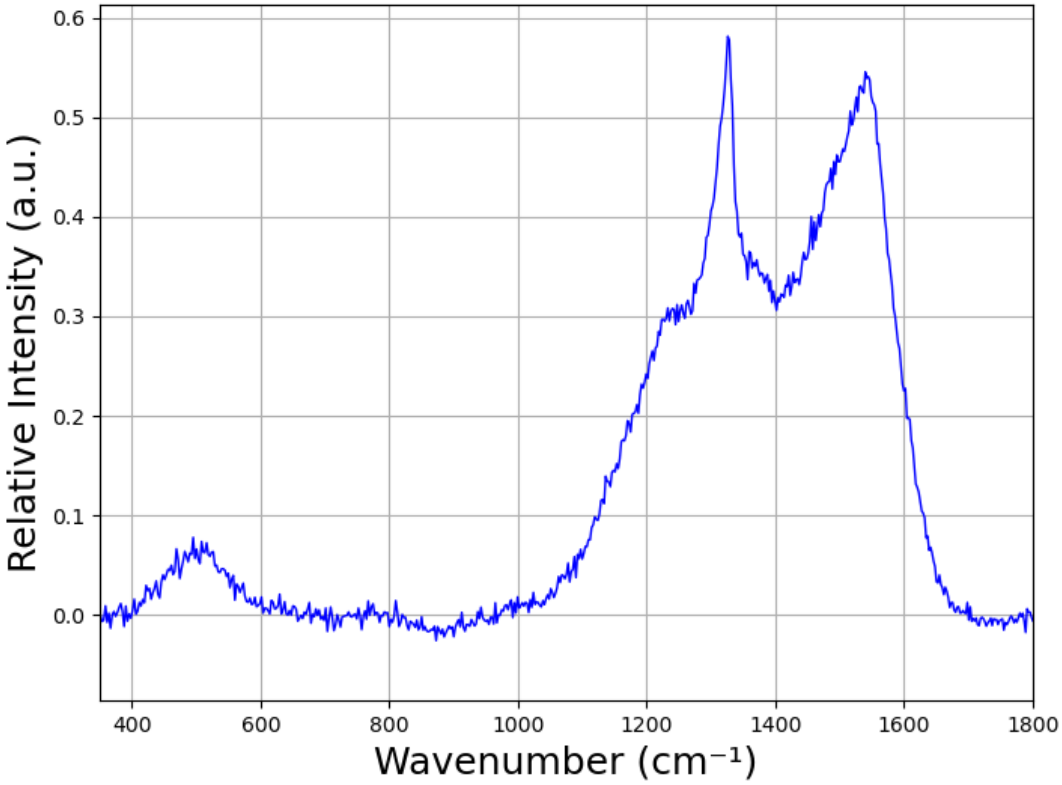

Figure 45 - Raman spectrum (excitation wavelength 514 nm) for the topside of the Element Six BDD used as a growth substrate for Diode 3.

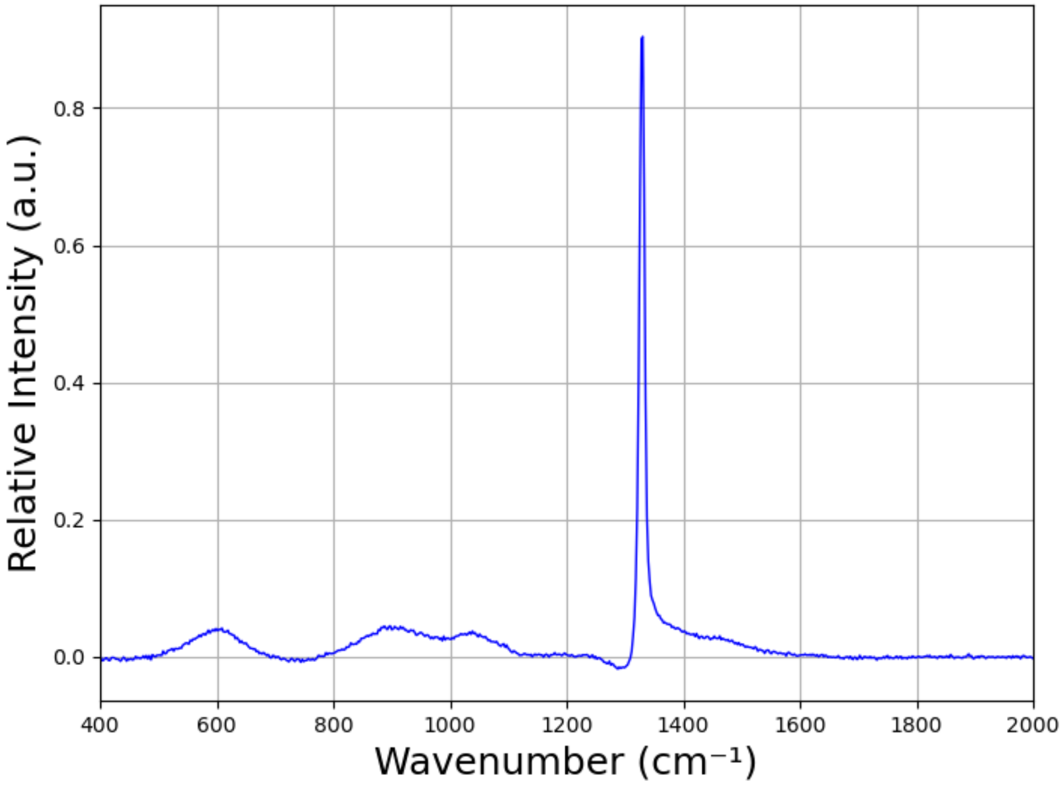

Figure 46 - Raman spectrum (excitation wavelength 514 nm) for the backside of the Element Six BDD.

4.4.4 Diode 4

Diode 4 was created to be an exact replica of Diode 1. The only difference was that Diode 4 was fabricated with its n-type layer grown *in situ* compared to the *ex-situ* n-type layer growth of Diode 1. The overall response of the I-V plot in Figure 47 demonstrates a characteristic diode shape and is comparable to the initial Diode 1 measurements as shown in Figure 49. Therefore, an early conclusion could be made that Diode 4 proved the results and *modus operandi* of Diode 1 could be replicated. Reinforcing the validity and reproducibility of the pseudo vertical P-i-N junction diode structure.

Under forward bias, Diode 4 exhibits a slight knee in the I-V curve at approximately 7 V. Above this voltage, there is a steep increase in current through the device, albeit not exponential. At 20 V, a maximum current of 8.34×10^{-5} A was recorded. The maximum rectification ratio was also recorded at 20 V, with a value of 9.11. However, at this point under reverse bias the diode begins to break down and a sudden decrease in reverse current is observed. Therefore, taking the rectification ratio at 20 V may not be an accurate representation of the full electrical response and rectifying behaviour of the diode. Additionally, the logarithmic plot of the rectification ratio as shown in Figure 48 was poor. Highlighting a non-linear trend which was again inconsistent with Shockley-type diode behaviour. Figure 49 is the comparison of the initial Diode 1 measurements against Diode 4. Diode 1 was superior in the reverse direction but in the forward direction, Diode 4 outperformed Diode 1 until 12 V. As these two devices were identical, the discrepancy in I-V response can be attributed to the wiring and ohmic contacts. This figure also revealed a threshold voltage for Diode 4 appears anonymously low at approximately 2 V compared to the value of 5.5 V compared with Diode 1 and the calculated built-in voltage of 5.4 V.

Figure 50 shows the two diodes being compared again, after the reapplication of the ohmic contacts of Diode 1, the device clearly outperforms Diode 4. In Diode 1, the application of new metal contacts led to an unexplained increase in the order of magnitude. Similar behaviour is predicted for Diode 4, although the device was not explicitly tested with new contacts.

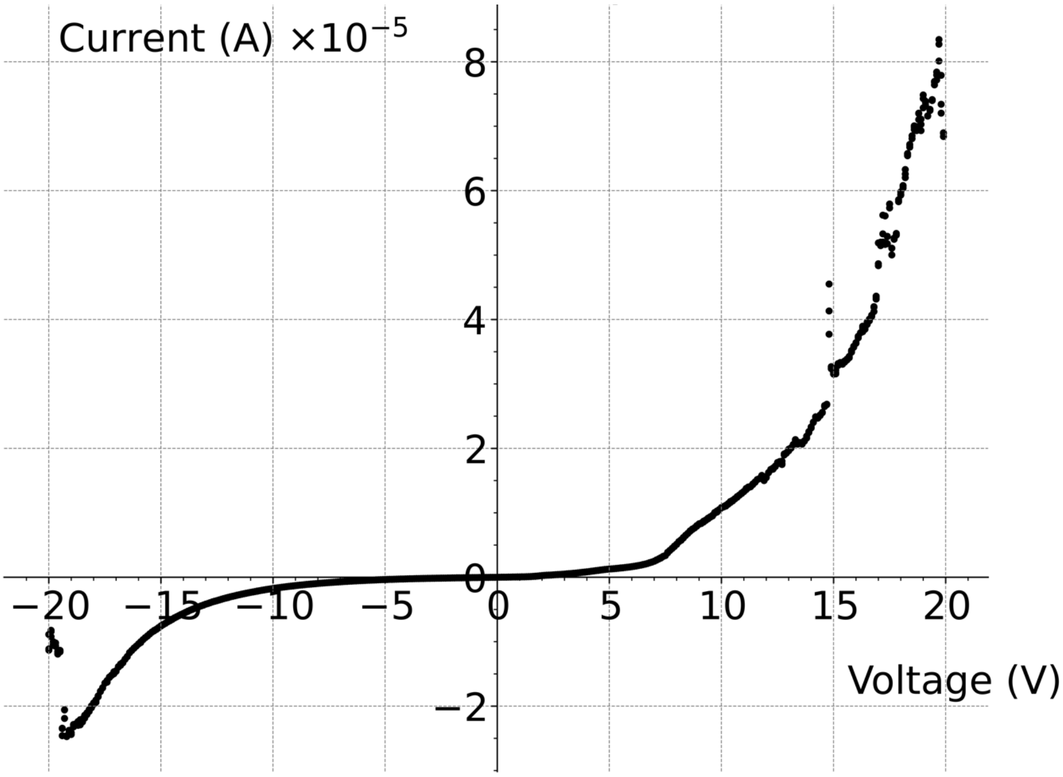

Figure 47 - Diode 4 I-V response, the potential difference ranged from -20 to 20 V.

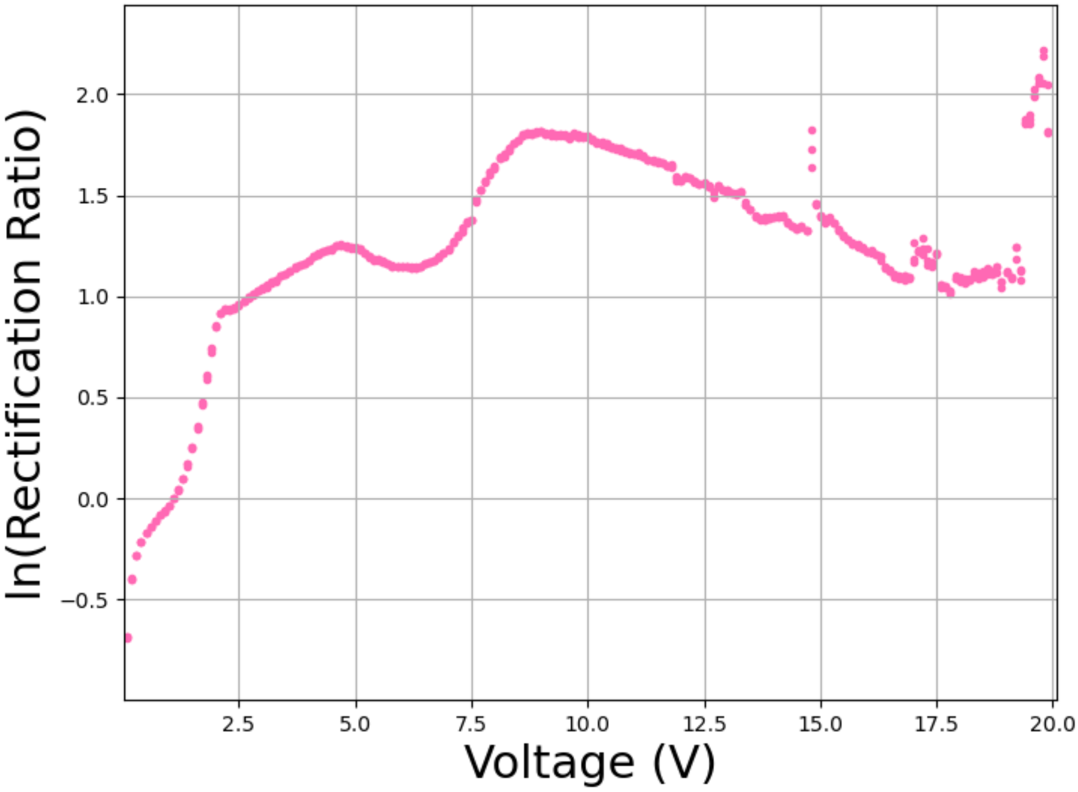

Figure 48 - The natural logarithm of the rectification ratio at a given potential difference for Diode 4.

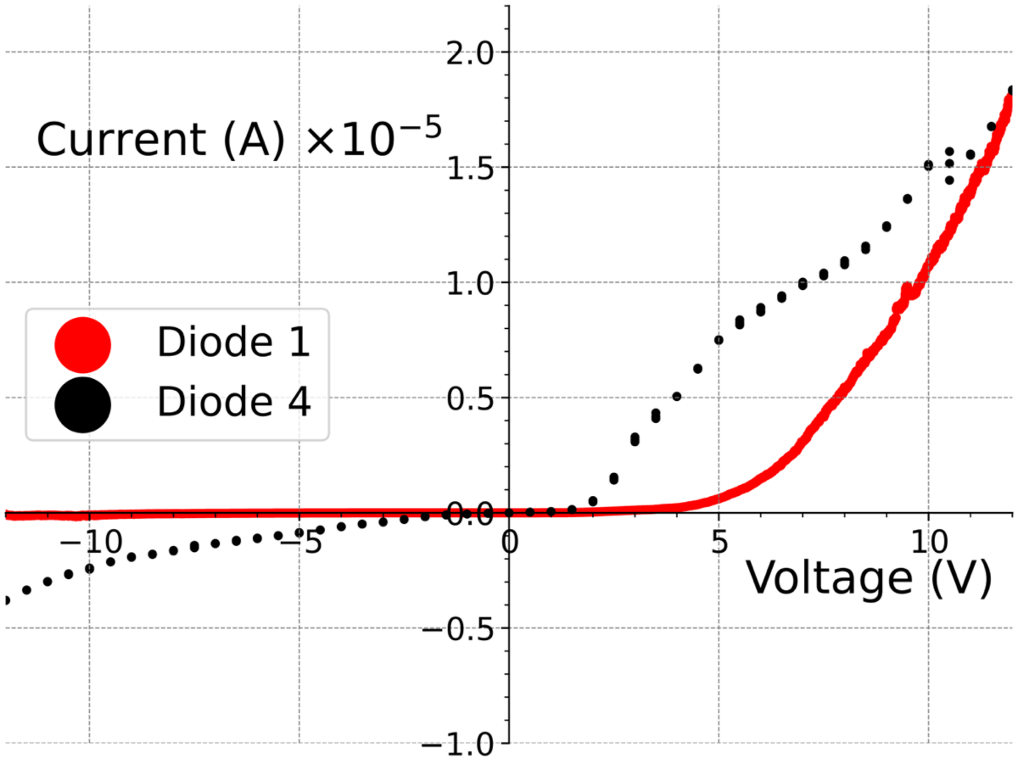

Figure 49 - I-V comparison of the initial Diode 1 measurements compared to Diode 4

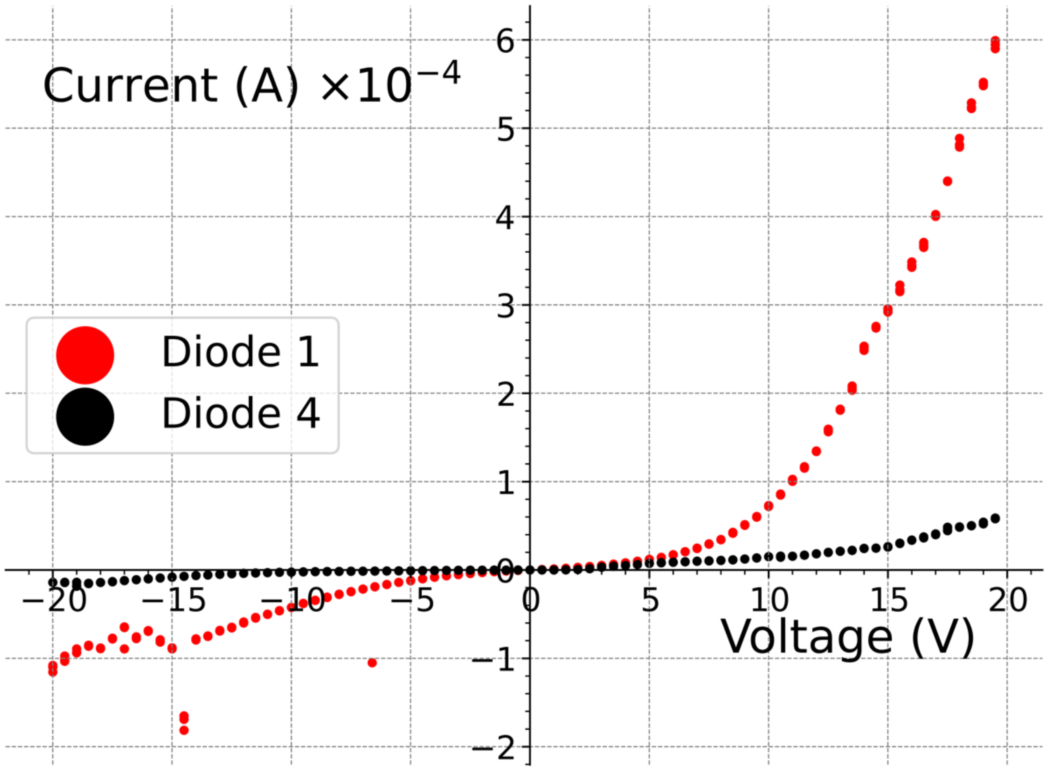

Figure 50 - I-V comparison of Diode 1 to Diode 4. Diode 4 is flat compared to Diode 1 which now measures current to order of magnitude higher

4.4.5 Diode 5

Diode 5 was designed to repeat the success of Diode 1 and 4 but with two key distinguishing modifications: an increased intrinsic layer thickness (depletion zone) and oxygen termination before subsequent diamond growth. To achieve a thicker intrinsic layer, the growth time was increase from 40 to 80 mins, effectively doubling its size. Additionally, the p-type layer underwent oxygen termination before the in situ intrinsic and n-type layer growth. This process aimed to reduce lattice vacancies and increase surface homogeneity. Despite these changes, the I-V response as shown in Figure 51 of Diode 5 was very poor and showed no diode characteristics. This was attributed to the inadequate surface contacts and the contamination of silver DAG across the device surface. As previously discussed, when not applied properly, the silver DAG had adverse effects on the movement of current through the pn junction. Due to time constraints, it was not possible to re-sputter or reapply the metal contacts. However, the shape of the I-V curve closely resembles diodes with poor or disconnected ohmic contacts as which were not included in this thesis.

The response of the I-V curve also bears resemblance to a filament lamp, suggesting that heat dissipation at higher powers increased resistance and lead to further deformation of surface contacts. To fully assess the impact of oxygen termination on sequential diamond growth as well as investigating how depletion layer thickness influences device behaviour and charge collection, further measurements with new ohmic contacts are required.

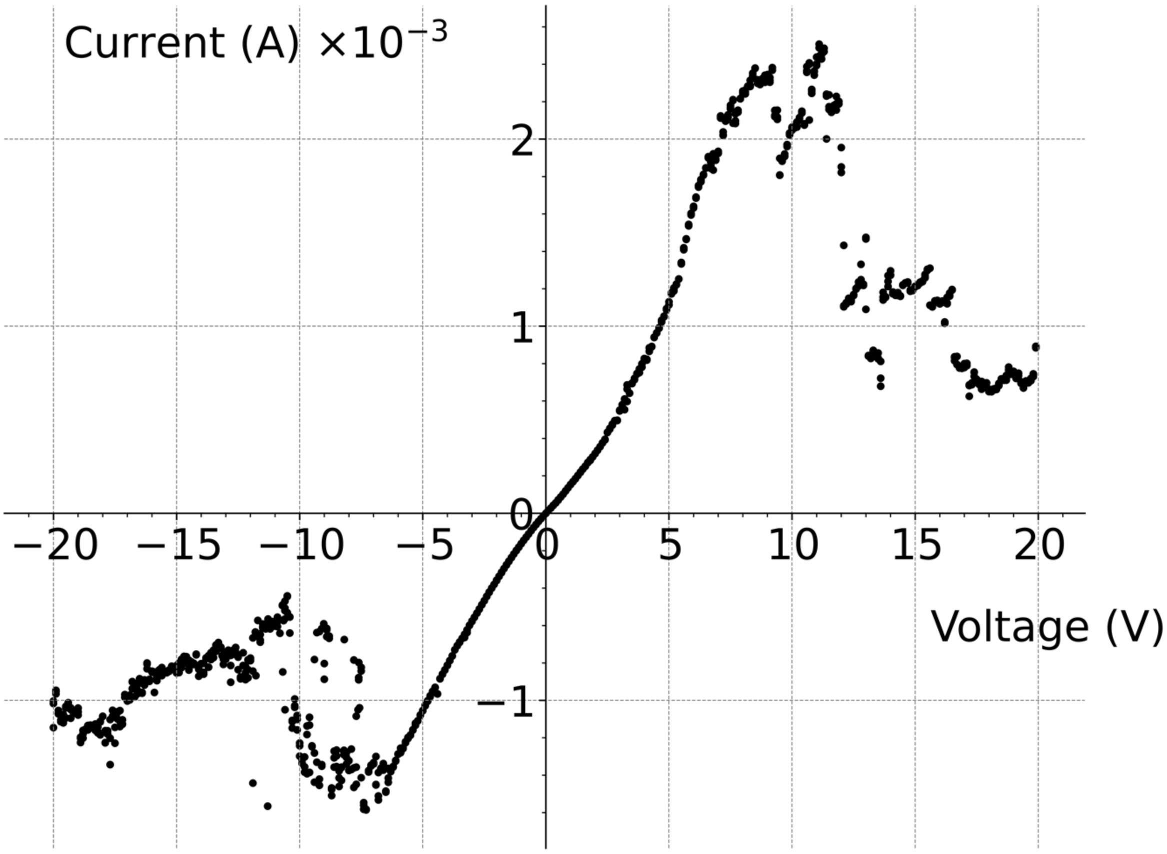

Figure 51 - Diode 5 I-V response, the noisy response is primarily due to the poor application of the wires and metal contacts

4.4.6 Surface contacts and Silver Contamination

Throughout this project, surface contacts were a limiting factor for all diodes. The manual process of applying silver DAG to form ohmic contacts between the metal contacts and the wires was difficult to replicate. This often led to weak ohmic contacts and irreproducible results. Moreover, the organic polymer within the silver DAG began to dry up and deform overtime, further reducing electronic performance. The reapplication of wires was time consuming and often required the metal layer to be completely removed. In some instances, it was possible to just reapply the silver DAG without the aqua regia cleaning step. However, cleaning of the surface with just acetone led to silver migration on the surface as shown in Figure 52. As a result, leakage currents and unpredictable IV characteristics occur when biases are applied.

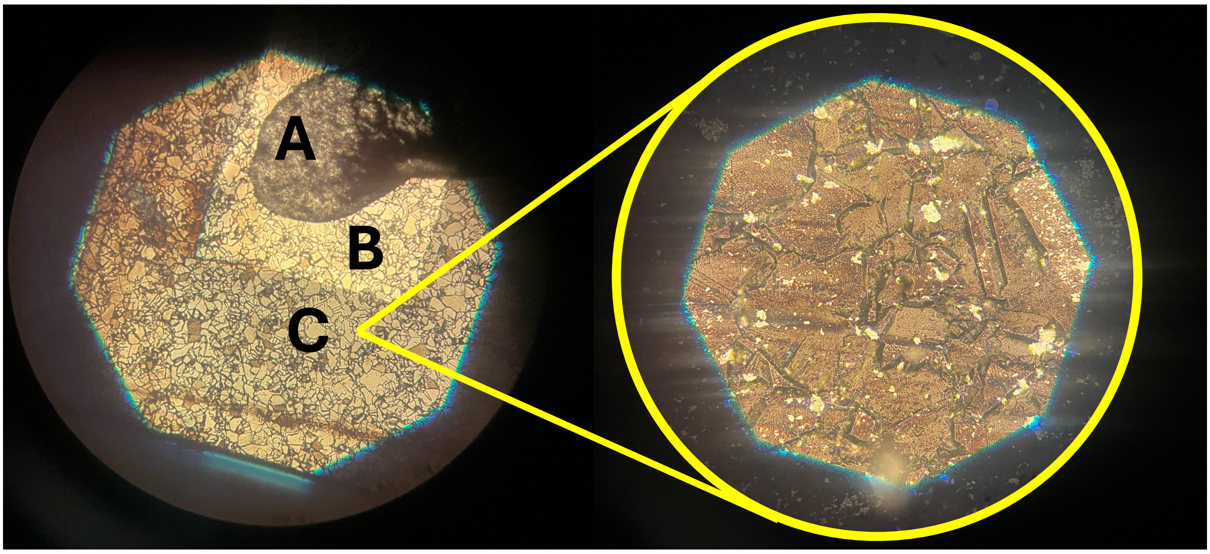

Figure 52 – An optical microscope image of [A] the wire and silver DAG [B] Pt/Pd metal contacts [C] Silver migration on the diamond surface, outside of the Pt/Pd contacts

During the fabrication of Diode 1, the primary target used in the AGAR high resolution sputter coater was silver (Ag), this target was routinely switched to Pt/Pd for the device sputtering. It was hypothesised that the background silver atoms within the sputter coater may have contaminated the Pt/Pd ohmic contacts creating a more homogenous contact with the silver DAG. This led to Diode 1 having superior electrical performance, with residual silver unintentionally enhancing the contact performance.

To investigate this issue, a control piece of silicon was masked in an identical way to samples before sputtering. Prior to sputtering with Pt/Pd, a two-minute sputter using a silver target to model silver contamination within the chamber was undertaken. This control was then subjected to EDS analysis to check for potential cross-contamination within the sputtering chamber. Figure 53 shows the results of EDS analysis, revealing a small yet significant Ag signal of ~0.1% atomic concentration. While the percentage is low, the presence of a visible Ag peak in the spectrum suggests that even trace levels of contamination could affect the composition and electronic behaviour of the ohmic contacts. To further investigate this, future work would involve the fabricating diodes using Ag contacts instead of or in conjunction with Pt/Pd, assessing if this improves device performance.

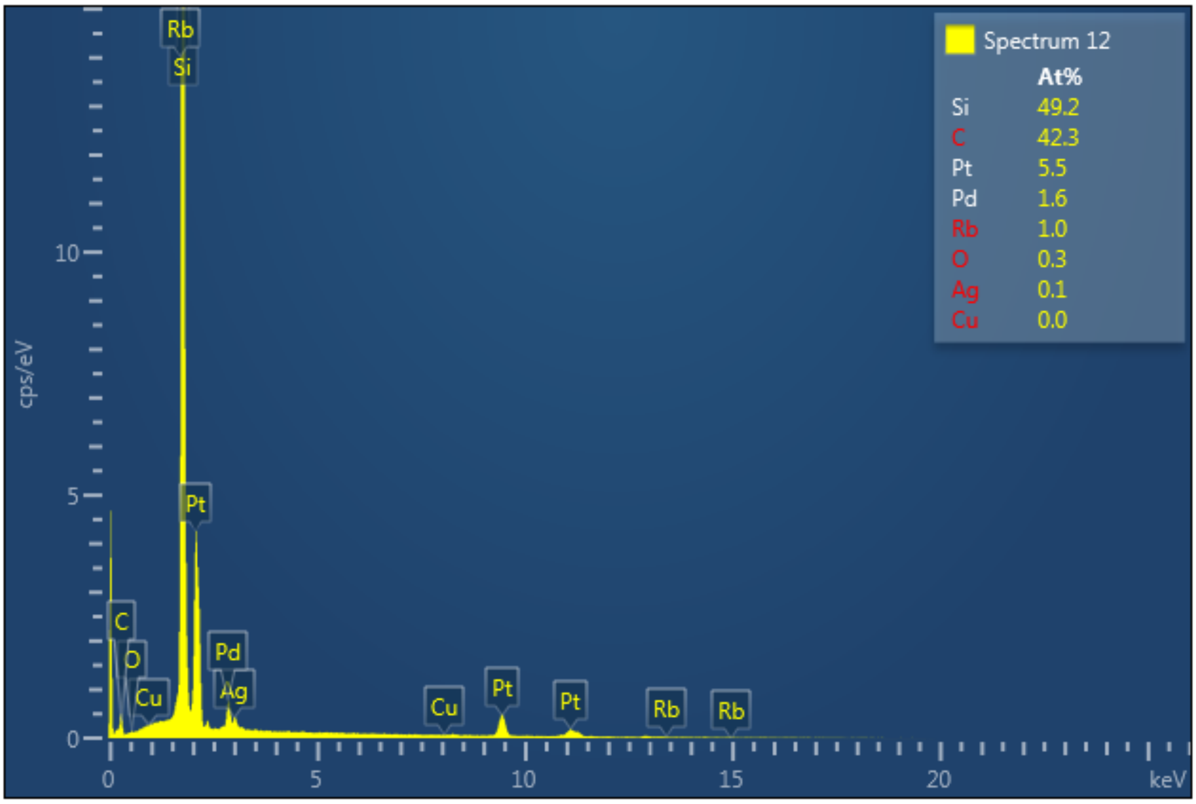

Figure 53 - EDS Spectrum from silver contamination investigation, measurements taken using the JSM-IT300 SEM kit from JEOL.

5 Conclusions and Future Work

5.1 Conclusions

In this project, microwave enhanced plasma CVD (MWCVD) was successfully utilised to grow and fabricate five devices from PCD substrates. The primary objective, the fabrication and evaluation of a working P-i-N junction diode was achieved through the fabrication of Device Structure I. This was then reproducibly grown and I-V characteristics evaluated. Two devices, Diode 1 and Diode 4, demonstrated functional diode behaviour, validating the fabrication methodology. The initial measurements of Diode 1 produced a rectification ratio of approximately 311, observed at 12 V. Upon remeasurement following reapplication of the metal contacts, a maximum forward current of 6×10^{-4} A at 20 V was achieved. The threshold voltage was estimated to be approximately 5.5 V, aligning well with the theoretical built-in potential of 5.4 V and suggesting minimal voltage drop outside the junction. This is evidence of efficient charge collection and near-ideal diode behaviour.

The secondary aim, investigating boron and nitrogen co-doping to achieve an n-type diamond layer at room temperature, was also investigated briefly. Although preliminary results were inconclusive due to insufficient nitrogen flow (1.1 sccm), the approach remains promising. Further investigation into reactor conditions and in situ optical emission spectroscopy are required to understand the plasma composition and growth environment.

The tertiary aim involved assessing the performance of industrially sourced BDD substrates, as used in Device Structure II. Raman spectroscopy and electrical measurements showed that the boron concentration was lower than reported by industry. These findings helped qualify the poor performance of Diode 3, underscoring a possible future challenge in the scaling-up of the manufacturing process.

Furthermore, the boron concentration of the p-type layers of in-house grown diamond was accurately determined using both Raman spectroscopy and four-point probe measurements. The growth of heavily boron-doped p-type diamond with resistivities comparable to literature was achieved reproducibly.

Overall, this work established a repeatable method for fabricating a diamond P-i-N junction diode using MWCVD. The devices demonstrated promising I-V characteristics and provided a foundation for further exploration of P-i-N junction diodes and their application in betavoltaics.

5.2 Future work

To extend this project an immediate priority is to test the best-performing devices, Diode 1 and Diode 4, as betavoltaic cells. Measurements would be conducted using a
Ni-63 beta source, with factors such as total conversion efficiency and total power output to be qualitatively assessed. In parallel, the recently constructed Kimball electron beam (E-beam) would be employed to simulate tritium beta decay.
Comparably to the work of Shimaoka et al., the diode would be characterised under electron beam irradiation [75]. The device would be exposed to electron energies ranging from 5 keV to 20 keV, allowing for a controlled investigation of charge collection in conditions analogous to tritium emission. If the tritium E-beam tests are successful, the electrical performance of the

device could also be studied, having been subject to high temperature gas loading via the recently commissioned tube furnace. Deuterium, another isotope of hydrogen, would likely be used instead of tritium to avoid the safety risks and regulatory challenges associated with handling radioactive materials. This substitution enables safe experimentation while still yielding valuable insights applicable to tritium systems.

Another key focus is the optimisation of the metal contacts. In this work, Pt/Pd was used to make ohmic contacts with the diamond surface but many other metals such as Ag, Au, Pt, Pd and Al can all be sputtered to create metal contacts. Yuan et al. investigates the contact properties of Pt, Pd and Au electrodes on the same hydrogen terminated diamond surface [112]. The paper concludes that the Pd/H-diamond made good ohmic contact before annealing and was the only contact that's sheet resistivity remained stable at high temperature. These findings are especially relevant if temperature dependent I–V measurements are revisited in future experiments. Initial attempts to conduct high-temperature measurements in this work were unsuccessful due to burning of silver DAG and therefore have been removed from this thesis.

In the same vein, while silver DAG was used in the initial prototypes, it exhibited poor adhesion which led to inconsistent I-V characteristic responses. The manual application process also made reproducibility challenging. Exploring new techniques, such as the creation of van der Waals metal-semiconductor junctions for reproducible I-V characterisation. In which, atomically flat metal surfaces are laminated onto semiconductor surfaces, without direct chemical bonding [113], creates an interesting avenue for future work.

In terms of structural characterisation, destructive analysis techniques may provide further insight into the device and understanding of the P-i-N junction. SEM could be used to confirm layer thickness by imaging the diode cross-section. Additionally, secondary ion mass spectroscopy (SIMS) to destructively measure the concentration of the dopants within the bulk of the material. This is particularly important for the n-type layer, whereby accurate measurement of nitrogen concentrations was not conducted during this project. Instead, it was predicted based on literature and similar experiment in the diamond laboratory that preceded this project.

At the University of Bristol, the NanoESCA facility is a state-of-the-art surface-sensitive system, that allows one to gain insight into the surface electronic properties of a material.

The best diodes could be analysed by photoemission electron microscopy (PEEM) mapping local variations in work function and electron emission across the surface. Alternatively, X-ray photoelectron spectroscopy (XPS) can be undertaken to better understand the elemental composition and electronic states of both the n-type and p-type layers.

Looking even further ahead, the long-term goal is to optimise the doping process to reliably achieve high-conductivity n-type diamond layers at room temperature. One possible avenue involves replacing molecular nitrogen with ammonia (NH_3) as the nitrogen source in MWCVD. The weaker N–H bond in ammonia, compared to the triple bond in N_2, may facilitate more efficient activation and incorporation of nitrogen into the diamond lattice, which may be particularly applicable to experimental co-doping. However, this would require a new dedicated ammonia gas line or potentially even require funding for a new MWCVD reactor.

Alternatively, phosphorus doping may offer a more direct path to n-type conductivity. Phosphorus introduces a shallower donor level (0.6 eV) compared to nitrogen (1.7 eV). A possible future experiment could involve replicating the work of Shimaoka et al., but with the addition of an intrinsic layer fabricating a P-i-N junction. This work would also include the use of single crystal diamond (SCD) substrates rather than PCD, providing more dopant control and an overall reduction in grain boundary effects on electrical properties. However, this would also require infrastructure changes, with the installation of a new dedicated gas lines into the MWCVD reactor and possibly even changes to the reactor design. Ohtani et al. demonstrated a more focussed gas flow, with through holes directly below the substrate, leading to an increase in the incorporation efficiency of phosphorus into diamond and a reduction deposition of phosphorus onto reactor walls [56]. This work could also be extended to other dopant species such as boron or nitrogen.

6 References

1. W Ehrenberg, Chi-Shi Lang, & R West. (1951). The Electron Voltaic Effect. *Proceedings of the Physical Society. Section A, 64*(4), 424.
2. Rappaport, P. (1954). The Electron-Voltaic Effect in p-n Junctions Induced by Beta-Particle Bombardment. *Physical Review, 93*(1), 246–247.
3. Bormashov, V. S., Troschiev, S. Yu., Tarelkin, S. A., Volkov, A. P., Teteruk, D. V., Golovanov, A. V., Kuznetsov, M. S., Kornilov, N. V., Terentiev, S. A., & Blank, V. D. (2018). High power density nuclear battery prototype based on diamond Schottky diodes. *Diamond and Related Materials, 84*, 41–47.
4. C. Zhou, J. Zhang, Wang, X., Yang, Y., Xu, P., Li, P., Zhang, L., Chen, Z., Feng, H., & Wu, W. (2021). Review—Betavoltaic Cell: The Past, Present, and Future. *ECS Journal of Solid State Science and Technology, 10*(2), 027005
5. Rappaport, P., & Loferski, J. J. (1954). *Radioactive battery employing semiconductors* (US Patent No. 2,976,433). U.S. Patent and Trademark Office. Retrieved November 11, 2024, from https://patents.google.com/patent/US2976433A/en
6. Alam, T. R., Tchouaso, M. T., & Prelas, M. A. (2023). *Summary of the design principles of betavoltaics and space applications* (pp. 293–345).
7. Olsen, L. C. (1993). *Review of betavoltaic energy conversion* (NASA Technical Memorandum No. NASA-TM-z106906). National Aeronautics and Space Administration.
8. Olsen, L. C. (1973). Betavoltaic energy conversion. *Energy Conversion, 13*(4), 117–127.
9. Huffman, F. N., & Norman, J. C. (1974). Nuclear-Fueled Cardiac Pacemakers. *Chest*, *65*(6), 667–672.
10. Romer, M., Miley, G. H., Luo, N., & Gimlin, R. J. (2008). Ragone Plot Comparison of Radioisotope Cells and the Direct Sodium Borohydride/Hydrogen Peroxide Fuel Cell With Chemical Batteries. *IEEE Transactions on Energy Conversion*, *23*(1), 171–178.
11. Matheson, W.E. (1975). The Betavoltaic Pacemaker Power Source. *Engineering in Medicine*, 401–424.
12. Bunney, L. R., & Scadden, E. M. (1967). Decay characteristics of 146Pm. *Journal of Inorganic and Nuclear Chemistry, 29*(10), 2497–2502.

13. Palmieri, V. G., Casalino, M., Di Gennaro, E., Romeo, E., & Russo, R. (2024). Alpha and beta-voltaic silicon devices operated at cryogenic temperatures: An energy source for deep space exploration. *Next Energy, 3,* 100101.
14. Olsen, L. C., Cabauy, P., Elkind, B. J., (2012). *Betavoltaic power sources*. *Physics Today,* *65*(12), 35–40.http://betabatt.com/files/Betavoltaic%20power%20sources%20PhysicsToday%20V65P35%20December%202012.pdf
15. Jeffrey, K., & Parsonnet, V. (1998). Cardiac Pacing, 1960–1985. *Circulation, 97*(19), 1978–1991.
16. Ghasemabadi, D., Zaki Dizaji, H., & Abdollahzadeh, M. (2024). Investigation and Analysis of Beta Radioisotopes for Optimal Use in Betavoltaic Batteries. *Nuclear Science and Engineering,* 1–14.
17. City Labs. (n.d.). *Nuclear batteries*. Retrieved March 31, 2025, from https://citylabs.net/nuclear-batteries/
18. Li, X., Lu, J., Chen, Z., Liu, X., Liu, Y., Zhang, Y., Zhang, Y., & Tian, F. (2023). 14C diamond as energy converting material in betavoltaic battery: A first principles study. *AIP Advances*, *13*(11).
19. Adams, T. E., & S.T. Revankar. (2015). *Research, development and evaluation capabilities for betavoltaic power sources.*
20. Bennett, G. L., Hemler, R. J., Schock, A. (1996), Space nuclear power: An overview. *Journal of Propulsion and Power*, 12(5), 901–910.
21. Palaporn, D., Tanusilp, S., Sun, Y., Pinitsoontorn, S. & Kurosaki, K. (2024). Thermoelectric materials for radioisotope thermoelectric generators. *Materials Advances, 5*(13), 5351–5364.
22. Yim, M.-S., & Caron, F. (2006). Life cycle and management of carbon-14 from nuclear power generation. *Progress in Nuclear Energy, 48*(1), 2–36.
23. S. Bocharov, Isakov, A. I., Yuri Yu. Petrov, Орехова, К. Н., Дементьева, Е. В., Burakov, B. E., & Zamoryanskaya, M. V. (2021). Study of radioluminescence and cathodoluminescence of artificial diamond single crystals as prospective durable core material for nuclear electric batteries. *Diamond and Related Materials, 120*, 108658–108658.
24. UK Atomic Energy Authority. (2024, December 4). *Diamonds are forever? World-first carbon-14 diamond battery made.* GOV.UK. Retrieved December 4, 2024, from

https://www.gov.uk/government/news/diamonds-are-forever-world-first-carbon-14-diamond-battery-made

25. Hu, C. (2010). *Modern semiconductor devices for integrated circuits*. Prentice Hall.
26. Mikhailov, E. E., & Yang, R. (n.d.). *Physics 252 Analog Electronics Lab Manual: Chapter 5 – Diodes*. Department of Physics, College of William & Mary.
27. S. M. Sze, Yiming Li, and Kwok K. Ng. Physics of semiconductor devices. John Wiley & Sons, Inc., Hoboken, NJ, fourth edition. edition, 2021.
28. May, P. (1996). *Diamond – Molecule of the Month*. University of Bristol. Retrieved December 11, 2024, from https://www.bristol.ac.uk/Depts/Chemistry/MOTM/diamond/diamond.htm
29. Grand View Research. (n.d.). *Diamond market size, share & trends analysis report.* Retrieved November 9, 2024, from https://www.grandviewresearch.com/industry-analysis/diamond-market
30. Slaymaker, R. (2024). *Diamond mining giant De Beers experiences 21% revenue decline in H1 2024*. Mining Technology. Retrieved November 7, 2024, from https://www.mining-technology.com/news/diamond-mining-giant-de-beers-experience-21-revenue-decline-in-h1-of-2024/#?cf-view
31. Y.A. Sorb, Bundy, F. P., & DeVries, R. C. (2016). Diamond: High-Pressure Synthesis. *Elsevier EBooks*.
32. Eaton-Magaña, S., Shigley, J. E., & Breeding, C. M. (2017). Observations on HPHT-grown synthetic diamonds: A Review. *Gems & Gemology, 53*(3), 262-284.
33. May, P. W. (2000). Diamond thin films: a 21st-century material. *Philosophical Transactions of the Royal Society of London. Series A: Mathematical, Physical and Engineering Sciences, 358*(1766), 473-495.
34. Nemanich, R. J., Carlisle, J. A., Hirata, A., & Haenen, K. (2014). CVD diamond—Research, applications, and challenges. *MRS Bulletin, 39*(6), 490–494.
35. Veljkovic, S., Mitic, V., Paunovic, V., Lazovic, G., Mohr, M., & Fecht, H. (2020). Analyses of the surface parameters in polycrystalline diamonds. *Serbian Journal of Electrical Engineering, 17(*1), 111–129.
36. Kaminski, N. (2009). State of the art and the future of wide band-gap devices. *Power Electronics and Applications, 2009. EPE '09. 13th European Conference On*, 1–9.
37. Isberg, J., Hammersberg, J., Johansson, E., WikströmT., Twitchen, D. J., Whitehead, A. J., Coe, S. E., & Scarsbrook, G. A. (2002). High Carrier Mobility in Single-Crystal Plasma-Deposited Diamond*.* *Science, 297*(5587), 1670–1672.

38. Wort, C. J. H., & Balmer, R. S. (2008). Diamond as an electronic material. *Materials Today, 11*(1-2), 22–28.
39. Gherardini, L., Michaud, P., M. Panizza, C. Comninellis, & N. Vatistas. (2001). Electrochemical Oxidation of 4-Chlorophenol for Wastewater Treatment: Definition of Normalized Current Efficiency. *Journal of the Electrochemical Society*, *148*(6).
40. Fujishima, A., Einaga, Y., Rao, T. N., & Tryk, D. A. (Eds.). (2005). *Diamond electrochemistry.* Elsevier.
41. Kalish, R. (1999). Doping of diamond. *Carbon, 37*(5), 781–785.
42. Williams, O. A., Whitfield, M. D., Jackman, R. B., Foord, J. S., Butler, J. E., & Nebel, C. E. (2001). Formation of shallow acceptor states in the surface region of thin film diamond. *Applied Physics Letters, 78*(22), 3460–3462.
43. Zhang, G., Zulkharnay, R., Ke, X., Liao, M., Liu, L., Guo, Y., Li, Y., Rubahn, H-G., Moshchalkov, V. V., & May, P. W. (2023). Unconventional Giant "Magnetoresistance" in Bosonic Semiconducting Diamond Nanorings. *Advanced Materials,* 35(22).
44. Goss, J. P., Eyre, R. J., & Briddon, P. R. (2008). Theoretical models for doping diamond for semiconductor applications. *Physica Status Solidi (B), 245*(9), 1679–1700.
45. Jiang, N., Hatta, A., & Ito, T. (1998). Nitrogen Doping Effects on Electrical Properties of Diamond Films. *Japanese Journal of Applied Physics, 37*(10A), L1175–L1175.
46. Pinault, M.-A. ., Barjon, J., Kociniewski, T., Jomard, F., & Chevallier, J. (2007). The n-type doping of diamond: Present status and pending questions. *Physica B: Condensed Matter, 401-402*, 51–56.
47. Chayahara, A., Mokuno, Y., Horino, Y., Takasu, Y., Kato, H., Yoshikawa, H., & Fujimori, N. (2004). The effect of nitrogen addition during high-rate homoepitaxial growth of diamond by microwave plasma CVD. *Diamond and Related Materials, 13*(11-12), 1954–1958.
48. Yan, C., Vohra, Y. K., Mao, H., & Hemley, R. J. (2002). Very high growth rate chemical vapor deposition of single-crystal diamond. *Proceedings of the National Academy of Sciences of the United States of America, 99*(20), 12523–12525.
49. Jin, S., & Moustakas, T. D. (1994). Effect of nitrogen on the growth of diamond films. *Applied Physics Letters, 65*(4), 403–405.
50. Dai, Y., David Yun Dai, Liu, D., Han, S., & Huang, B. (2004). Mechanism of p-type-to-n-type conductivity conversion in boron-doped diamond. *Applied Physics Letters, 84*(11), 1895–1897.

51. Prawer, S., Uzan-Saguy, C., Braunstein, G., & Kalish, R. (1993). Cann-type doping of diamond be achieved by Li or Na ion implantation? *Applied Physics Letters, 63*(18), 2502–2504.
52. Koizumi, S., Kamo, M., Sato, Y., Mita, S., Sawabe, A., Reznik, A., Uzan-Saguy, C., & Kalish, R. (1998). Growth and characterization of phosphorus doped n-type diamond thin films. *Diamond and Related Materials, 7*(2-5), 540–544.
53. Katamune, Y., Izumi, A., Ichikawa, K., & Koizumi, S. (2023). Heavy phosphorus doping of diamond by hot-filament chemical vapor deposition. *Diamond and Related Materials, 134*, 109789–109789.
54. Zhao, S. (2016). *Theoretical Studies of Diamond for Electronic Applications* (PhD Thesis, Acta Universitatis Upsaliensis).
55. Koizumi, S. (1999). Growth and Characterization of Phosphorus Doped n-Type Diamond Thin Films. *Physica Status Solidi, 172*(1), 71–78.
56. Ohtani, R., Yamamoto, T., Janssens, S. D., Yamasaki, S., & Koizumi, S. (2014). Large improvement of phosphorus incorporation efficiency in n-type chemical vapor deposition of diamond. *Applied Physics Letters, 105*(23).
57. Goss, J., (n.d.) *n-type doping of diamond*. (Newcastle University.). Retrieved November 10, 2024, from https://www.staff.ncl.ac.uk/j.p.goss/Research/NtypeDiamond/
58. Croot, A., Othman, M. Z., Conejeros, S., Fox, N. A., & Allan, N. L. (2018). A theoretical study of substitutional boron–nitrogen clusters in diamond. *Journal of Physics Condensed Matter*, *30*(42), 425501–425501.
59. Katayama-Yoshida, H., Nishimatsu, T., Yamamoto, T., & Orita, N. (2001). Codoping method for the fabrication of low-resistivity wide band-gap semiconductors in p-type GaN, p-type AlN, and n-type diamond: Prediction versus experiment. *Journal of Physics: Condensed Matter, 13*(40), 8901–8914.
60. Segev, D., & Wei, S.-H. (2003). Design of Shallow Donor Levels in Diamond by Isovalent-Donor Coupling. *Physical Review Letters, 91*(12).
61. Delun, Z., Tang, L., Geng, Y., Zhang, J., Yue, R., & Wang, Y. (2020). First-principles calculation to N-type Li N Co-doping and Li doping in diamond. *Diamond and Related Materials, 110*, 108070.
62. Conejeros, S., Othman, M. Z., Croot, A., Hart, J. N., O'Donnell, K. M., May, P. W., & Allan, N. L. (2020). Hunting the elusive shallow n-type donor – An ab initio study of Li and N co-doped diamond. *Carbon, 171*, 857–868.

63. Wu, Y., Tong, J., Ruan, L., Luo, F., Liu, G., Zhang, R., Han, X., Zhang, Y., Tian, F., & Zhang, X. (2021). N-type diamond semiconductor induced by co-doping selenium and boron. *Computational Materials Science, 196*, 110515–110515.
64. Dai, Y., David Yun Dai, Liu, D., Han, S., & Huang, B. (2004). Mechanism of p-type-to-n-type conductivity conversion in boron-doped diamond. *Applied Physics Letters, 84*(11), 1895–1897.
65. Shur, M. (2019). Wide band gap semiconductor technology: State-of-the-art. *Solid-State Electronics, 155*, 65–75
66. Shenai, K., Scott, R. S., & Baliga, B. J. (1989). Optimum semiconductors for high-power electronics. *IEEE Transactions on Electron Devices, 36*(9), 1811–1823.
67. Graebner, J.E. (1995). Thermal Conductivity of Diamond. *Diamond: Electronic Properties and Applications*, 285–318.
68. Tiwari, A. K., Goss, J. P., Briddon, P. R., Wright, N. G., Horsfall, A. B., & Rayson, M. J. (2012). Effect of different surface coverages of transition metals on the electronic and structural properties of diamond. *Physica Status Solidi (A), 209*(9), 1697–1702.
69. Koizumi, S. (1999). Growth and Characterization of Phosphorus Doped n-Type Diamond Thin Films. *Physica Status Solidi, 172*(1), 71–78.
70. Behnke, T., Doucet, M., Ghodbane, N., Imhof, A., Martínez C., & Zeuner, W. (2002). Electromagnetic radiation hardness of diamond detectors. *Nuclear Instruments and Methods in Physics Research Section A: Accelerators, Spectrometers, Detectors and Associated Equipment, 489*(1-3), 230–240.
71. Shimaoka, T., Koizumi, S., & Kaneko, J. H. (2021). Recent progress in diamond radiation detectors. *Functional Diamond, 1*(1), 205–220
72. Adam, W., & others (1997). Development of CVD diamond radiation detectors. *Electrochemical Society Proceedings*, 97-32, 491–502.
73. Tang, L., Tsai, C., Gerberich, W. W., Kruckeberg, L., & Kania, D. R. (1995). Biocompatibility of chemical-vapour-deposited diamond. *Biomaterials, 16*(6), 483–488.
74. Delfaure, C., Pomorski, M., J. de Sanoit, P. Bergonzo, & Saada, S. (2016). Single crystal CVD diamond membranes for betavoltaic cells. *Applied Physics Letters, 108*(25).
75. Shimaoka, T., Umezawa, H., Ichikawa, K., Pernot, J., & Koizumi, S. (2020). Ultrahigh conversion efficiency of betavoltaic cell using diamond pn junction. *Applied Physics Letters, 117*(10), 103902.

76. Shockley, W., & Queisser, H. J. (1961). Detailed Balance Limit of Efficiency of p-n Junction Solar Cells. *Journal of Applied Physics, 32*(3), 510–519.
77. Okada, S., & Momoshima, N. (1993). Overview of Tritium. *Health Physics*, *65*(6), 595–609.
78. Roth, E., Abassin, J. J., Botter, F., Briec, M., Chenebault, P., Masson, M., Rasneur, B., & Roux, N. (2003). Irradiation of lithium aluminate and tritium extraction. *Journal of Nuclear Materials*, 133-134, 238–241.
79. Ferreira, M, F., Turner, A., Vernon, E. L., Grisolia, C., L. Lebaron-Jacobs, Malard, V., & Jha, A. N. (2023). Tritium: Its relevance, sources and impacts on non-human biota. *Science of the Total Environment, 876*, 162816–162816.
80. Poletiko, C. (1988). Determination of nickel-63. *Environment International, 14*(5), 387–390.
81. *National Nuclear Data Center, Brookhaven National Laboratory*, (2008), Retrieved March 25, 2025, from (https://www.nndc.bnl.gov/nudat3/).
82. Zulkharnay, R., (2023). *Electron Emission Studies of Scandium on Diamond for Thermionic Solar Energy Generation Devices* (PhD thesis, University of Bristol).
83. Croot, A., (2018). *Boron and nitrogen in diamond: an ab initio simulation, plasma emission spectroscopy and material deposition & characterisation study* (PhD thesis, University of Bristol).
84. Nutbrown, B., (2024). *Microwave plasma assisted growth of CVD diamond incorporating BN atom clusters* (MSci thesis, University of Bristol).
85. Thoms, B. D., Owens, M. S., Butler, J. E., & Spiro, C. (1994). Production and characterization of smooth, hydrogen-terminated diamond C(100). *Applied Physics Letters*, *65*(23), 2957–2959.
86. Manfredotti, C., Fizzotti, F., Lo Giudice, A., Manfredotti, Ch., Castellino, M., Bonino, P., & Vittone, E. (2008). A comprehensive study on hydrogenated diamond surfaces as obtained by using molecular hydrogen. *Diamond and Related Materials, 17*(7-10), 1154–1158.
87. Van der Weide, J., & Nemanich, R. J. (1993). Argon and hydrogen plasma interactions on diamond (111) surfaces: Electronic states and structure. *Applied Physics Letters, 62*(16), 1878–1880.
88. Anthony, T. R. (2003). Metastable synthesis of diamond. *Vacuum, 41*(4-6), 1356–1359.

89. Thoms, B. D., Pehrsson, P. E., & Butler, J. E. (1994). A vibrational study of the adsorption and desorption of hydrogen on polycrystalline diamond. *Journal of Applied Physics, 75*(3), 1804–1810.
90. Keithley Instruments. (n.d.). Model 2401 SourceMeter® datasheet. Retrieved March 31, 2025, from https://www.testequipmenthq.com/datasheets/KEITHLEY-2401-Datasheet.pdf
91. Walock, M. J. (2012). *Nanocomposite coatings based on quaternary metal-nitrogen and nanocarbon systems* (Doctoral thesis, Université Paris-Est)
92. Miccoli, I., Edler, F., Pfnür, H. and Tegenkamp, C., 2015. The 100th anniversary of the four-point probe technique: the role of probe geometries in isotropic and anisotropic systems. *Journal of Physics: Condensed Matter, 27*(22), p.223201.
93. Sze, S. M., Li, Y., & Ng, K. K. (2021). *Physics of semiconductor devices* (4th ed.). John Wiley & Sons, Inc.
94. University of Warwick. (n.d.). *Hall effect measurements*. Department of Physics. Retrieved April 2, 2025, from https://warwick.ac.uk/fac/sci/physics/current/postgraduate/regs/mpagswarwick/ex5/techniques/electronic/hall-effect/.
95. Filik, J. (2005). *Raman spectroscopy: a simple, non-destructive way to characterise diamond and diamond-like materials. 17*(5).
96. Kuntumalla, M. K., Elfimchev, S., Chandran, M., & Hoffman, A. (2018). Raman scattering of nitrogen incorporated diamond thin films grown by hot filament chemical vapor deposition. *Thin Solid Films, 653*, 284–292.
97. López-Ríos, T., Sandré, É., Leclercq, S., & Sauvain, É. (1996). Polyacetylene in Diamond Films Evidenced by Surface Enhanced Raman Scattering. *Physical Review Letters, 76*(26), 4935–4938.
98. Ferrari, A. C., & Robertson, J. (2000). Interpretation of Raman spectra of disordered and amorphous carbon. *Physical Review B, 61*(20), 14095–14107.
99. Prawer, S., & Nemanich, R. J. (2004). Raman spectroscopy of diamond and doped diamond. *Philosophical Transactions of the Royal Society of London. Series A: Mathematical, Physical and Engineering Sciences, 362*(1824), 2537–2565.
100. May, P. W., Ludlow, W. J., Hannaway, M., Heard, P. J., Smith, J. A., & Rosser, K. N. (2007). Raman and conductivity studies of boron-doped microcrystalline diamond, facetted nanocrystalline diamond and cauliflower diamond films. *Diamond and Related Materials, 17*(2), 105–117.

101. Knittel, P., Stach, R., Yoshikawa, T., Kirste, L., Mizaikoff, B., Kranz, C., & Nebel, C. E. (2018). Characterisation of thin boron-doped diamond films using Raman spectroscopy and chemometrics. *Analytical Methods, 11(*5), 582–586.

102. Bernard, M., Baron, C., & Deneuville, A. (2004). About the origin of the low wave number structures of the Raman spectra of heavily boron doped diamond films. *Diamond and Related Materials, 13*(4-8), 896–899.

103. V. Mortet, I. Gregora, Taylor, A., Lambert, N., P. Ashcheulov, Z. Gedeonova, & P. Hubik. (2020). New perspectives for heavily boron-doped diamond Raman spectrum analysis. *Carbon, 168*, 319–327.

104. Bernard, M., Deneuville, A. & Muret, P. (2004) a Non-destructive determination of the boron concentration of heavily doped metallic diamond thin films from Raman spectroscopy. *Diamond and Related Materials, 13*, 282.

105. Smits, F.M. (1958) Measurement of sheet resistivities with the four-point probe. *Bell System Technical Journal, 37*(3), pp.711-718.

106. *NSM Archive - Diamond (C) - Band structure and carrier concentration*. (n.d.). Retrieved April 1, 2025, from https://www.ioffe.ru/SVA/NSM/Semicond/Diamond/bandstr.html

107. *EP Poly 10.0x10.0mm, 0.60mm thick, NP*. (2025). Retrieved April 1, 2025, from https://e6cvd.com/uk/application/electrochemistry/pe-10x10-mm-0-6-mm-thick.html

108. Denisenko, A., & Kohn, E. (2005). Diamond power devices. Concepts and limits. *Diamond and Related Materials, 14*(3-7), 491–498.

109. Yuan, X., Zheng, Y., Zhu, X., Liu, J., Liu, J., Li, C., Jin, P., & Wang, Z. (2019). Recent progress in diamond-based MOSFETs. *International Journal of Minerals, Metallurgy, and Materials, 26*(10), 1195–1205.

110. Hemawan, K. W., & Hemley, R. J. (2015). Optical emission diagnostics of plasmas in chemical vapor deposition of single-crystal diamond. *Journal of Vacuum Science & Technology A: Vacuum, Surfaces, and Films, 33*(6).

111. McCauley, T. S., Israel, A., Vohra, Y. K., & Tarvin, J. T. (1997). Spatially resolved in situ diagnostics for plasma-enhanced chemical vapor deposition film growth. *Review of Scientific Instruments, 68*(4), 1860–1865.

112. Yuan, X., Liu, J., Shao, S., Liu, J., Wei, J., Da, B., Li, C., & Koide, Y. (2020). Thermal stability investigation for Ohmic contact properties of Pt, Au, and Pd electrodes on the same hydrogen-terminated diamond. *AIP Advances, 10*(5).

113. Liu, Y., Guo, J., Zhu, E., Liao, L., Lee, S.-J., Ding, M., Shakir, I., Gambin, V., Huang, Y., & Duan, X. (2018). Approaching the Schottky–Mott limit in van der Waals metal–semiconductor junctions. *Nature*, *557*(7707), 696–700.